Analysis of the Presence of Small Admixtures of Heavy Elements in the Solar Plasma by Using the SAHA-S Equation of State

S. V. Ayukov[1,]*, V. A. Baturin[1], V. K. Gryaznov[2], I. L. Iosilevskiĭ[3], A. N. Starostin[4], and V. E. Fortov[2]

[1] *Sternberg Astronomical Institute, Universitetskiĭ pr. 13, Moscow, 119992 Russia*
[2] *Institute of Problems of Chemical Physics, Russian Academy of Sciences, Chernogolovka, Moscow region, 142432 Russia*
[3] *Moscow Institute of Physics and Technology (State University),*
Institutskiĭ per. 9, Dolgoprudnyĭ, Moscow region, 141700 Russia
[4] *Troitsk Institute for Innovation and Thermonuclear Research, Troitsk, Moscow region, 142190 Russia*
* e-mail: asv@sai.msu.ru
Received May 26, 2004

The thermodynamic functions of a weakly nonideal plasma are extensively calculated for conditions typical of the depths of stars by using the SAHA-S equation of state. These calculations ensure precise analysis of the effect of the heavy-element content on adiabatic compressibility in the depths of the Sun. Comparison of model calculations with recent helioseismic data ensures more precise determination of solar-plasma composition. This comparison shows that the inclusion of additional components to the composition of heavy-element admixtures is a necessary condition for the theoretical equation of state and the results of analysis of solar oscillations to be consistent. © *2004 MAIK "Nauka/Interperiodica".*

PACS numbers: 95.30.Qd; 96.60.Fs

Extensive recent observation data on the eigenfrequencies of solar oscillations (see, e.g., [1]) provide information about physical conditions in the depths of the Sun and enable one to refine the model of the internal structure. In order to develop a model of the Sun, it is necessary to know the equation of state of the solar plasma with high accuracy. In turn, the comparison of theoretical models with helioseismic data opens a unique possibility of verifying and refining the equation of state of a weakly nonideal plasma with a high accuracy (higher than 10^{-4}). The comparison of theoretical data on the speed of sound and data reconstructed from helioseismic observations depends on the distribution of temperature, density, and chemical composition over the radius inside the Sun. Therefore, this problem is a multiparameter problem and requires the fixation of at least some of these data. In this work, we use data on the distribution of temperature and density from the model of the current Sun accepted in helioseismology [2], whereas the problem of the effect of the equation of state on the evolution and structure of the model is ignored.

Certain curves characterizing the used model data are shown in Fig. 1. Monotonically increasing solid line *1* is the density–temperature thermodynamic curve for the internal structure of the Sun. Equations of state are compared in this line. Part *3* marked by a heavy solid line corresponds to the zone of convective heat transfer, and most part of this zone is very close to the isentrope $S(T, \rho) = \text{const}$. Line *2* is the distribution of adiabatic

compressibility $\tilde{\gamma}_1 = (\partial \ln P / \partial \ln \rho)_S$. Regions of a considerable deviation of this quantity from an ideal-gas value of 5/3 correspond to the ionization of hydrogen and helium. The upper abscissa axis shows the relative radius for the corresponding temperature.
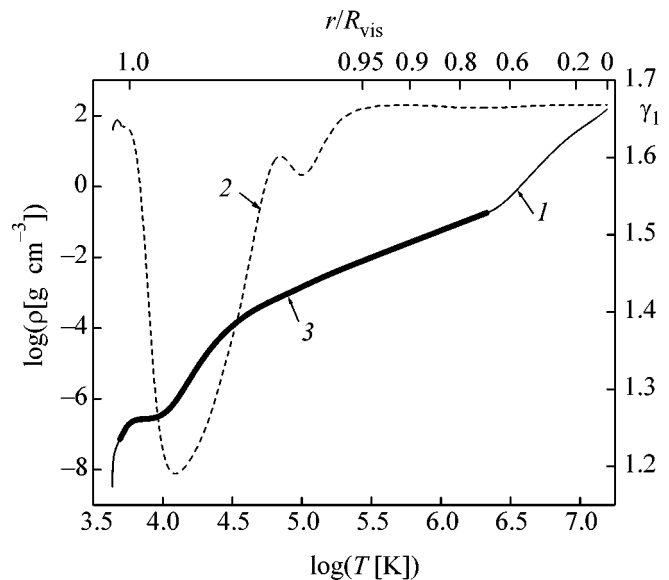

Fig. 1. Distribution of (*1*) density and (*2*) adiabatic compressibility inside the Sun according to the *S* model. Convective transfer zone (*3*) is indicated.

The equation of state and thermodynamic functions are calculated by using the "chemical" model [3]. The plasma consists of hydrogen, helium (these basic components amount to 98 wt %), and heavy admixtures of carbon, nitrogen, oxygen, and neon. The inclusion of silicon and iron is additionally studied upon the conservation of the 2% general mass fraction of admixtures. The plasma consists of more than 90 components: atoms, diatomic molecules, electrons, and ions from single-charged ions to ions with the maximum possible charge for each element.

According to [3], the free energy F of the system was represented as a sum, where the first term F_{id}^0 describes a mixture of noninteracting "ideal" particles—partially degenerate slightly relativistic electrons; classical ions; atoms and molecules; and photons (the radiation-pressure effect is quite noticeable particularly for $\tilde{\gamma}_1$). The second term ΔF_{int} describes interaction between these particles. Although the first term describes the translational degrees of freedom of particles and is decomposed into the terms for kinds of particles, chemical reactions between particles, as well as the ionization and recombination reactions, can proceed. Therefore, the resulting thermodynamic parameters differ from the ideal-gas values even in simple cases (see Fig. 1). Moreover, compound particles can have internal degrees of freedom, which are described in the below expression by the partition functions Q_j for particles of the jth kind:

$$F(\{N_i\}, V, T) = F_{\text{id}}^0 + \Delta F_{\text{int}}$$

$$= \sum_j N_j k_{\text{B}} T \left(\ln\left(\frac{n_i \chi_j^3}{Q_j}\right) - 1 \right) + \Delta F_{\text{int}}(\{N_i\}, V, T). \quad (1)$$

Here, N_j and n_j are the number of particles of the jth kind and their density, respectively; V is volume; T is the temperature of the system; k_{B} is the Boltzmann constant; and χ_j is the de Broglie thermal wavelength.

Corrections in the second term ΔF_{int} are usually associated with the nonideality of the system, although they are not the main cause of deviation from the equation of state for an ideal gas under solar conditions. The main part of the correction is attributed to the Coulomb interaction in the plasma and corresponds to the Debye approximation in the grand canonical ensemble [4] with allowance for the electron degeneracy. In addition, we include corrections for the electron diffraction upon scattering. The Coulomb and diffraction corrections have a smallness of $\sim\Gamma_{\text{D}}$ and $\sim\Gamma_{\text{D}}\chi_e\kappa_{\text{D}}$, respectively, where κ_{D} is the inverse Debye radius, $\Gamma_{\text{D}} = e^2\beta\kappa_{\text{D}}$ is the Debye nonideality parameter, and $\beta \equiv (k_{\text{B}}T)^{-1}$. The SAHA-S equation of state additionally includes the exchange correction $\sim\chi^2 e^2\beta$. We point out the relativistic correction $\sim k_{\text{B}}T/m_e c^2$ that is small for cold solar-type stars, but noticeably affects adiabatic compressibility.

The OPAL equation of state [4] is currently accepted as the reference equation of state in helioseismology. It was partially obtained from the first principles in the framework of the expansion of the Helmholtz thermodynamic potential Ω in series in activities. The OPAL equation of state includes nonrelativistic degenerate electrons, classical ions, all stages of ionization and excitation, molecular hydrogen, Coulomb approximation with allowance for the electron degeneracy, electron diffraction, electron exchange, and pressure-induced ionization (contributions from ladder diagrams are also mentioned). The second virial coefficient including contributions from ring and ladder diagrams is thought to be well known since Vedenov and Larkin [5, 6] and was refined by Ebeling *et al.* [7, 8] and Kopyshev [9]. Since the basic contribution from scattering states is proportional to $\sim\Gamma_{\text{D}}^2\ln\Gamma_{\text{D}}]$ and $\Gamma_{\text{D}} \sim 0.05$ in most of the internal part of the solar convective zone, these contributions in our equation of state of the solar plasma are ignored. It is considered a well-established fact [5, 7, 8] that the partition function Q_j over discrete levels is regularized by the Planck–Larkin procedure, and contribution to Ω for, e.g., nonrelativistic hydrogen atoms has the form [3]

$$\Delta\Omega_{\text{bs}} = -k_{\text{B}} T \zeta_e \zeta_i \chi_{ei}^3$$

$$\times \sum_{n=1}^{\infty} n^2 e^{\beta E_n}(1 - e^{-\beta E_n} - \beta E_n e^{-\beta E_n}), \quad (2)$$

where

$$E_n = \frac{Ry}{n^2}, \quad \chi_{ei} = \sqrt{\frac{2\pi\hbar}{\mu k_{\text{B}} T}}, \quad \mu = \frac{m_e m_p}{m_e + m_p}. \quad (3)$$

Expression (2) is used in the OPAL equation of state. At the same time, the following, more rigorous expression for the contribution from bound states, which differs from the Planck–Larkin expression, was presented in [10] without the deduction that was given in [11]:

$$\Delta\Omega_{\text{bs}} = -k_{\text{B}} T \zeta_e \zeta_i \chi_{ei}^3 \sum_{n=1}^{\infty} n^2 F_n(\beta) e^{\beta E_n}, \quad (4)$$

where

$$F_n(\beta) = 1 - e^{-\beta E_n}\left[4 - \frac{6}{\sqrt{\pi}}(\beta E_n)^{1/2} + \frac{4}{\sqrt{\pi}}(\beta E_n)^{3/2} \right]$$

$$+ \frac{\Gamma\left(\frac{1}{2}, \beta E_n\right)}{\sqrt{\pi}}[3 - 4\beta E_n + 4(\beta E_n)^2]. \quad (5)$$

Asymptotically for $\beta E_n \ll 1$, Eqs. (4) and (5) yield

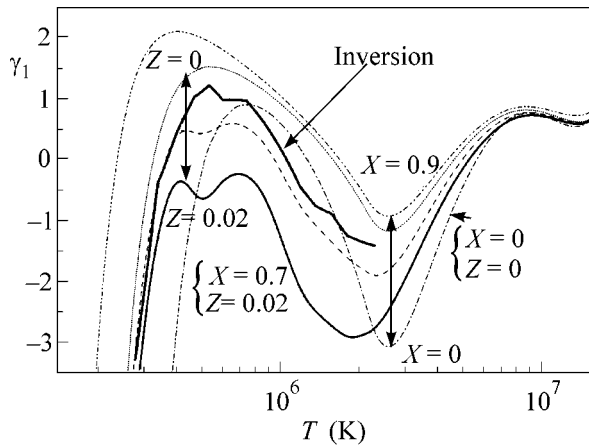$$n^2 F_n(\beta) \longrightarrow 2n^2(\beta E_n)^2, \quad (6)$$

Fig. 2. Effective adiabatic index $\gamma_1 = \left[\left(\dfrac{d\ln P}{d\ln\rho}\right)_s - \dfrac{5}{3}\right] \times 10^3$ inside the Sun for various fractions of hydrogen X and heavy elements Z in comparison with the inversion-procedure results [1].
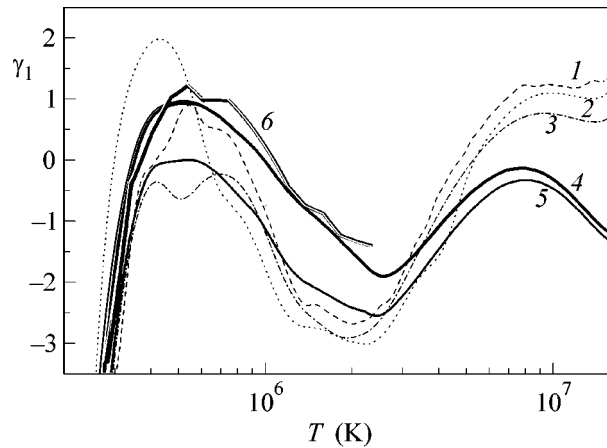
Fig. 3. Effective adiabatic index γ_1 for the equations of solar-plasma state (*1*) OPAL [4], (*2*) MHD [13], (*3*) SAHA-S (C–Ne), (*4*) SAHA-S, $Z = 0.01$ (C–Ne, Si, Fe), and (*5*) SAHA-S, $Z = 0.02$ (C–Ne, Si, Fe) in comparison with (*6*) the inversion-procedure results [1].

whereas the asymptotic behavior of Eq. (2) has the form

$$n^2 F_n^{\text{PL}}(\beta) \longrightarrow \frac{1}{2}n^2(\beta E_n)^2. \tag{7}$$

In contrast to the OPAL equation of state [4], the SAHA-S equation of state describes the solar-plasma model [12] by using Eqs. (4) and (5). However, it is difficult to directly compare the SAHA-S and OPAL equations of state by using only the initial assumptions. We can only state that these equations are quite consistent with each other with respect to the nonideality contribution, and the difference between them lies within the uncertainty in the description of these terms, which are small for the Sun and more massive stars. The basic difference from the OPAL equation of state is the addition of silicon and iron to the mixture of heavy elements.

Using the SAHA-S code intended for calculating the thermodynamics of the nonideal plasma of astrophysical objects, we calculated the composition and thermodynamic functions of the solar plasma for densities up to 200 g/cm^3 and temperatures up to 2×10^7 K. Using the calculated thermodynamic functions and procedure of calculating the solar parameters, we developed a model of the internal solar structure and its chemical evolution.

We compared the theoretical predictions of the equations of state and data of analysis of the spectrum of natural oscillations for a relatively narrow region in the depth of the Sun that covers the lower part of the convective zone. In this zone, the basic components of the solar plasma—hydrogen and helium—are already ionized, and the thermodynamic parameters are close to ideal-gas values. In particular, we focus on adiabatic compressibility, which deviates from 5/3 by no more than several thousandths in the region under consider-

ation. Moreover, the results of helioseismic inversion of adiabatic compressibility are most reliable in this region. We emphasize that the above values of the corrections responsible for various nonideality effects enable one to compare variations in pressure or internal energy. The situation is much more difficult for the effect of these factors on adiabatic compressibility. In this case, certain effects can be weakly manifested (e.g., electron degeneracy), whereas other effects can be surprisingly large (e.g., the contribution from radiation and the slight relativism of electrons).

Figures 2 and 3 show the results of calculations in comparison with the results of helioseismic inversion. We emphasize that the adiabatic index for temperatures higher than 2×10^6 K is reconstructed with much larger uncertainties, because this temperature is the bound of the convective-transfer zone with well-determined adiabatic stratification. For this reason, we focused on the interior of the convective zone.

These figures also show the results of calculations by the SAHA-S code. Figure 2 illustrates the effect of the content of helium and heavy admixture on the behavior of adiabatic compressibility. Pairs of lines connected by arrows show that an increase in the content of both helium and heavy elements reduces adiabatic compressibility. However, the "standard" chemical composition of the solar plasma corresponds to the solid line ($Z = 0.02$ and $X = 0.7$), which underestimates helioseismic data. The assumption of the low content of heavy elements ($Z = 0.00$) leads to considerable difficulties when comparing them with other astrophysical data.

Figure 3 shows the adiabatic compressibility index obtained from the inversion of helioseismic data [1] in comparison with data taken from [4, 13], SAHA-S data ($Z = 0.02$), and our calculations with the refined com-

position of heavy elements including silicon and iron. Heavy elements were 2% in mass and included 17.6% carbon, 5.2% nitrogen, 50.2% oxygen, 9.7% neon, 9.8% silicon, and 7.5% iron. Figure 3 shows that the inclusion of silicon and iron into admixtures (instead of simplified change of these elements to neon) is noticeable from the viewpoint of agreement with helioseismic data. Our model agrees well with models presented in [4, 13] in the theoretical description of nonideality in this temperature region.

Thus, the use of the SAHA-S equation of state makes it possible to calculate the internal structure and evolution of the Sun and refine (due to high and controllable accuracy of the equation of state) the composition and general content of heavy elements, which are consistent with helioseismic data.

REFERENCES

1. S. V. Vorontsov, in *Proceedings of 2002 SOHO 12/GONG + 2002, Local and Global Helioseismology: The Present and Future*, Ed. by H. Lacoste (Noordwijk, The Netherlands, 2002), ESA SP-517 SOHO/GONG; in *Proceedings of Workshop on Equation-of-State and Phase-Transition Issues in Models of Ordinary Astrophysical Matter* (Leiden, The Netherlands, 2004).

2. J. Christensen-Dalsgaard, W. Dappen, S. V. Ajukov, *et al.*, Science **272**, 1286 (1986).

3. A. A. Likal'ter, Zh. Éksp. Teor. Fiz. **56**, 240 (1969) [Sov. Phys. JETP **29**, 133 (1969)].

4. F. Rogers, F. Swenson, and G. Iglesias, Astrophys. J. **456**, 902 (1996); F. J. Rogers and A. Nayfonov, Astrophys. J. **576**, 1064 (2002).

5. A. A. Vedenov and A. I. Larkin, Zh. Éksp. Teor. Fiz. **36**, 1133 (1959) [Sov. Phys. JETP **9**, 806 (1959)].

6. A. I. Larkin, Zh. Éksp. Teor. Fiz. **38**, 1896 (1960) [Sov. Phys. JETP **11**, 1363 (1960)].

7. W. Ebeling, W.-D. Kraeft, and D. Kremp, *Theory of Bound States and Ionisation Equilibrium in Plasmas and Solids* (Akademie, Berlin, 1976; Mir, Moscow, 1979).

8. W.-D. Kraeft, D. Kremp, W. Ebeling, and G. Röpke, *Quantum Statistics of Charged Particle Systems* (Plenum, New York, 1986; Mir, Moscow, 1988).

9. V. P. Kopyshev, Zh. Éksp. Teor. Fiz. **55**, 1304 (1968) [Sov. Phys. JETP **28**, 684 (1969)].

10. G. É. Norman and A. N. Starostin, Teplofiz. Vys. Temp. **8**, 413 (1970).

11. A. N. Starostin, V. C. Roerich, and R. N. More, Contrib. Plasma Phys. **43**, 369 (2003).

12. V. K. Gryaznov, I. L. Iosilevskiĭ, and V. E. Fortov, in *Shock Waves and Extremal States of Substance*, Ed. by V. E. Fortov, L. V. Al'tshuler, R. F. Trunin, and A. I. Funtikov (Nauka, Moscow, 2000), p. 299 [in Russian].

13. W. Dappen, D. Hummer, and D. Mihalas, Astrophys. J. **331**, 794 (1988); **331**, 815 (1988); **332**, 261 (1988).

Translated by R. Tyapaev

Testing the Correlations between Ultrahigh-Energy Cosmic Rays and BL Lac–Type Objects with HiRes Stereoscopic Data[¶]

D. S. Gorbunov[1,]*, P. G. Tinyakov[1, 2], I. I. Tkachev[1, 3], and S. V. Troitsky[1]

[1] Institute for Nuclear Research, Russian Academy of Sciences, Moscow, 117312 Russia
* e-mail: gorby@ms2.inr.ac.ru
[2] Service de Physique Théorique, CP 225, Université Libre de Bruxelles, B-1050 Brussels, Belgium
[3] CERN Theory Division, CH-1211 Geneva 23, Switzerland
Received June 21, 2004

Abstract—Previously suggested correlations of BL Lac–type objects with the arrival directions of the ultrahigh-energy cosmic ray primaries are tested by making use of the HiRes stereoscopic data. The results of the study support the conclusion that BL Lacs may be cosmic ray sources and suggest the presence of a small (a few percent) fraction of neutral primaries at $E > 10^{19}$ eV. © 2004 MAIK "Nauka/Interperiodica".

PACS numbers: 98.54.Cm; 98.70.Sa

1. MOTIVATION

With the exception of a small number of highest-energy events, the bulk of ultrahigh-energy cosmic rays (UHECRs) is most naturally explained by acceleration in active galaxies [1–3]. This explanation is supported by clustering of UHECRs observed in the AGASA and Yakutsk datasets [4–6][1] and by correlations between arrival directions of UHECRs and a particular class of active galactic nuclei, the BL Lacertae objects (BL Lacs) [11–13] (see also [14]).

The correlations with BL Lacs were observed in AGASA and Yakutsk datasets. To test them, *independent* datasets are needed. Such a dataset has been recently published by the HiRes collaboration [8]. It consists of 271 events with reconstructed energy $E > 10^{19}$ eV which were observed in the stereoscopic mode. The energies of the events are not published; this makes reconstruction [12] of arrival directions in the Galactic magnetic field impossible. Despite the small exposure of HiRes in the stereo mode as compared to AGASA, the excellent angular resolution of 0.6° makes HiRes data quite competitive (or even superior) in testing correlations with BL Lacs under the assumption of neutral primary particles. This test is the purpose of the present work. More precisely, we take three previously studied sets of BL Lacs without any further selection and test them for correlations with the entire set of 271 HiRes events.

2. FLUCTUATIONS OF CORRELATION SIGNAL

At the current low statistics, the correlation signal is not expected to be robust [5]. To illustrate this important point, consider the following example. Assume that a given set of sources in a given exposure time produces five events on average. Let the average number of rays coincident with sources by chance be two. The *average* number of correlating rays observed in such an experiment would therefore be seven. Both the real events from sources and background chance coincidences are Poisson distributed. Thus, in a particular realization, the number of correlating rays would vary roughly within $7 \pm \sqrt{7}$. It is therefore likely that two identical experiments will see ten and four correlating rays, respectively. The first one would see a strong correlation signal (ten events at two expected with the hypothesis of no correlations; probability $p \sim 5 \times 10^{-5}$, and the second one would see a signal compatible with the uniform background (four events at two expected, $p \sim$ 14%).

It is worth stressing that, in this situation, the final conclusion would be that the *correlation exists*, because the first of the two experiments is incompatible with uniform background (while both are compatible with the signal). Thus, at present small statistics, one *should* expect that some of the experiments see no correlations. Such fluctuations indeed exist, e.g., in the autocorrelation signal [4, 8].

3. BL LAC SAMPLES

There were three samples of BL Lacs discussed in the literature, all three drawn from the catalog of quasars and active galactic nuclei [15]:

[¶] This article was submitted by the authors in English.

[1] HiRes collaboration does not observe significant clustering [7, 8], but, at the present level of statistics, this does not contradict the previous results [9, 10].
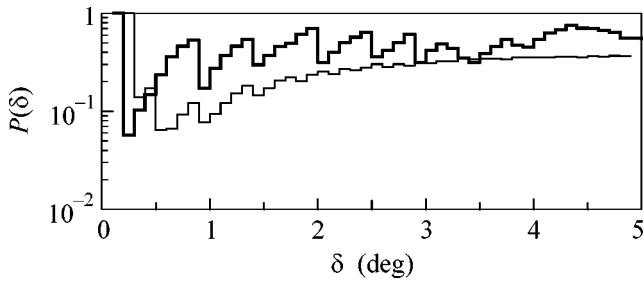
Fig. 1. $P(\delta)$ for the set of 22 BL Lacs and HiRes stereo events. The thick line shows data, and the thin line shows $P_{th}(\delta)$ obtained in the Monte Carlo simulations in which two events are from the BL Lac sources.

Fig. 2. $P(\delta)$ for the set of 14 BL Lacs and HiRes stereo events. The thick line shows data, and the thin line shows $P_{th}(\delta)$ obtained in the Monte Carlo simulations in which two events are from the BL Lac sources.
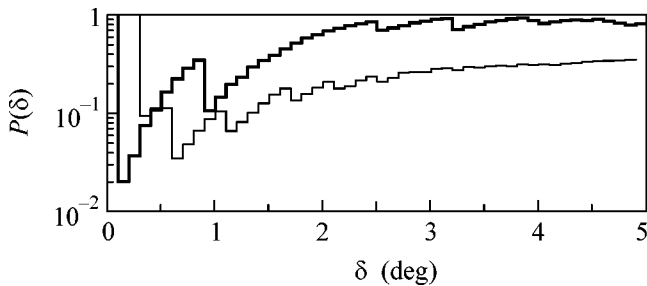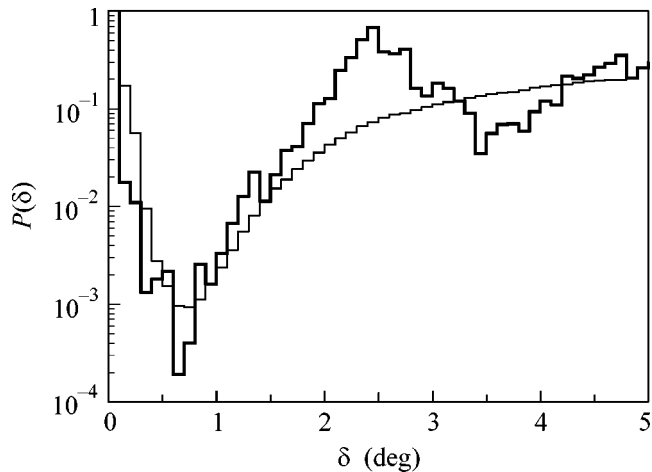

Fig. 3. $P(\delta)$ for the set of 156 BL Lacs and HiRes stereo events. The thick line shows data, and the thin line shows $P_{th}(\delta)$ obtained in the Monte Carlo simulations in which nine events are from the BL Lac sources.

(1) The set of 22 most powerful BL Lacs [11]. This set was found by adjustment of cuts on magnitude and radio flux in the catalog of confirmed BL Lacs using the

requirement of the best correlation signal with the most clustered subset of AGASA and Yakutsk cosmic ray events. Neutral primaries were assumed.

(2) The set of 14 BL Lacs which contains potentially γ-ray-loud objects [13]. This subset was obtained by the positional cross-correlation of confirmed BL Lacs with the catalog of EGRET sources [16]. Both assumptions of neutral and charged primary particles were tested using the most clustered subset of AGASA and Yakutsk events.

(3) The set of all confirmed BL Lacs with the single cut on visual magnitude, mag < 18 [12]. This set of BL Lacs contains 156 objects. Both neutral and charged primaries were tested using the whole available set of AGASA events, $E > 4 \times 10^{19}$ eV. Better correlations were found under the assumption of positively charged primary particles.

Note that subsets (1)–(3) are not independent. BL Lacs which correlate with the UHECRs in set (1) are also present in set (2). The cut on magnitude, mag < 18, being the single cut for set (3), is also imposed in set (1) among other cuts.

4. PROCEDURE

Our analysis is based on the calculation of the angular correlation function by means of the algorithm described in [11]. The statistical significance of correlation is estimated by testing the hypothesis that the UHECRs and BL Lacs are uncorrelated. This is done as follows. For a given set of sources and the angle δ, we count the number of pairs "cosmic ray–source" separated by an angular distance less or equal δ, thus obtaining the "data count." We then replace the real data by a randomly generated Monte Carlo set of cosmic rays and calculate the number of pairs in the same way, thus obtaining the "Monte Carlo count." We repeat the latter procedure many times, noting cases when the Monte Carlo count equals or exceeds the data count. The number of such cases divided by the total number of tries gives the probability $P(\delta)$, which characterizes the significance of correlations at a given angular scale δ. The smaller this probability, the stronger (more significant) the correlation.

The Monte Carlo events are drawn from the isotropic distribution according to the acceptance of a given UHECR detector. For the HiRes experiment in the stereo mode, we use the zenith-angle and azimuth-angle distributions given in [17] and the sidereal time distribution published in [18].

The probability $P(\delta)$ depends on the choice of δ. The optimal value of δ is clearly the one where the *expected* signal is strongest (e.g., expected $P_{th}(\delta)$ is lowest). In the case of point sources and neutral primary particles, the shape of $P_{th}(\delta)$ can be calculated by the following Monte Carlo simulation. We start by generating a cosmic ray set which is artificially correlated with BL Lacs. This is achieved by replacing a given (small)

Cosmic rays and BL Lacs from the sample of 156 objects separated by less than 1°. Note that SBS 1508 + 561 correlates with two rays

Cosmic ray		BL Lac	
α, deg	δ, deg	name	z
17.8	–12.5	RBS 161	0.234
48.5	5.8	RX J03143 + 0620	?
118.7	48.1	TXS 0751 + 485	?
123.8	57.0	RX J08163 + 5739	?
137.2	33.5	Ton 1015	0.354
162.6	49.2	MS 10507 + 4946	0.140
169.3	25.9	RX J11176 + 2548	0.360
209.9	59.7	RX J13598 + 5911	?
226.5	56.5	SBS 1508 + 561	?
229.0	56.4	SBS 1508 + 561	?
253.7	39.8	RGB J1652 + 403	?
265.3	46.7	OT 465	?
300.2	65.1	1ES 1959 + 650	0.047

number of events in a random set by the events correlated with randomly chosen BL Lacs. To generate an event correlated with the BL Lac, we assume the two-dimensional Gaussian distribution normalized in such a way that a circle of a radius of 0.6° around the BL Lac contains 68% of the events. The resulting correlated set is then treated as the real data; i.e., the probability $P(\delta)$ is calculated. The bin-by-bin median values of the probabilities obtained for many different sets give $P_{th}(\delta)$. In the real data, following [19], we measure correlations at that value of δ where $P_{th}(\delta)$ is minimal.

5. RESULTS

In Fig. 1–3 we present the expected (thin line) and observed (thick line) $P(\delta)$ for the HiRes dataset of UHECRs and three samples of BL Lac objects described in Section 3. There are no significant correlations with the subsets of 22 and 14 BL Lacs. In both cases only two BL Lacs contribute, to data counts within 1 degree. In the subset of 22 BL Lacs, these are TXS 0751 + 485 and OT 465 (the latter object was among 5 BL Lacs which contribute to correlations in [11]). In the subset of 14 BL Lacs, the two contributing objects are PKS 1604 + 159 and 1ES 1959 + 650. It is worth mentioning that 1ES 1959 + 650 is a confirmed TeV source and contributes to correlations in [13].

The set of 156 BL Lacs with mag < 18 shows rather strong correlation. We list in the table the cosmic rays and BL Lacs separated by less than 1°. The expected probability $P_{th}(\delta)$ has a minimum at $\delta = 0.8$. At this value of δ, the real data give the probability $P(0.8) = 4 \times 10^{-4}$. The data count is 11, while the Monte Carlo expectation due to random uncorrelated background is

~3. This corresponds to about 8 events from sources in the overall HiRes data sample of 271 events. Thus, a ~3% fraction of neutral particles in the total cosmic ray flux may be sufficient to explain this correlation. This is consistent with the fraction of clustered events observed by AGASA at these energies [20].

6. CONCLUSIONS

We have assumed—as a "null-hypothesis"—that BL Lacs and the new HiRes stereo data are uncorrelated. We have tested this hypothesis for three particular subsets of BL Lacs studied previously and found an excess of pairs "BL Lac–cosmic ray" in one of them, which would occur with a probability of 4×10^{-4} for a random set of UHECRs. If these sets were independent, the final significance would be the best probability found multiplied by the number of tries. Since the samples are not independent, the penalty factor is smaller. In any case, the null-hypothesis is rejected with a probability of ~10^{-3}. Our analysis thus confirms the association of UHECRs with BL Lacs.

Only one of the three examined subsets of BL Lacs—the largest one—shows significant correlations. This may indicate that those BL Lacs which are sources have similar and small luminosity in UHECRs. This conclusion is also consistent with the statistics of the clustering of UHECR events, which suggests a few hundred sources currently contributing to the UHECR flux, see [10, 21, 22].

The observation of correlations at angles much smaller than the typical deflection of a charged UHECR particle in the Galactic magnetic field suggests that (at least) a few percent of UHECRs are neutral.

REFERENCES

1. V. S. Berezinsky *et al.*, *Astrophysics of Cosmic Rays*, Ed. by V. L. Ginzburg, 2nd ed. (Nauka, Moscow, 1990; North-Holland, Amsterdam, 1990).

2. J. P. Rachen and P. L. Biermann, Astron. Astrophys. **272**, 161 (1993).

3. V. Berezinsky, A. Z. Gazizov, and S. I. Grigorieva, hep-ph/0204357.

4. M. Takeda *et al.* (AGASA Collab.), Astrophys. J. **522**, 225 (1999).

5. P. G. Tinyakov and I. I. Tkachev, Pis'ma Zh. Éksp. Teor. Fiz. **74**, 3 (2001) [JETP Lett. **74**, 1 (2001)].

6. C. B. Finley and S. Westerhoff, astro-ph/0309159.

7. R. U. Abbasi *et al.* (The High Resolution Fly's Eye Collab.), astro-ph/0404366.

8. R. U. Abbasi *et al.* (The High Resolution Fly's Eye Collab.), astro-ph/0404137.

9. H. Yoshiguchi, S. Nagataki, and K. Sato, astro-ph/0404411.

10. M. Kachelriess and D. Semikoz, astro-ph/0405258.

11. P. G. Tinyakov and I. I. Tkachev, Pis'ma Zh. Éksp. Teor. Fiz. **74**, 499 (2001) [JETP Lett. **74**, 445 (2001)].

12. P. G. Tinyakov and I. I. Tkachev, Astropart. Phys. **18**, 165 (2002).

13. D. S. Gorbunov *et al.*, Astrophys. J. **577**, L93 (2002).

14. A. V. Uryson, in *Proceedings of 27th ICRC* (Hamburg, 2001), p. 551.

15. M. P. Véron-Cetty and P. Véron, ESO Scientific Report (2000); Astron. Astrophys. **374**, 92 (2001).

16. R. C. Hartman *et al.*, Astrophys. J., Suppl. **123**, 79 (1999).

17. R. W. Springer, *Presentation at the 29th ICRC* (Tsukuba, 2003).

18. B. T. Stokes, C. C. H. Jui, and J. N. Matthews, Astropart. Phys. **21**, 95 (2004).

19. P. Tinyakov and I. Tkachev, astro-ph/0301336.

20. M. Takeda (for the AGASA Collab.), in *Proceedings of 27th ICRC* (Hamburg, 2001), Vol. 1, p. 341.

21. S. L. Dubovsky, P. G. Tinyakov, and I. I. Tkachev, Phys. Rev. Lett. **85**, 1154 (2000).

22. P. Blasi and D. De Marco, Astropart. Phys. **20**, 559 (2004); astro-ph/0307067.

Search for the Emission of π⁰ Mesons from the Neutron-Induced Fission of ²³⁵U Nuclei

V. A. Varlachev, G. N. Dudkin*, Yu. F. Krechetov, V. N. Padalko, and E. N. Shuvalov

Research Institute of Nuclear Physics, Tomsk Polytechnic University, Tomsk, 634050 Russia

* e-mail: dudkin@npi.tpu.ru

Received June 23, 2004

A nuclear-reactor experiment on the search for the emission of neutral pions from the neutron-induced fission of ²³⁵U nuclei has been carried out. To this end, an experimental setup for searching for the emission of π⁰ mesons with high sensitivity to this process has been designed and produced. This setup consisted of two Cherenkov total-absorption spectrometers for the detection and measurements of the energy of two gamma-ray photons from π⁰-meson decay. The spectrometers were placed at the exits of two coaxial horizontal experimental channels. To protect the detectors from low-energy β and γ rays and neutron fluxes, 3.5-m-long water filters were situated in the channels. To reject the cosmic background, large-area scintillation counters operating in the anticoincidence mode were placed over each spectrometer. The energy and time resolution of the spectrometers, as well as the efficiency of detecting charged particles by scintillation counters, were tested on the secondary electron beam of the Tomsk electron synchrotron Sirius. Runs of measurements of the effect on the operating reactor (duration of 805 h) were alternated with runs of measurements of background on the stopped reactor (duration of 403 h). Statistical processing of the experimental results yields an upper limit of $\leq 5.3 \times 10^{-12}$ with a 90% confidence level for the probability of the emission of neutral pions from the neutron-induced fission of ²³⁵U nuclei. This result and results of other works carried out with sources of spontaneously fissioning ²⁵²Cf nuclei show that the probabilities of the emission of π⁰ mesons from spontaneous fission and fission induced by fission-spectrum neutrons are equal to each other. © 2004 MAIK "Nauka/Interperiodica".

PACS numbers: 25.85.Ec

It is known that the fission of heavy nuclei ($Z > 92$) is accompanied by the release of an energy of about 200 MeV, which is sufficient for the production of a π⁰ meson. This process is not forbidden by the energy–momentum conservation law. However, it is suppressed by barrier effects in conventional models and has vanishingly low probability [1].

Ion *et al.* [2] proposed a statistical nuclear model treating a heavy nucleus ($Z > 92$) as a hot sphere with the admixture of the relativistic pion gas with the Bose–Einstein distribution. The probabilities P_m/P_f of the emission of neutral pions (yield of pions per fission event) from the fission of certain nuclei were calculated in the framework of this model. The probability of "pionic radioactivity" was shown to strongly depend on the model parameters such as the nuclear excitation energy and the corresponding temperature. In particular, for the spontaneously fissioning nucleus ²⁵²Cf, the probability of pionic radioactivity varies from 1.8×10^{-14} to 7.3×10^{-7} when nuclear temperature varies from 1.3 to 1.6 MeV. After publication of theoretical works [2], experiments on the search for pionic radioactivity from nuclear fission were carried out with sources of ²⁵²Cf spontaneously fissioning nuclei. With a 90% confidence level, the following upper limits P_m/P_f on the emission of π⁰ mesons were obtained:

$<5 \times 10^{-9}$ [3], $<10^{-9}$ [4], $<3.3 \times 10^{-10}$ [5], and $<1.4 \times 10^{-11}$ [1].

It is known that spontaneous nuclear fission considerably differs from neutron-induced fission, because the fission of a nucleus in the latter case proceeds through an intermediate highly excited state. This circumstance can affect the probability of emission of pions or other high-energy particles from the nucleus undergoing induced fission. In particular, Il'inov and Mebel' [6] assumed that the probability of the emission of π mesons from induced fission can be higher than from spontaneous fission by many orders of magnitude. The authors of that theoretical work proposed to investigate the π channel of proton-induced nuclear fission (fission accompanied by the emission of pions) for energies below the threshold of the formation of π mesons on nuclei. The authors of that work calculated the total cross sections, as well as the angular and differential distributions of pions, in the cascade–evaporation–fission model developed by them and showed that the cross section for the π channel is rather large. It is intended to build an experimental setup for searching π fission on the proton beam at the Moscow meson factory.

Nikolenko *et al.* [7] attempted to observe the yield of high-energy γ rays (>30 MeV) from the induced fission of ²³⁹Pu and ²³⁵U nuclei at the JINR pulsed nuclear
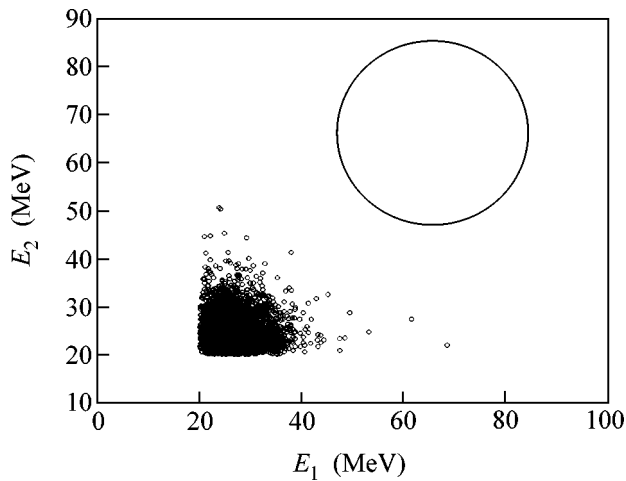
Fig. 1. Distribution of events in the two-dimensional energy region for the stopped reactor.

reactor (Dubna). However, the relatively weak limitation $P_\gamma/P_f \leq 3 \times 10^{-8}$ on the probability of emission of high-energy γ rays was established in the experiment. At the same time, the detection of rare processes accompanying the fission of ordinary nuclei or the determination of stronger limitation on the existence of such processes is important for expanding our knowledge of nuclear-matter structure and the nuclear-fission mechanism. For this reason, the main goal of this work was searching for the emission of π^0 mesons from the neutron-induced fission of ^{235}U nuclei at a setup with high sensitivity to this process.

When developing the project of the experiment, we assumed that the emission of π^0 mesons with low kinetic energy is the most probable process. In this case, the scattering angle between γ-ray photons is close to 180°, and their energy is equal to $E_\gamma = 67.5$ MeV. The experimental setup was based on two Cherenkov total-absorption spectrometers (CTASs) [8] for the coincidence detection and measurement of the energy of two γ-ray photons from the decay of π^0 mesons. These spectrometers were placed at the exits of horizontal experimental channels of the nuclear reaction at the Research Institute of Nuclear Physics, Tomsk Polytechnic University, with a maximum power of 6 MW. The axes of the channels intersect each other at an angle of 177.3° ± 1.2° near the center of the active zone of the reactor. The distance between the spectrometers is equal to 9.5 m. To reject the cosmic background, large-area scintillation counters operating in the anticoincidence mode are placed over each spectrometer [9]. The efficiency of charged particles being detected by the scintillation counters, which is measured for cosmic-ray muons, amounts to 0.97. To protect the CTASs from low-energy β and γ rays and neutron fluxes from the active zone of the reaction, 350-cm-long water filters were placed in the channels. Measurements showed that the background conditions

are as follows: the γ radiation exposition dose rate is equal to 30 μR/s and the flux density of fast and thermal neutrons is less than 1 neutron/cm² s. The anode current of photomultipliers was equal to 1.4 μA. To simulate the background load when measuring with the stopped reactor, the CTASs were equipped with light-emitting diodes, which enabled one to generate constant-level illumination of photomultipliers. The energy and time calibrations of the CTAS were carried out with the secondary monoenergetic electron beam of the Sirius synchrotron at energies 41, 66, and 97 MeV. Since the background radiation from the active zone of the reactor deteriorates the energy and time resolution of the spectrometers, their calibration was carried out upon the one-photon illumination of the photocathodes of the photomultiplier at an anode current of 2 μA. The amplitude resolution of both spectrometers for an energy of 66 MeV is equal to 20%, and the time resolution is equal to 2.0 ns (rms deviations are given). Signals from the Cherenkov detectors and scintillation counters after amplification were applied to pulse formers and further to the programmable scheme of the event selection, which plays the role of a built-in trigger. The scheme forms the start signal if signals from the CTASs coincide within the time interval (τ = ±50 ns) in the absence of signals from the scintillation counters. The amplitudes of signals from the CTASs and scintillation counters were measured by a charge-to-digital converter. The time interval between signals from the CTASs was converted into code by a time encoder. The monitoring system was based on the programmable generator and high-stable carbide–silicon light-emitting diodes placed in each detector [10]. Additional independent continuous control over the stability of the amplitude sections and optical part of the CTASs was carried out by periodic measurements of the maximum of the amplitude distribution of pulses from cosmic rays.

Measurements were carried out in 2002–2003. Runs of measurements on the operating reactor were alternated with runs of measurements of radiation and cosmic background with the stopped reactor. In order to conserve the conditions of background measurements, the photomultipliers of the Cherenkov spectrometers were illuminated by dc light-emitting diodes with the illumination level ensuring approximately the same counting rate from the pulse formers of the Cherenkov spectrometers as with the operating reactor. Figure 1 shows the results of measurement of radiation and cosmic backgrounds with the stopped reactor for a total duration of 403 h. The circle shows the region of γ-ray energies from expected events of the decay of π^0 mesons with a confidence level of 0.9 in the approximation of two-dimensional Gaussian distribution with the mean value $E_{\gamma_{1,2}} = 67.5$ MeV and $\sigma_{\gamma_{1,2}} = 13.5$ MeV. Moreover, additional selection was carried out by selecting pulses from the CTASs in a time interval of ±6 ns. Figure 2 shows the results of measurements of
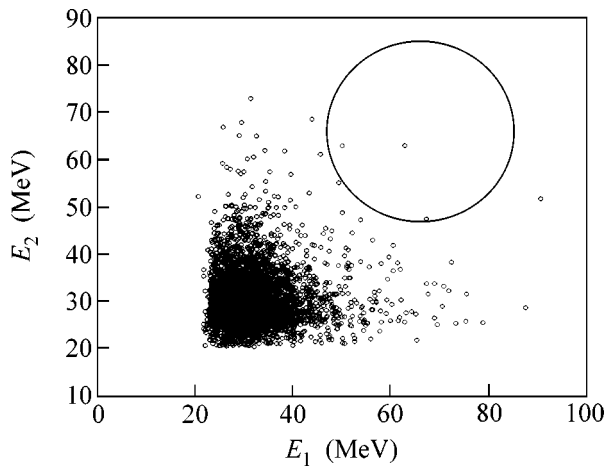
Fig. 2. Distribution of events in the two-dimensional energy region for the operating reactor.

the effect on the operating reactor with a 805-h total duration of accumulated statistics. It is seen that three events fall within the selected region of detected π^0 mesons. It is worth noting that the energy spectrum of γ-rays from the active zone of the reactor is rather hard, and events falling within the selected region can be attributed to random coincidences. Therefore, the results provide only an upper limit on the probability of emitting π^0 mesons from the neutron-induced fission of ^{235}U nuclei:

$$\frac{P_m}{P_f} \leq \frac{4\pi n}{GT\Omega k_1 k_2}. \tag{1}$$

Here, $G = 5.3 \times 10^{15}$ event/s is the calculated intensity of nuclear fission in that part of the active zone of the reactor which is scanned through coaxial channels, $T = 2.89 \times 10^6$ s is the effect measurement time, $\Omega = 3.3 \times 10^{-4}$ sr is the calculated effective solid angle of detecting π^0 mesons under the assumption that π^0 mesons are formed with almost zero kinetic energy, $k_1 = 2.2 \times 10^{-6}$ is the calculation coefficient representing the absorption of γ rays from the decay of a π^0 meson in the active zone of the reactor and water filters, $k_2 = 0.9$ is the coef-

ficient that accounts for the loss of events upon the energy cutoff of the π^0-meson detection region, and $n < 4.2$ is the upper limit on the number of detected π^0 mesons at a 90% confidence level. This limit was obtained by the Poisson statistical analysis of data [11] (three events were detected in the presence of three background events). As a result, $P_m/P_f \leq 5.3 \times 10^{-12}$ with a 90% confidence level. This result shows that the probabilities of emission of π^0 mesons from spontaneous fission and fission induced by fission-spectrum neutrons are equal to each other.

REFERENCES

1. J. N. Knudson, C. L. Morris, J. D. Bowman, *et al.*, Phys. Rev. C **47**, 2869 (1991).
2. D. B. Ion, R. Ion-Mihai, M. L. Ion, and A. I. Sandru, *Spontaneous Pion Emission during Fission as a New Nuclear Radioactivity*; nucl-th/0310056 v.1 (2003).
3. C. Cerruti, J. M. Hisleur, and J. Julien, Z. Phys. A **329**, 383 (1988).
4. J. R. Beene, C. E. Bemis, and M. L. Halbert, Phys. Rev. C **38**, 569 (1988).
5. S. Stanislaus, D. S. Armstrong, and D. F. Measday, Phys. Rev. C **39**, 295 (1989).
6. A. S. Il'inov and M. V. Mebel', Yad. Fiz. **64**, 1463 (2001) [Phys. At. Nucl. **64**, 1386 (2001)].
7. V. G. Nikolenko, A. B. Popov, G. S. Samosvat, and Hvan Cher Gu, Pis'ma Zh. Éksp. Teor. Fiz. **27**, 65 (1978) [JETP Lett. **27**, 59 (1978)].
8. G. N. Dudkin, V. N. Eponeshnikov, and Yu. F. Krechetov, Prib. Tekh. Éksp., No. 2, 64 (1973).
9. Yu. V. Vasil'chenko, A. N. Gulida, G. N. Dudkin, and V. N. Padalko, Prib. Tekh. Éksp., No. 2, 36 (1998).
10. S. V. Bryanskiĭ and V. N. Padalko, Prib. Tekh. Éksp., No. 1, 82 (1995).
11. Phys. Rev. D **54**, 166 (1996).

Translated by R. Tyapaev

Topological Noise Scalings in Superfluid and Classical Turbulence¶

D. Kivotides

Low Temperature Laboratory, Helsinki University of Technology, FIN-02015 HUT, Finland
e-mail: demos@galcit.caltech.edu
Received July 2, 2004

Abstract—We calculate the topological noise characterizing the direction of line vortices in superfluid and classical turbulence by finding the intersection of line vortices with square surfaces of edge length l_s positioned normal to three orthogonal axes. In the case of homogeneous superfluid turbulence in thermal counterflow, we find that the noise scales as l_s along the two directions normal to the counterflow and as $l_s^{3/2}$ along the direction parallel to it. In homogeneous isotropic superfluid turbulence, at $T \longrightarrow 0$ K, the noise scales as $l_s^{7/4}$. In homogeneous isotropic classical turbulence, the scaling is l_s^2. We offer possible interpretations of the computed scalings, as well as justification for their differences. © *2004 MAIK "Nauka/Interperiodica"*.

PACS numbers: 47.37.+q; 47.27.Sd

Turbulence in thermally excited superfluids involves the interaction of topological defects (line vortices) of collective superfluid motion with thermal excitations of the superfluid ground state (normal fluid) via mutual friction forces. In the related field of classical turbulence, a quantized model of Navier–Stokes turbulence was developed in which all flow vorticity is in the form of classical vortex filaments (schoinoidal turbulence). The model was found to reproduce central aspects of classical turbulence phenomenology like Kolmogorov scalings for the second and third order structure functions [1], Navier–Stokes turbulence kinematics [2], and geometrical aspects of turbulent vorticity [3]. Definitely, in all cases the geometry of the vortices is of paramount importance. However, much less detailed information might be of importance in cases where gross properties of the system are of interest [4–6]. For example, the (topological) noise characterizing the direction of vortices intersecting a particular surface dividing the fluid volume in two provides information about the net vorticity flux through the surface. Moreover, noise scalings are important in the context of quantum field theory (condensed matter and high energy physics), where changes in asymptotic scaling behavior mark phase transitions [7]. In this letter, we investigate whether topological noise scalings exist in the context of flow turbulence and how they might be affected by the equations of motion. We study three different flow situations: (a) homogeneous superfluid turbulence in thermal counterflow [8, 9], (b) homogeneous isotropic superfluid turbulence at $T \longrightarrow 0$ K [10], and (c) homogeneous isotropic classical turbulence.

¶ This article was submitted by the author in English.

(a) The mathematical system describing thermal counterflow concerns exclusively the quantized vortex dynamics. This is because the counterflow velocity $\mathbf{V}_n - \mathbf{V}_s$ itself (with $\mathbf{V}_n$ being the normal fluid velocity and $\mathbf{V}_s$ being the irrotational part of superfluid velocity) is kinematically imposed. Therefore, although the counterflow affects the line vortex motion, it is unaffected by the latter. If $\mathbf{S}(\xi, t)$ is the three-dimensional representation of the vortex tangle (where ξ is the arclength parametrization along the loops and t is time), then its motion obeys the equation [11]

$$\frac{d\mathbf{S}}{dt} = \mathbf{V}_l = \mathbf{V}_s + \mathbf{V}_{bs} + \alpha_x \mathbf{S}' \times (\mathbf{V}_n - \mathbf{V}_s - \mathbf{V}_{bs})$$
$$- \alpha_{xx} \mathbf{S}' \times [\mathbf{S}' \times (\mathbf{V}_n - \mathbf{V}_s - \mathbf{V}_{bs})], \quad (1)$$

where the rotational part of superfluid velocity $\mathbf{V}_{bs}$ is given by the Biot–Savart integral:

$$\mathbf{V}_{bs}(\mathbf{x}) = -\frac{\kappa}{4\pi} \int d\xi \frac{\mathbf{S}' \times (\mathbf{S} - \mathbf{x})}{|\mathbf{S} - \mathbf{x}|^3}. \quad (2)$$

Here, $\mathbf{x}$ is the space coordinate, κ is the quantum of circulation, $\mathbf{S}' = d\mathbf{S}/d\xi$ is the unit tangent vector, and α_x, α_{xx} are the mutual friction coefficients.

The working fluid is ⁴He and the temperature $T = 1.3$ K. Under these conditions, $\kappa = 9.97 \times 10^{-4}$ cm²/s, the density of the normal fluid is $\rho_n = 6.5 \times 10^{-3}$ g/cm³, the density of the superfluid is $\rho_s = 138.6 \times 10^{-3}$ g/cm³, the normal fluid viscosity is $\nu = 23.30 \times 10^{-4}$ cm²/s, $\alpha_x = 3.4145 \times 10^{-2}$, and $\alpha_{xx} = 1.3703 \times 10^{-2}$. The computation is done in a box of size $l_b = 0.1$ cm with periodic boundary conditions to enforce homogeneity. The

velocities $\mathbf{V}_n$ and $\mathbf{V}_s$ are prescribed to be parallel to the y axis. We prescribe the Reynolds number of the normal fluid Re $= |\mathbf{V}_n|l_b/\nu$ at $t = 0$ to be Re $= 50$. This specifies $|\mathbf{V}_n| = 0.6408$ cm/s, and using the continuity equation $\rho_s\mathbf{V}_s + \rho_n\mathbf{V}_n = 0$, we find $\mathbf{V}_s = -(\rho_n/\rho_s)\mathbf{V}_n$ with $|\mathbf{V}_s| = 0.030146$ cm/s. Then, by specifying the initial geometry of the tangle (which at $t = 0$ consists of ten randomly positioned rings of length $L_0 = 2.1608$ cm), one can calculate the evolution of the tangle using numerical methods. We choose the discretization length $\Delta\xi$ along the line vortices to be $\Delta\xi = 2.0833 \times 10^{-3}$ cm and the numerical time step Δt to be small enough so that no possible (resolved by $\Delta\xi$) Kelvin wave in the system propagates more than $\Delta\xi$ during Δt. This requirement leads to typical time steps $\Delta t \approx 0.001$ s. Finally, when two vortices approach closer than $\Delta\xi$, they reconnect. This methodology is supported by the results of [12, 13].

Knowledge at each time step of the tangle's configuration allows the calculation of topological number noise. The following algorithm was developed for this purpose. First, the average intervortex distance $l_\zeta = (L/l_b^3)^{-1/2}$ is defined. Subsequently (for sufficiently dense tangles), a range of length sizes is specified $[ml_\zeta, l_b]$, with m being a small natural number ($m = 4$ in the present calculation). A sequence of lengths l_s ($ml_\zeta < l_s < l_b$) is generated by dividing $[ml_\zeta, l_b]$ into n subintervals ($n = 100$ in this computation). Each of the lengths l_s in this sequence is taken to be the edge of a square surface positioned normal to each axis in due order of succession. For each choice of edge length and axis, we consider k surfaces ($k = 1000$ in this calculation). The position of each square surface center is defined using random numbers for the coordinates. For every surface, we determine the intersection points with the vortex tangle. In doing this, we attribute to every intersection point a topological number $+1$ or -1, depending on whether the vorticity vector is pointing towards one or the other of the two halves of the fluid volume that the surface delimits. In this work, the number $+1$ is used when vorticity points towards the positive part of an axis. We call these numbers topological because they characterize the direction of the vorticity vector along the line vortex and this direction, as well as the vortex itself, persists in time due to the topological nature of the defects. We define N^+ to be the sum of points associated with topological number $+1$ and in a similar way we define N^-. In the end, the exercise mentioned above attributes to each surface the quantity $N^+ - N^-$, which represents the net number of vorticity vectors that thread the surface possessing one of the two possible orientations. By squaring this quantity and averaging over the number k of surfaces of edge l_s normal to the particular axis, we obtain the topological (number) noise $\theta_i(l_s) = \langle (N^+ - N^-)^2 \rangle$, with $i = 1, 3$ representing the three directions.
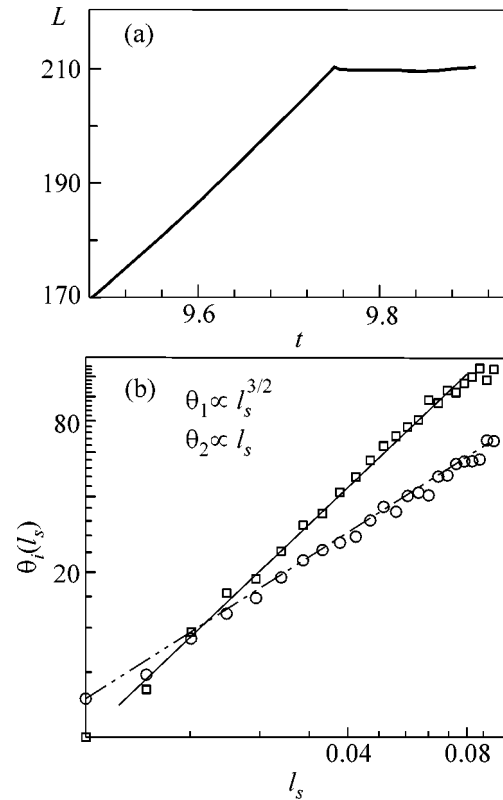

Fig. 1. Results for counterflow turbulence: time evolution of tangle length L (top) and topological noises θ_i as functions of the surface edge length l_s at stoppage time (bottom). Time t is measured in s and L, l_s in cm.

In accordance with the calculations of [14], the counterflow causes a rapid increase in the tangle length L. At $t = 9.7$ s and $L = 182.9$ cm and due to the dramatic increase in the number of vortex particles required by the numerics, the calculation becomes very complex. In response to this, we regulate the magnitude of the counterflow in order to achieve a steady state for L. We find (Fig. 1, top) that, when the Reynolds number is close to Re $= 27.5$, the tangle length becomes to a very good approximation stationary. Definitely, one would like to continue the calculation for longer times while keeping the vortex length approximately constant. However, for the number of particles in the present calculation (typically close to 80×10^3), the Biot–Savart many-body problem is computationally too complex for that. This situation might change in the future with the combination of powerful numerical (tree algorithms) and computational (parallel algorithms) methodologies. It is observed (Fig. 1, bottom) that, over a decade of l_s, θ_1 and θ_2 display the scaling behavior l_s and $l_s^{3/2}$, respectively. We note that θ_2 refers to surfaces normal to the counterflow and that the θ_1 and θ_3 scaling behaviors were identical. The scalings remained unaltered throughout the time interval of approximately constant L. The noise in the counterflow direction seems to be
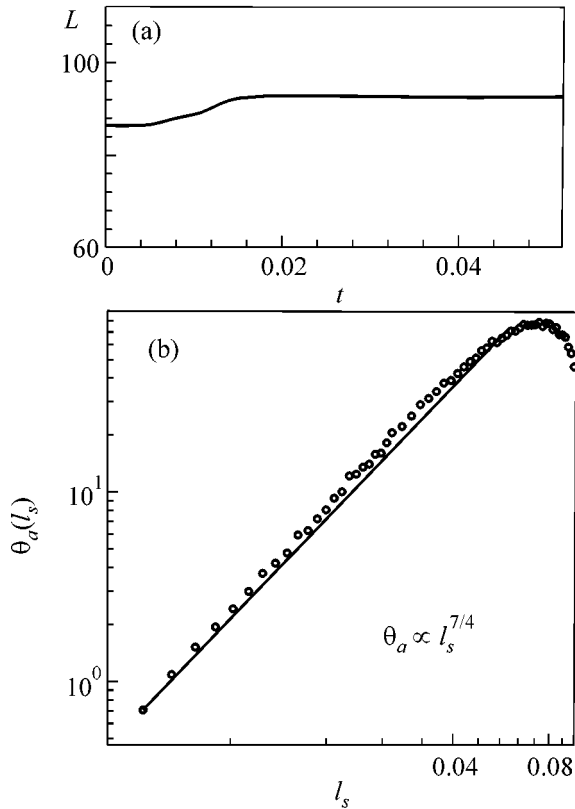
Fig. 2. Results for homogeneous isotropic superfluid turbulence at $T \longrightarrow 0$: time evolution of tangle length L (top) and average of topological noises θ_a as a function of the surface edge length l_s at stoppage time (bottom). Time t is measured in s and L, l_s in cm.

proportional to the measure of a fractal object thicker than a line but still not as extended as a surface.

One can say that the counterflow introduces an anisotropy in the equations of motion. Indeed, in contrast to vortices along the x and z directions, those parallel to $\mathbf{V}_n - \mathbf{V}_s$ do not interact with the counterflow. Therefore, as far as the tangle configuration is concerned, a kind of order is introduced along the normal to the counterflow axes due to the $\mathbf{S}' \times (\mathbf{V}_n - \mathbf{V}_s)$ terms in the equations of motion. As a result, different scalings are observed in different directions, although the particular values of the observed scalings are not *a priori* anticipated. Certainly since $\mathbf{V}_n - \mathbf{V}_s$ drives the turbulence in the system, one should not exclude the possibility that the calculated exponents depend on the counterflow velocity magnitude. How should one interpret the $l_s^{3/2}$ scaling? It is possible that, since the counterflow velocity does not interact with vortices parallel to $\mathbf{V}_n - \mathbf{V}_s$, this scaling is indicative of the situation where $\mathbf{V}_n - \mathbf{V}_s = 0$ but there is still mutual friction. In this case, the only relevant velocity for the determination of the speed of the line vortex is the Biot–Savart one. How-

ever, one can object arguing that the $l_s^{3/2}$ scaling incorporates indirectly the effect of the counterflow due to the interdependence of the vortex dynamics along the three dimensions, which leads to influence from the more orderly vortex states along the other two directions. Certainly, future computations could clarify these important issues.

(b) The mathematical system that describes superfluid turbulence for $T \longrightarrow 0$ in the absence of any irrotational flow component is a subset of Eq. (1):

$$\frac{d\mathbf{S}}{dt} = \mathbf{V}_{bs} \qquad (3)$$

with $\mathbf{V}_{bs}$ defined as in Eq. (2). The size of the box is the same as before, $l_b = 0.1$ cm. The discretization length $\Delta\xi$ along the line vortices is $\Delta\xi = 1.1904 \times 10^{-3}$ cm, and the numerical time step Δt is $\Delta t \approx 0.001$ s. There are initially 700 randomly positioned vortex rings of total length $L = 86.39$ cm. The temporal evolution of L is seen in Fig. 2 (top), indicating a steady state. The latter is not surprising since the superfluid vortex system is conservative and its energy is constant in time, hinting at small variations of the tangle length. Until stoppage time, around 500 reconnections have occurred in the system and 50 time steps were taken. Since (by construction) the flow is homogeneous and isotropic, the topological noises θ_i $i = 1, 3$ were found to be similar in all directions. Therefore, in Fig. 2 (bottom), we plot the arithmetic mean θ_a of the noises θ_i. It is evident that θ_a scales as $l_s^{7/4}$. We have checked that, during the last ten time steps of the computation, the scaling remained invariant. The contrast with the exponents calculated for counterflow turbulence is indicative of the different physics characterizing the two situations.

(c) Finally, the mathematical system that describes (the quantized model) of classical turbulence is also based on the Biot–Savart equation. If $\mathbf{r}_i$ is the three dimensional representation of the center-line curve of filament i, then the vortex motion is described by

$$\frac{d\mathbf{r}_i}{dt} = \mathbf{V}(\mathbf{r}_i(t), t), \qquad (4)$$

where $\mathbf{V}(\mathbf{r}_i(t), t)$ is the Biot–Savart velocity:

$$\mathbf{V}(\mathbf{x}, t) = -\frac{1}{4\pi}\int\frac{(\mathbf{x} - \mathbf{x}') \times \boldsymbol{\omega}(\mathbf{x}')d\mathbf{x}'}{|\mathbf{x} - \mathbf{x}'|^3} \qquad (5)$$

with $\boldsymbol{\omega}(\mathbf{x}')$ being the vorticity vector and $\mathbf{x}'$ denoting points along the core center lines. In the case of superfluid topological defects, $\boldsymbol{\omega}(\mathbf{x}')$ is a delta function along the curve of the vortex C_i since the superfluid vortices have (at hydrodynamic scales) infinitesimal core sizes. However, in the classical Navier–Stokes case, the vortices have dynamic, finite cores and the vorticity is dis-

tributed. Because of this, we employ a more complex vorticity representation [16]:

$$\boldsymbol{\omega}(\mathbf{x}', t) = \sum_i \Gamma \int_{C_i} \frac{1}{\sigma_i(\xi, t)^3} \zeta\left(\frac{|\mathbf{x}' - \mathbf{r}_i(\xi, t)|}{\sigma_i(\xi, t)}\right)$$
$$\times \left(\frac{\partial \mathbf{r}_i}{\partial \xi} + \frac{\mathbf{x}' - \mathbf{r}_i(\xi, t)}{\sigma_i(\xi, t)} \frac{\partial \sigma_i}{\partial \xi}\right) d\xi, \tag{6}$$

where $\sigma_i(\xi)$ is the local core radius of filament i and the smoothing kernel ζ describes the way vorticity spreads around the core center line. There is a variety of smoothing kernels suitable for the computation. The high-order algebraic kernel of [17] is the one used here. A detailed discussion of the numerical analysis and the formulas used can be found in [18]. Γ is the circulation strength attributed to all filaments and is the model's analogue of the quantum of circulation. The formula shows that the vorticity field has two constituents. The first term of the sum inside the integral sign models the vorticity component along the direction of the filament tangent $\partial \mathbf{r}_i/\partial \xi$. This is the only component present in quantum vortices (without the smoothing effect of ζ). The second term models the vorticity component along the direction $\mathbf{x} - \mathbf{r}_i(\xi)$ and is induced by the change of $\sigma_i(\xi)$ along the filaments. The filament cores tend to grow due to diffusive effects. This phenomenon is calculated using the core-spreading method [19]. When two filaments approach within a certain distance from each other, they reconnect. Detailed description of the reconnection methodology can be found in [20].

In order to calculate the topological noises, we use the stoppage time tangle configuration of [3]. In this earlier calculation, the initial conditions consist of 192 rings in a periodic box. The Reynolds number has the value $\text{Re} = \dfrac{\Gamma}{\nu} = 5 \times 10^3$. The results are made dimensionless in the following manner: $t = \dfrac{\Gamma t'}{R^2}$, $\mathbf{x} = \dfrac{\mathbf{x}'}{R}$, $\boldsymbol{\omega} = \dfrac{R^2 \boldsymbol{\omega}'}{\Gamma}$, where t', $\mathbf{x}'$, $\boldsymbol{\omega}'$ are dimensional and R is a reference initial vortex-ring radius. We have chosen $\Gamma = 1$ and $R = 1$; the box size is $l_b = 2.041$. The discretization length $\Delta\xi$ along the line vortices is $\Delta\xi = 4 \times 10^{-2}$, and the numerical time step Δt is $\Delta t \approx 0.0024$. In order to have a stable calculation, the latter is chosen to be the inverse of the maximum average vorticity over the vortex cores. The total evolution time is comparable to the lifetime of the large eddies. The temporal evolution of tangle length L after the artificial initial transient is shown in Fig. 3 (top). As demonstrated in [1], this flow exhibits a Kolmogorov scaling exponent for the energy spectrum. Since the flow is isotropic, we have verified that all three dimensions give identical scalings. In Fig. 3 (bottom), we plot the arithmetic mean θ_a of the
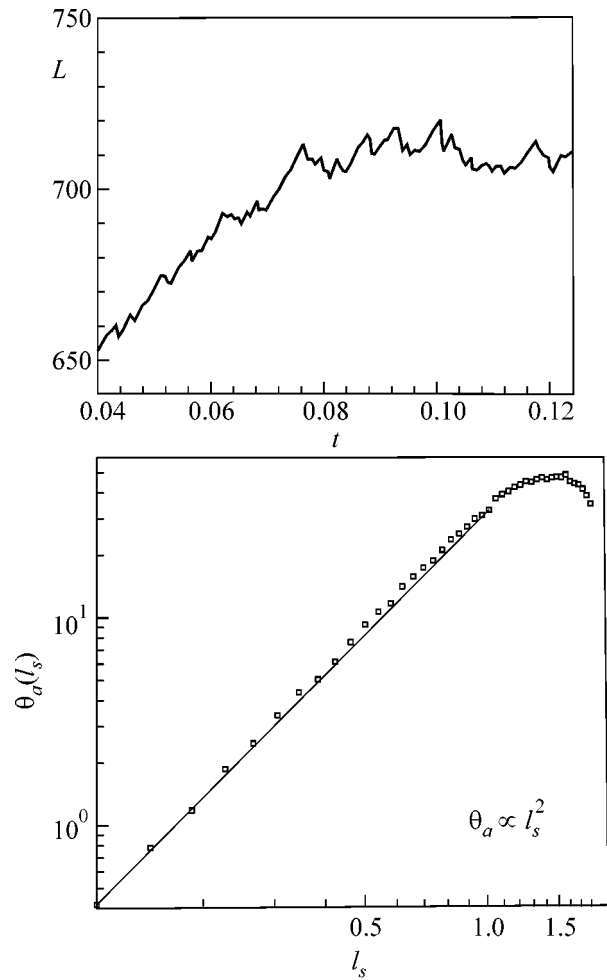

Fig. 3. Results for homogeneous isotropic classical turbulence: time evolution of tangle length L as calculated in [3] (top) and average of topological noises θ_a as a function of the surface edge length l_s at stoppage time (bottom). All quantities are nondimensional.

noises θ_i. It is evident that θ_a scales as l_s^2. Why the difference in scaling exponents between the classical and quantum case? After all, is it not the case that both are described by the Biot–Savart integral? The answer to these questions could be found in [3, 15]. In these papers, the curvature spectra for superfluid and classical vortices were reported. In the former case, it was found that the spectra were flat (white-noise-like). However, in the latter case, a nontrivial scaling was discovered exactly in the wave-number regime corresponding to the inertial range of turbulence with Kolmogorov scaling. The authors of [3] attributed this difference to the ability of classical vortices (in opposition to superfluid line vortices) to stretch. Therefore, since the geometries in these two cases are different, there is no reason to expect the topological noise scalings (which are determined by the geometry) to be identical.

The scalings revealed in the present work are characterized by the simplicity of the computed quantities.

It is desirable that a deeper (and more technical) study of possible connections between the physics of vortex systems and the topology/geometry of their configurations be pursued in the future (e.g., [21, 22]). Such studies would illuminate the mechanisms underlying the appearance of the observed scalings. Finally, one notes that, due to computational complexity, it is difficult to make the same calculation with a wide range of counterflow velocity magnitudes. Therefore, it is not possible at present to be assertive about the universality of the reported (counterflow) scaling exponents.

ACKNOWLEDGMENTS

REFERENCES

1. D. Kivotides and A. Leonard, Phys. Rev. Lett. **90**, 234503 (2003).
2. D. Kivotides and A. Leonard, Europhys. Lett. **65**, 344 (2004).
3. D. Kivotides and A. Leonard, Europhys. Lett. **66**, 69 (2004).
4. A. Maniv, E. Polturak, and G. Koren, Phys. Rev. Lett. **91**, 197001 (2003).
5. G. E. Volovik, JETP Lett. **78**, 533 (2003).
6. G. E. Volovik, *The Universe in a Helium Droplet* (Oxford Univ. Press, New York, 2003), p. 353.
7. A. M. Polyakov, *Gauge Fields and Strings* (Harwood Academic, Chur, 1987).
8. S. C. Courts and J. T. Tough, Phys. Rev. B **38**, 74 (1988).
9. A. P. Finne, T. Araki, R. Blaauwgeers, *et al.*, Nature **424**, 1022 (2003).
10. W. F. Vinen and J. J. Niemela, J. Low Temp. Phys. **128**, 167 (2002).
11. O. C. Idowu, D. Kivotides, C. F. Barenghi, and D. C. Samuels, J. Low Temp. Phys. **120**, 269 (2000).
12. J. Koplik and H. Levine, Phys. Rev. Lett. **71**, 1375 (1993).
13. A. T. A. M. de Waele and R. G. K. M. Aarts, Phys. Rev. Lett. **72**, 482 (1994).
14. K. W. Schwarz, Phys. Rev. B **38**, 2398 (1988).
15. D. Kivotides, J. C. Vassilicos, D. C. Samuels, and C. F. Barenghi, Phys. Rev. Lett. **86**, 3080 (2001).
16. A. Leonard, Phys. Fluids **6**, 765 (1994).
17. G. S. Winckelmans and A. Leonard, J. Comput. Phys. **109**, 247 (1993).
18. A. Leonard, Annu. Rev. Fluid Mech. **17**, 523 (1985).
19. A. Leonard and K. Chua, Physica D (Amsterdam) **37**, 490 (1989).
20. D. Kivotides and A. Leonard, Europhys. Lett. **63**, 354 (2003).
21. D. R. Poole, H. Scoffield, C. F. Barenghi, and D. C. Samuels, J. Low Temp. Phys. **132**, 97 (2003).
22. C. F. Barenghi, R. L. Ricca, and D. C. Samuels, Physica D (Amsterdam) **157**, 197 (2001).

Near-Field Scanning Optical Microscopy Based on Surface-Enhanced Raman Scattering

V. S. Gorelik[1, *], O. N. Gadomsky[2, **], and A. S. Kunitsyn[2]

[1] Lebedev Institute of Physics, Russian Academy of Sciences, Moscow, 117924 Russia
*e-mail: gorelik@sci.lebedev.ru
[2] Ul'yanovsk State University, Ul'yanovsk, 432700 Russia
**e-mail: qed_group@mail.ru
Received June 29, 2004

We describe a near-field optical microscopy technique based on the interaction of a probe molecule with the sample surface (e.g., with a flat metal surface) in the field of external optical radiation and consider the spontaneous Raman scattering characterized, in the presence of a metal surface, by the effective polarizability of the probe molecule, depending on the frequency and the distance to the sample surface. At certain distances from the probe molecule to the surface, the effective polarizability of this molecule (determined with allowance for the polarizing influence of the surface of a semi-infinite medium) at the Stokes frequency sharply increases in comparison to the quantum polarizability of an isolated molecule, which is indicative of the formation of optical near-field resonances. It is shown that the proposed method of near-field optical microscopy is characterized by high sensitivity and high spatial resolution (on the order of 1 Å). © 2004 MAIK "Nauka/Interperiodica".

PACS numbers: 07.79.Fc; 78.30.-j

Surface-enhanced Raman scattering (SERS) is observed for molecules adsorbed on metals and insulators with both smooth and rough surfaces [1]. In this paper, we will consider the spontaneous SERS for a single immobile molecule occurring in the vicinity of a flat surface. As will be shown below, the SERS effect is accompanied by a shift in the energy of vibrational levels of the molecule, depending on the distance from this molecule to the surface.

According to the proposed method, a probe molecule is situated at the end of a light guide (Fig. 1) that is pumped with an optical radiation of frequency ω_L and which scatters this light. The scattered radiation at a frequency of ω_S is monitored in the wave zone in the direction within a solid angle $d\Omega$. The Fresnel reflection from a sample surface can be separated from the scattered radiation via proper selection of the angle in which the photons with the frequency ω_S are scattered.

The spatial resolution of optical near-field microscopes is determined by the size of the probe used for diagnostics of the solid surface. In connection with this, it was suggested to increase the resolution of such devices by using individual atoms as probes [2–5]. The interaction of such a probe atom with the sample surface is described on the basis of the resonance electric dipole transitions, whereby the frequency of external field approximately coincides with the resonance frequency in the spectrum of interacting atoms. In particular [4, 5], we have recently proposed a method of near-field optical microscopy with a spatial resolution on the order of 1 nm, according to which a probe atom situated at the flat end of a light guide selectively interacts with an atom in the sample due to the appearance of optical size resonances in the probe atom–sample atom system. By varying the frequency of external field so that it
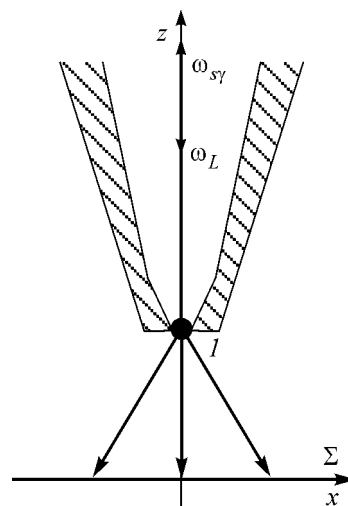

Fig. 1. Optical scheme of the near-field interaction of a probe molecule *1* with the flat surface Σ of a semi-infinite medium. The probe molecule occurs at the end of a narrow light guide (tip) providing the input of photons of an external radiation with the frequency ω_L and the output of scattered photons with the frequencies $\omega_{s\gamma} = \omega_L - \omega_{0\gamma}$, where $\omega_{0\gamma}$ are the frequencies of optical dimensional resonances.

would coincide with one of the size resonance frequencies, it is possible [4, 5] to provide a significant increase in the response dipole signal intensity in the wave zone.

In this work, we suggest a new method for diagnostics of the microscopic structure of solid surfaces, interfaces, and foreign atoms or molecules at such surfaces by means of nonresonance interaction of optical radiation with a probe molecule, which results in the Raman scattering of incident light and in the excitation of vibrational states of the probe molecule.

Let us consider the interaction of a probe molecule with the sample surface (e.g., with a flat metal surface). The corresponding boundary-value problem will be solved on the basis of a system of integro-differential equations used in the optics of insulators [6], taking into account that the main equations describing the propagation of a plane wave in a conducting medium differ from the analogous equations for a transparent insulator only in that the real optical constants are replaced by complex quantities.

The fields at the site where the probe molecule is situated ($\mathbf{r}_1$) and at the point of observation ($\mathbf{r}'$) inside or at the surface of the medium can be described as

$$\mathbf{E}_{01}(\mathbf{r}_1) = \mathbf{E}_{0I}\exp[i(\mathbf{k}_L - \mathbf{k}_S)\mathbf{r}_1] + \hat{a}_R(\mathbf{r}_1)\mathbf{X}N,$$

$$\mathbf{E}_{01}(\mathbf{r}') = \mathbf{E}_{0I}\exp[i(\mathbf{k}_L - \mathbf{k}_S)\mathbf{r}'] \quad (1)$$

$$+ \hat{a}_T(\mathbf{r}')\mathbf{X}N + \frac{1}{3}\hat{G}\mathbf{X}_1.$$

Here, $\mathbf{k}_L$ is the wavevector of the external optical radiation with the frequency ω_0, $\mathbf{k}_S$ is the wavevector of photons scattered at the Stokes frequency $\omega_S = \omega_L - \omega_0$, ω_0 is the transition frequency between the ground state and the first excited vibrational level of the probe molecule, N is the density of conduction electrons,

$$\mathbf{E}_{0I} = \mathbf{u}|\mathbf{E}_{0L}|, \quad (2)$$

$\mathbf{u}$ is the unit vector of polarization of the external optical radiation,

$$\frac{|\mathbf{E}_{0L}|^2}{4\pi} = \frac{n_0\hbar\omega_L}{V_R}, \quad (3)$$

n_0 is the number of photons of the external optical radiation, and V_R is the quantization volume. Tensor $\hat{G}$ determining the electric dipole field of the probe molecule has the following form:

$$\hat{G} = \begin{pmatrix} -F & 0 & 0 \\ 0 & -F & 0 \\ 0 & 0 & 2G \end{pmatrix}, \quad (4)$$

where

$$G = \frac{1}{R^3} - i\frac{k_0}{R^2}, \quad F = G - \frac{k_0^2}{R}, \quad (5)$$

$k_0 = \omega_L/c$, c is the speed of light in vacuum, and $R = |\mathbf{r}_1 - \mathbf{r}'|$. Vectors $\mathbf{X}$ and $\mathbf{X}'$ in Eq. (1) determine the dipole moments induced in the medium and in the probe molecule. They are defined as

$$\mathbf{X} = \alpha\mathbf{E}_0(\mathbf{r}'), \quad \mathbf{X}_1 = -w_1\alpha_1\mathbf{E}_{01}(\mathbf{r}_1), \quad (6)$$

where w_1 is the difference in probabilities of finding the probe molecule in the excited and the ground state,

$$\alpha = -\frac{e^2}{m}\frac{1}{\omega^2 + i\beta\omega}, \quad \alpha_1 = \frac{2|\mathbf{d}_0|^2}{\hbar}\frac{1}{\omega_0 - \omega + i\gamma}, \quad (7)$$

e and m are the electron charge and mass, respectively, β is the damping constant, and γ^{-1} is the phase relaxation time of the first excited level of the probe molecule. The quantity $|\mathbf{d}_0|^2$ is determined by comparing the probability of resonance quantum transition in first-order perturbation theory and the probability of Raman scattering by the quantum system [7]. This gives

$$|\mathbf{d}_0|^2 = \frac{\omega_S^2 V_R n_0}{2\pi\hbar\omega_0^3}|M_{ba}|^2, \quad (8)$$

where

$$|M_{ba}|^2 = \frac{2\pi}{V_R}\sqrt{\omega_L\omega_S}$$

$$\times e^2\sum_{p \neq b}\left[\frac{(\mathbf{u'r}_{bp})(\mathbf{ur}_{pa})}{\omega_L - \omega_{pa}} - \frac{(\mathbf{ur}_{bp})(\mathbf{u'r}_{pa})}{\omega_S + \omega_{pa}}\right] \quad (9)$$

is the scattering tensor, $\mathbf{u}'$ is the unit vector of polarization of the photons scattered at the Stokes frequency ω_S, $|a\rangle$ is the ground vibrational state of the probe molecule, $|b\rangle$ is the first excited state of this molecule, p are the intermediate states of this molecule, and $\mathbf{r}_{bp}$ and $\mathbf{r}_{ba}$ are the matrix elements corresponding to the electric dipole transitions in the long-wavelength approximation with the emission and absorption of photons. The geometric factors $\hat{a}_R$ and $\hat{a}_T$ in Eqs. (1) have the following form [8]:

$$a_T^y = -\frac{\pi}{\tilde{n}^2 - 1}\frac{\sin(\varphi + \Theta_T)}{\cos\varphi\sin\Theta_T} + \frac{2\pi\tilde{n}^2 + 2}{3}\frac{\tilde{n}^2 + 2}{\tilde{n}^2 - 1},$$

$$a_T^x = \frac{\pi}{\tilde{n}^2 - 1}\frac{\sin(\varphi + \Theta_T)}{\cos\varphi\sin\Theta_T}(\sin\varphi\cos\varphi - \cos^2\varphi)$$

$$+ \frac{2\pi\tilde{n}^2 + 2}{3}\frac{\tilde{n}^2 + 2}{\tilde{n}^2 - 1},$$

$$a_T^z = \frac{\pi}{\tilde{n}^2 - 1}\frac{\sin(\varphi + \Theta_T)}{\cos\varphi\sin\Theta_T}(\sin\varphi\cos\varphi - \sin^2\varphi)$$

$$+ \frac{2\pi\tilde{n}^2 + 2}{3}\frac{\tilde{n}^2 + 2}{\tilde{n}^2 - 1}, \quad (10)$$

$$a_R^y = -\frac{\pi}{\tilde{n}^2 - 1}\frac{\sin(\varphi - \Theta_T)}{\cos\varphi\sin\Theta_T},$$

$$a_R^x = \frac{\pi}{\tilde{n}^2 - 1}\frac{\sin(\varphi - \Theta_T)}{\cos\varphi\sin\Theta_T}(\sin\Theta_R\cos\Theta_R - \cos^2\Theta_R),$$

$$a_R^z = \frac{\pi}{\tilde{n}^2 - 1}\frac{\sin(\varphi - \Theta_T)}{\cos\varphi\sin\Theta_T}(\sin\Theta_R\cos\Theta_R - \sin^2\Theta_R),$$

where $\tilde{n}$ is the complex refractive index of the medium; Θ_T and Θ_R are the angles of light refraction and reflection from the sample surface Σ, respectively (Fig. 1). For the Fresnel reflection and refraction of a wave incident at the angle Θ_I onto the surface Σ, these angles are related as

$$\varphi = \Theta_I, \quad \tilde{n}\sin\Theta_T = \sin\Theta_I, \quad \Theta_R = \pi - \Theta_I. \quad (11)$$

Substituting expressions (6) into Eq. (1); taking into account that, for the points of observation in the near-field zone with respect to the surface Σ one has

$$|\mathbf{k}_L - \mathbf{k}_L|R \ll 1, \quad F = G = \frac{1}{R^3}; \quad (12)$$

and solving the system of equations (1), we can determine the fields at the site where the probe molecule is situated ($\mathbf{E}_{01}$) and on the sample surface ($\mathbf{E}_0$). Let us introduce the effective polarizabilities

$$\mathbf{X}_1 = \hat{\alpha}_{\text{eff}}(1)\mathbf{E}_{0I}, \quad \mathbf{X} = \hat{\alpha}_{\text{eff}}\mathbf{E}_{0I} \quad (13)$$

and determine these values by substituting expressions for the fields $\mathbf{E}_{01}$ and $\mathbf{E}_0$. For the x components of the effective polarizability vectors, we obtain

$$\alpha_{\text{eff}}^x(1) = -w_1\alpha_1\frac{1 - a_T^xN\alpha + a_R^zN\alpha}{1 - a_T^xN\alpha - \frac{1}{2}Fw_1\alpha_1 a_R^xN\alpha},$$

$$\alpha_{\text{eff}}^x = \alpha\frac{1 + \frac{1}{2}Fw_1\alpha_1}{1 - a_T^xN\alpha - \frac{1}{2}Fw_1\alpha_1 a_R^xN\alpha}. \quad (14)$$

Taking into account the form of diagonal tensors (10) and (4), we also obtain the effective polarizabilities of the other components of induced dipole moments.

Effective polarizabilities (14) determine the near-field self-consistent interaction of the probe molecule with the metal surface. A dispersion dependence of the polarizability α_{eff}^x of the probe molecule strongly differs from the analogous dependence of the polarizability α_1 of the same isolated molecule. The frequencies at which the quantities $\hat{\alpha}_{\text{eff}}^x$ reach maximum values differ from the frequency ω_0 corresponding to the transition frequency from the lowest vibrational state to the first excited state for the same ground-state electronic con-

figuration of the molecule. These frequencies correspond to the optical near-field dimensional resonances and depend on the distance from the probe molecule to the flat metal surface. The effective polarizabilities $\hat{\alpha}_{\text{eff}}^x$ of the probe molecule also depend on the population of the vibrational states under consideration, which is determined by w_1. Interaction of the probe molecule with the metal surface renders the molecule anisotropic because, in the general case, $\alpha_{\text{eff}}^x(1) \neq \alpha_{\text{eff}}^y(1) \neq \alpha_{\text{eff}}^z(1)$. In the case of a light normally incident onto the metal surface, expressions (10) yield $\alpha_{\text{eff}}^x(1) = \alpha_{\text{eff}}^y(1) \neq \alpha_{\text{eff}}^z(1)$.

Using expressions for the effective polarizability (14), we calculate the SERS coefficient as

$$q_\gamma = \frac{dP_S^\gamma/d\Omega}{dP_S/d\Omega}, \quad (15)$$

where

$$dP_S/d\Omega = \frac{2\pi}{\hbar^2}|M_{ba}|^2\frac{\omega_S^2 n_0 V_R}{(2\pi c)^3}, \quad (16)$$

is the Stokes power radiated per unit solid angle $d\Omega$ by an isolated molecule;

$$dP_S^\gamma/d\Omega = \frac{1}{16\pi c^3\hbar}\omega_{0\gamma}^3|\alpha_{\text{eff}}^\gamma(1)|^2(E_{0I}^\gamma)^2, \quad (17)$$

is the Stokes power radiated per unit solid angle $d\Omega$ by a probe molecule situated near the metal surface; $\gamma = x$, y, z; and $\omega_{0\gamma}$ is the frequency of one of the optical near-field resonances. The Stokes radiation from a molecule near a surface takes place at the frequency $\omega_{s\gamma} = \omega_L - \omega_{0\gamma}$, while the isolated molecule radiates at $\omega_S = \omega_L - \omega_0$. Substituting expressions (16) and (17) into Eq. (15), we can determine the condition for which the SERS coefficient is maximum. This condition has the form

$$\text{Re}(1 - a_T^\gamma N\alpha + G_{\gamma\gamma}w_1\alpha_1 a_R^\gamma N\alpha) = 0. \quad (18)$$

Using this relation at a fixed distance between the probe molecule and the sample surface, we can determine the frequency of molecular vibrations and oscillations of conduction electrons, for which the signal of dipole radiation in the wave zone is maximum.

Let us consider a numerical example in which a pyridine molecule situated at the tip end interacts with a flat silver surface. Let the molecule pass from the ground state to a vibrationally excited state in the ground electron state corresponding to a line at 1010 cm^{-1} [1]. For the external optical radiation with a wavelength of $\lambda = 0.6328$ μm (He–Ne laser), we obtain $\omega_L = 2.98 \times 10^{15}$ s^{-1} and the Stokes photon frequency $\omega_S = 2.787 \times 10^{15}$ s^{-1}. For the diameter of a hole at the tip end equal to 80 Å and a laser power of 100 mW, the number of scattered photons at a frequency of ω_L is $n_0 = 4.63 \times 10^{19}$. In this case, formula (16) yields
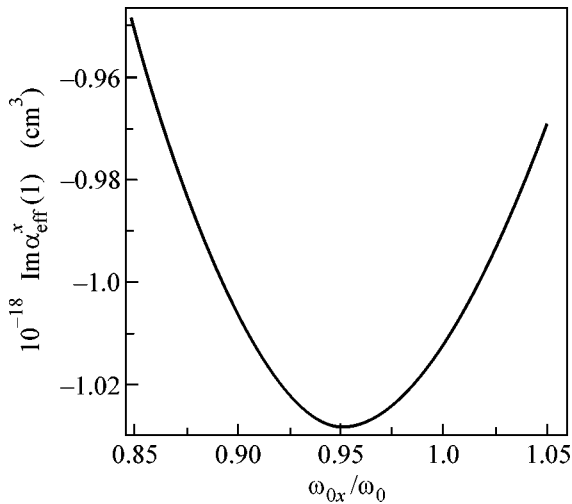
Fig. 2. Plot of the effective polarizability of a probe molecule occurring at a fixed distance $R = 5$ Å from a flat silver surface, as calculated for $\omega_0 = 1.9 \times 10^{14}$ s^{-1}, $d_0 = 2 \times 10^{-16}$ esu, $\beta = 4.17 \times 10^{15}$ s^{-1}, $N = 2.34 \times 10^{22}$ cm^{-3}, and $\sigma = 2.24 \times 10^{17}$ s^{-1}. The angle of photon incidence on the metal surface is $\Theta_I = 0$.

$dP_S/d\Omega = 7.04 \times 10^3$ s^{-1} sr^{-1} (for $V_R = 1$ cm^3). Using this value, we can determine the effective dipole moment d_0 of transition by the formula

$$d_0^2 = \frac{2\pi c^3 \hbar}{\omega_0^3} \frac{dP_S}{d\Omega}, \qquad (19)$$

which yields $d_0 = 7.496 \times 10^{-18}$ esu. Once the d_0 value is known, we find the polarizability of the probe molecule in the vicinity of the isolated resonance ω_0 using formula (7) and setting $\gamma = 2\pi \times 10^{12}$ s^{-1}. For silver with the density of conduction electrons $N = 2.34 \times 10^{22}$ cm^3 and conductivity $\sigma = 2.24 \times 10^{17}$ s^{-1}, the square of the plasma frequency is $\omega_p^2 = 0.745 \times 10^{32}$ s^{-1} and the damping constant is $\beta = 4\pi\omega_p^2/\sigma = 4.17 \times 10^{15}$ s^{-1}. For these parameters and normal incidence of light onto the sample surface, we have $\tilde{n}^2 \approx i \times 4\pi\sigma/\omega$, $a_T^\gamma \approx 2\pi/3$, $a_R^x = a_R^y \approx \pi\omega/i \times 4\pi\sigma$, and $a_R^z = 0$. Substituting these values into Eq. (18), we determine the value of the optical near-field resonance frequency ω_{0x} at which the effective polarizability $a_{\text{eff}}^x(1)$ in Eq. (14) exhibits maximum.

The effective dipole moment (19) of transition is proportional to the number of scattered photons n_0

interacting with a single molecule situated at the end of a light guide. The n value depends on the beam cross-sectional area. By decreasing this area to a value equal to the molecular cross section, we may change the d_0 value and vary, according to Eq. (18), the distance R from the probe molecule to the sample surface.

Figure 2 shows the dispersion dependence of the effective polarizability $a_{\text{eff}}^x(1)$ at a fixed distance $R = 5$ Å from the probe molecule to the sample surface. For $d_0 = 2 \times 10^{-16}$ esu and $\omega_0 = 1.9 \times 10^{14}$ s^{-1}, we obtain the following value of the optical near-field resonance frequency: $\omega_{0x} = 1.811 \times 10^{14}$ s^{-1}. At the frequency of the near-field resonance, the SERS coefficient is $q_x = 5.4 \times 10^3$ for $w_1 = -1$.

In conclusion, we have described the operation of a optical near-field microscope based on enhanced Raman scattering by a probe molecule as a result of interaction with a sample (e.g., with a flat metal surface). The spatial resolution of such a near-field microscope is determined by the distance from the probe molecule to the sample surface, while the sensitivity at the Stokes frequency $\omega_L - \omega_{0x}$ is determined by the SERS coefficient (15). Based on the proposed principle of the optical near-field microscope and taking into account the experimental conditions and the character of samples, it is possible to change the geometry of the tip with a probe molecule at its end and modify geometric factors (10), for example, allowing for the sample surface roughness. These physical situations will be considered in subsequent publications.

REFERENCES

1. *Surface Enhanced Raman Scattering*, Ed. by R. K. Chang and T. E. Furtak (Plenum, New York, 1982).
2. S. K. Sekatskiĭ and V. S. Letokhov, Pis'ma Zh. Éksp. Teor. Fiz. **63**, 311 (1996) [JETP Lett. **63**, 319 (1996)].
3. J. Michaels, C. Hettich, J. Mynek, and V. Sandoghdar, Nature **405**, 325 (2000).
4. O. N. Gadomskiĭ and K. Yu. Moiseev, Zh. Prikl. Spektrosk. **68**, 526 (2001).
5. O. N. Gadomskiĭ and K. Yu. Moiseev, Opt. Spektrosk. **93**, 163 (2002) [Opt. Spectrosc. **93**, 153 (2002)].
6. O. N. Gadomskiĭ, Usp. Fiz. Nauk **170**, 1145 (2000) [Phys. Usp. **43**, 1071 (2000)].
7. A. S. Davydov, *Quantum Mechanics* (Nauka, Moscow, 1963; Pergamon, Oxford, 1976).
8. O. N. Gadomskiĭ and A. S. Kadochkin, Zh. Éksp. Teor. Fiz. **124**, 516 (2003) [JETP **97**, 466 (2003)].

Translated by P. Pozdeev

Microwave Spectroscopy of Cold Rubidium Atoms

V. M. Entin and I. I. Ryabtsev

Institute of Semiconductor Physics, Siberian Division, Russian Academy of Sciences, Novosibirsk, 630090 Russia
Received June 22, 2004

The effect of microwave radiation on the resonance fluorescence of a cloud of cold ^{85}Rb atoms in a magnetooptical trap is studied. The radiation frequency was tuned near the hyperfine splitting frequency of rubidium atoms in the 5S ground state. The microwave field induced magnetic dipole transitions between the magnetic sublevels of the 5S ($F = 2$) and 5S ($F = 3$) states, resulting in a change in the fluorescence signal. The resonance fluorescence spectra were recorded by tuning the microwave radiation frequency. The observed spectra were found to be substantially dependent on the transition under study and the frequency of a repump laser used in the cooling scheme. © 2004 MAIK "Nauka/Interperiodica".

PACS numbers: 32.50.+d; 32.30.Bv

The method of optical-radio-frequency double resonance provides the basis for atomic frequency standards [1]. Microwave radiation, resonant with transitions between the hyperfine levels of alkali metal atoms (for example, Rb and Cs), induces magnetic dipole transitions, resulting in turn in a change in a resonance fluorescence or absorption signal at optical transitions from the ground state. In the first experiments, the effect of microwave fields on absorption and polarization of light from resonance lamps has been studied [2].

Before the advent of magnetooptical traps for laser cooling and capture of atoms [3], thermal atomic gases with a large Doppler broadening have been mainly studied. The first microwave spectroscopic experiments with cooled atoms have been performed in a magnetic trap with Na atoms [4]. The fluorescence spectrum of Na atoms captured in a strong magnetic field (~2300 G) was studied in the presence of a probe laser field and probing microwave radiation. However, a strong magnetic field caused the broadening of resonances up to 200 MHz, which substantially exceeds the natural width of optical transitions.

Later [5], a microwave field was used to excite transitions between the hyperfine levels of the ground state of cesium atoms cooled in the optical molasses at the point of intersection of three standing light waves. The fluorescence signal from atoms, which have been preliminary cooled in the molasses, was studied after the shutdown of cooling laser beams. This allowed the observation of optically unperturbed microwave resonances of width as small as a few tens of hertz. The intensity of microwave radiation in these experiments did not exceed a few tens of nW/cm^2.

These studies have been further developed in experiments with so-called "atomic fountains" (see, for example, [6]). Narrowing of the atomic-standard lines was achieved by the Ramsey fringes method during the round-trip transit of cooled slow atoms in a microwave resonator [7]. In addition, a microwave field was used in some papers instead of a repump laser to produce an optical-microwave magnetooptical trap [8].

The aim of the microwave spectroscopy of cooled atoms is, as a rule, the observation of ultranarrow resonances and the development of a precision atomic clock based on microwave transitions. However, microwave spectroscopy can be also used to study processes occurring in a cloud of cold atoms. For example, recently microwave spectroscopic experiments were performed with atoms loaded from a magnetooptical trap to an optical trap with a large frequency detuning [9]. The authors of paper [9] also observed narrow microwave resonances (~500 Hz and narrower) by switching off coiling lasers during measurements.

The aim of this work was to study the effect of a microwave field on a resonance fluorescence signal in a standard magnetooptical trap with Rb atoms and to estimate the possibility of using this effect for diagnostics of a cloud of cold atoms.

EXPERIMENTAL SETUP

The Rb atoms were cooled and captured in a magnetooptical trap using a laser setup containing two 780-nm external-resonator semiconductor lasers and a frequency-locking system based on saturated absorption in optical cells with Rb atoms [10, 11].

Laser cooling was performed using a standard optical scheme consisting of three pairs of orthogonally polarized laser beams (σ^+, σ^-) crossing at the center of a quartz cell (Fig. 1), which was evacuated by ion pumps down to a pressure of ~10^{-8} Torr. The source of Rb atoms was an ampoule containing a natural mixture of rubidium isotopes at room temperature.

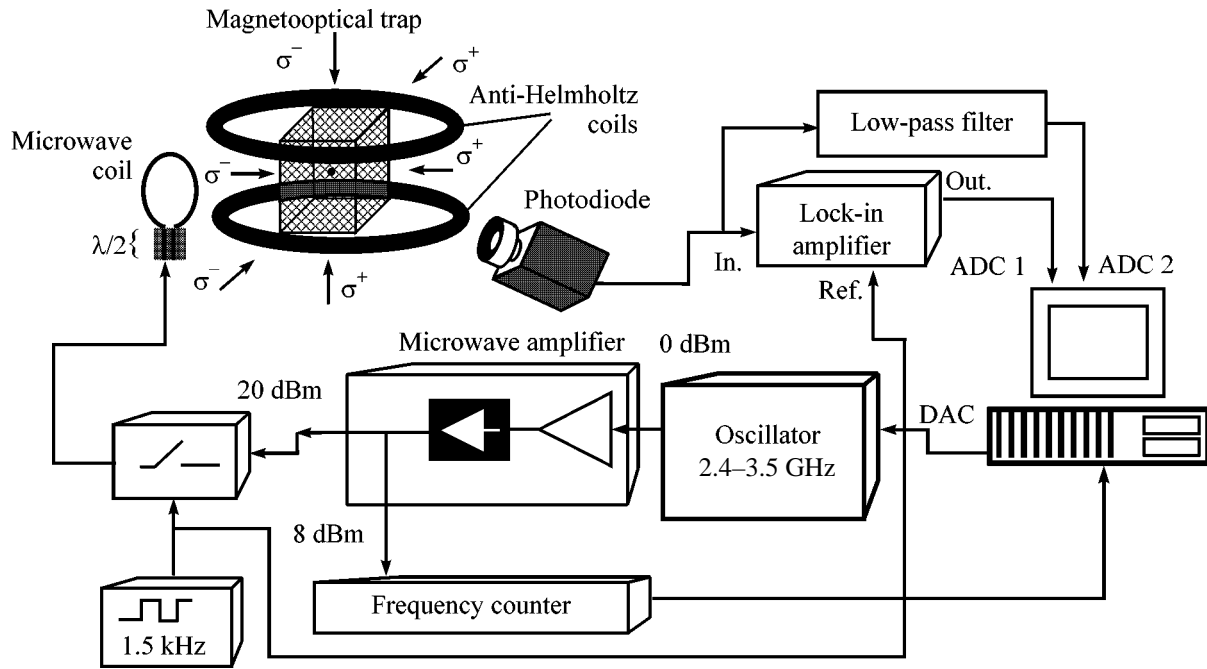The magnetic-field gradient in the trap (0–15 G/cm) was produced by a pair of anti-Helmholtz coils. Resid-

Fig. 1. Scheme of the experimental setup.

ual magnetic fields were compensated with the help of additional Helmholtz coils. The possibility of compensation for residual magnetic fields and the accuracy of alignment of the laser beams were provided by using two CCD cameras placed from both sides of the cell.

The resonance fluorescence signal was detected with a calibrated two-element photodiode equipped by a TV objective and a differential amplifier. The cloud image was projected by the objective on one of the elements of the photodiode, the second element being used to subtract laser radiation scattered from the cell walls.

The Rb atoms were captured in the trap by locking the cooling laser frequency either to the slope of the saturated absorption (Fig. 2b) $5S_{1/2}(F = 3) \longrightarrow 5P_{3/2}(F = 4)$ transition peak of ^{85}Rb with the red 1–3-Γ detuning from the resonance center (Fig. 2a) ($\Gamma = 6$ MHz is the natural width of the D_2 line of Rb) or to the slope of the fluorescence resonance of the trap. In the latter case, the so-called self-stabilized magnetooptical trap was realized [12]. As a result, the fluorescence signal had a more stable constant component corresponding to the equilibrium population of the trap.

The repump laser was tuned to the slope of the saturated absorption $5S_{1/2}(F = 2) \longrightarrow 5P_{3/2}(F = 2$ or 3) transition peak with the red 0–3-Γ detuning (Fig. 2a) and was locked to the resonance using the Pound–Drever frequency-modulation method [13, 14].

The output power of lasers was ~6 mW. Laser beams were expanded in front of the cell with the help of telescopes up to a diameter of 7–8 mm. The intensity of each of the laser beams incident on the cell was 2.6 mW/cm^2, while the calculated saturation intensity was 1.65 mW/cm^2. Figure 2c illustrates the measured dependence of the number of trapped atoms on the cooling laser frequency, the repump laser frequency being locked to the resonance at the $5S_{1/2}(F = 2) \longrightarrow 5P_{3/2}(F = 2)$ transition. Figure 2d shows the dependence of the number of trapped atoms on the total power of the repump laser in the trap when the cooling laser was detuned by $\delta = 9$ MHz. It is seen that the saturation of trap population occurs even at 0.1 mW.

We obtained in the trap a cloud of cold atoms 0.6–2 mm in diameter, containing $\leq 2 \times 10^7$ atoms, which corresponds to an atomic density $\leq 2 \times 10^{10}$ cm^{-3}. The cloud temperature equal to ~50 μK was measured by the dynamics of a decrease in the number of atoms after a short (5–200 ms) switching off of the magnetic field gradient. The trap population decreased by a factor of e for the time $t \sim 30$ ms. This means that a greater part of Rb atoms escaped from the region of interaction with laser radiation for the time 30 ms by flying the distance $L = A/2 \approx 3.5$ mm (A is the beam aperture). In the Maxwell velocity distribution approximation, the expression for the average temperature of atoms can be written in the form [4]

$$\langle T \rangle = \frac{M \langle v \rangle^2}{3 k_B},\qquad(1)$$

where $\langle v \rangle = L/t$ is the average velocity of atoms, k_B is the Boltzmann constant, and M is the atom mass; and the temperature estimated from (1) is 50 μK.
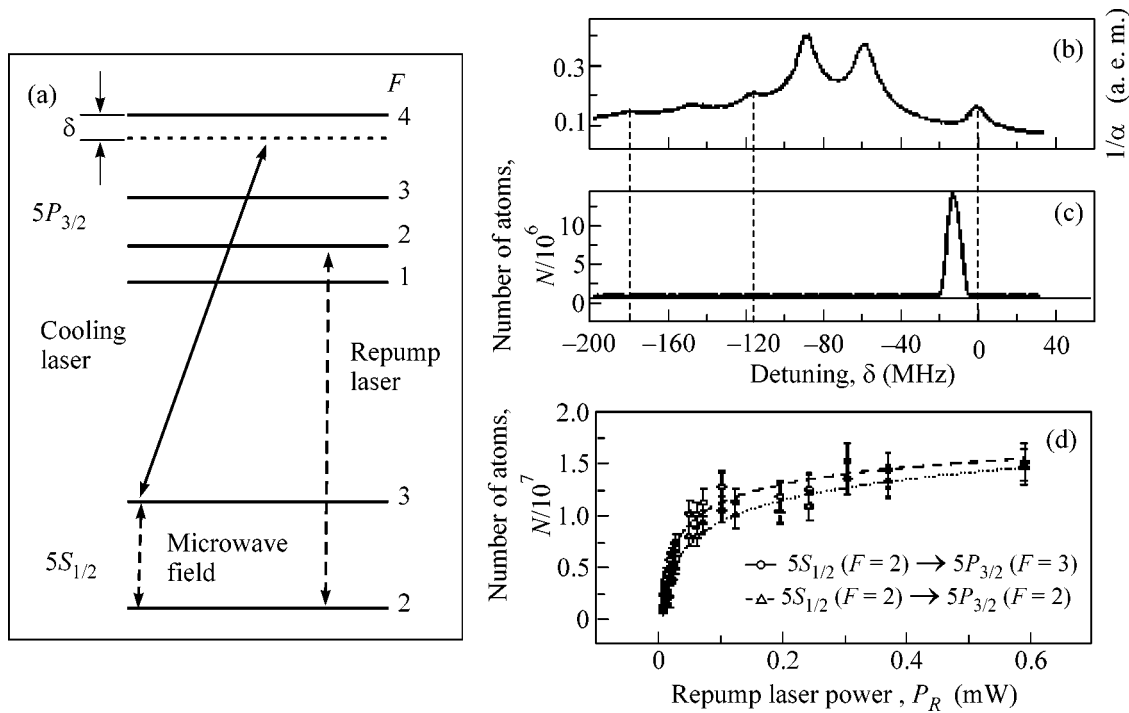
Fig. 2. (a) Scheme of transitions in ^{85}Rb atoms; (b) saturated absorption spectrum of a reference cell; (c) the number of atoms in the trap as a function of the cooling laser frequency; (d) dependence of the number of atoms in the trap on the total output power of the repump laser.

In microwave spectroscopic experiments, we used a frequency synthesizer based on the first heterodyne of a S4-60 spectrum analyzer with a 20-dBm, 3-GHz (±300 MHz) power amplifier (Fig. 1). The width of the heterodyne line did not exceed 10 kHz. The frequency was continuously tuned with the help of a CAMAC digital-to-analog converter.

A weak change in the resonance fluorescence caused by magnetic dipole transitions in rubidium atoms was investigated by the lock-in detection technique. For this purpose, the amplitude of microwave radiation was modulated by a SSW-508 microwave switch (Sirenza). The output microwave radiation was fed from the switch to a wire coil of diameter 4 cm, which was matched with the help of a strip half-wave transformer and was located at a distance of 3 cm from the trap center. Control pulses at the frequency 1.5 kHz from a pulse generator were applied to the microwave switch.

The fluorescence signal from the photodetector was fed to a phase-sensitive amplifier. The output signal of the generator controlling the switch was used as the reference frequency signal. As a result, the output signal of the amplifier was proportional to a change in the fluorescence intensity caused by microwave radiation. This signal, along with a constant fluorescence from the trap, was recorded as a function of the microwave generator frequency.

We have failed in our first experiments to achieve the reproducibility of microwave spectra when the cooling laser frequency was locked to the saturated absorption resonances. For this reason, we used frequency locking over fluorescence. Microwave radiation modulated the fluorescence signal at 1.5 kHz. The cutoff frequency of the cooling laser locking system was selected to be on the order of few hundred of hertz to avoid the suppression of the useful signal.

To enhance the useful signal, the repump laser power was reduced to 90 μW for each of the beams in the trap. In addition, to narrow the microwave resonances in microwave experiments, we used the minimal gradient of the magnetic field in the trap (≈5G/cm) at which a sufficient number of atoms is still captured by the trap.

EXPERIMENTAL RESULTS AND DISCUSSION

Figure 3a shows the dependence of the trap population on the microwave frequency for the case when the repump laser was detuned to the red with respect to the maximum of the $5S_{1/2}(F = 2) \longrightarrow 5P_{3/2}(F = 2)$ transition. The microwave spectrum was obtained after averaging over ten measurements. Noise and fluctuations were mainly caused by the photodetector noise. The position of the frequency 3035.732 MHz of the unperturbed microwave resonance for the magnetic dipole $5S_{1/2}(F = 2) \longleftrightarrow 5S_{1/2}(F = 3)$ transition in ^{85}Rb atoms
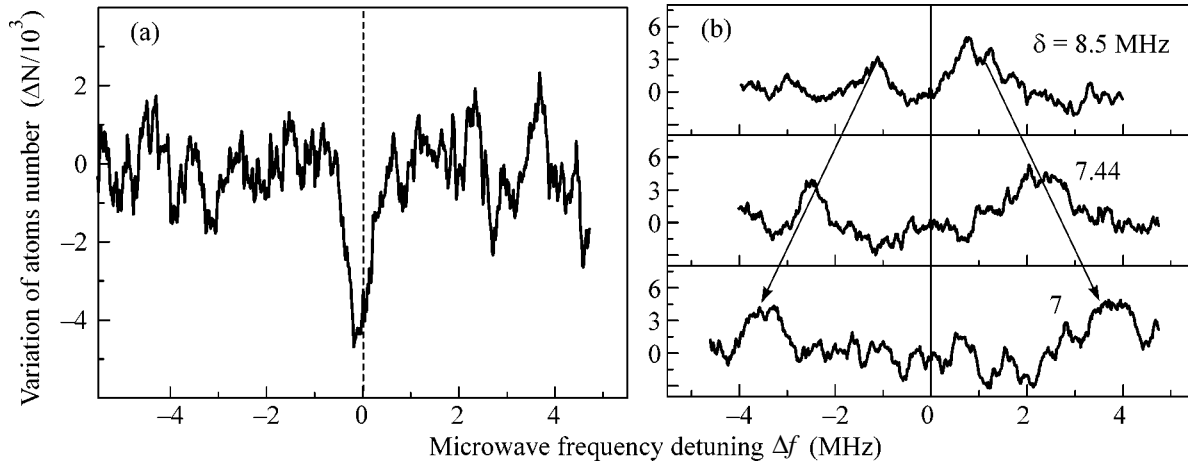
Fig. 3. Dependence of the trap population on the microwave-field frequency for the repump laser tuned to the (a) $5S_{1/2}(F = 2) \longrightarrow 5P_{3/2}(F = 2)$ and (b) $5S_{1/2}(F = 2) \longrightarrow 5P_{3/2}(F = 3)$ transitions.

is indicated by the dashed straight line. One can see that the fluorescence signal from the trap exhibits a dip near this frequency. The width of the microwave resonance was almost the same in different experiments and was ~500 kHz.

The observed resonance is caused by the transfer of cold ^{85}Rb atoms from the $5S_{1/2}(F = 3)$ state to the $5S_{1/2}(F = 2)$ state due to magnetic dipole transitions. In the case of exact tuning of the microwave frequency, the fluorescence intensity of the trap at the cooling $5S_{1/2}(F = 3) \longrightarrow 5P_{3/2}(F = 4)$ transition decreases because the number of atoms in the $5S_{1/2}(F = 3)$ state decreases. The absence of the shift of the microwave resonance suggests that either the fluorescence signal is detected from the central part of a cloud of cooled atoms, where the magnetic field is weak and the Zeeman shift of levels is negligible, or magnetic dipole transitions are excited between the central Zeeman components $5S_{1/2}(F = 2, |m_F| = 0)$ and $5S_{1/2}(F = 3, |m_F| = 0)$, which are not shifted. The latter assumption is unlikely because the magnetic moments of cold atoms have no definite orientation with respect to any arbitrary quantization axis in the trap, while the polarization of microwave radiation has not been especially selected. Therefore, the most probable reason for the absence of the shift of the microwave resonance is the detection of variations in the fluorescence intensity from the central part of the cloud. Such a behavior is observed only when the repump laser is tuned to the $5S_{1/2}(F = 2) \longrightarrow 5P_{3/2}(F = 2)$ transition, at which a part of atoms at the trap center can be transferred to the dark states, which do not interact with laser radiation [15].

The decrease in the fluorescence intensity is most likely explained by the fact that microwave radiation transfers a part of atoms from the $5S_{1/2}(F = 3)$ state to the local dark states, which are produced at the $5S_{1/2}(F = 2)$ level by the repump laser. Because atoms

in these states are not excited by the pump laser, they do not also interact with the radiation of the cooling laser, which results in the reduction of the fluorescence signal.

By analyzing the width of the observed resonance, note that the $5S_{1/2}(F = 3)$ sublevel should experience the shift, broadening, and splitting under the action of radiation from the cooling laser due to the Autler–Townes effect [16]. The level splitting and shift are determined by the position of the quasi-energy levels [17]

$$\omega_\pm = \delta/2 \pm \sqrt{\delta^2/4 + \Omega^2/4}, \qquad (2)$$

where δ is the detuning from the optical resonance and Ω is the Rabi frequency. Note that the detuning and Rabi frequency in our experiment (in the case of saturation) are of the same order of magnitude as Γ. The magnetic-field gradient determines the variation of detunings on the cloud dimensions, therefore a microwave resonance should broaden up to a few megahertz. This conclusion is confirmed by recent papers [18, 19] in which the Autler–Townes effect was studied on optical transitions in cold Rb atoms and level shifts and splittings were observed.

However, the resonance width ≈ 400 kHz observed in our experiments is noticeably smaller than the above value and is virtually independent of the detuning of the cooling laser. This is probably explained by the fact that microwave radiation has induced transitions to the dark states, which do not interact with radiation. In this case, the resonance width was determined only by the inhomogeneity of the magnetic field at the trap center, where the dark states for degenerate levels can appear. This conclusion requires further experiments to study the features of the dark states produced at the trap center when the repump laser operates at the $5S_{1/2}(F = 2) \longrightarrow 5P_{3/2}(F = 2)$ transition.

The resonance amplitude in Fig. 3a in different experiments was $(3–9) \times 10^3$ atoms. Its maximum value was determined by the strength of the magnetic component of the microwave field. At the same time, it was found that a rather large variation in the amplitude was caused by weak fluctuations in the detunings of laser frequencies from optical-transition frequencies. The maximum amplitude was achieved when these detunings were identical, the central frequency of the resonance being invariable.

Quite a different picture was observed when the repump laser was tuned to the $5S_{1/2}(F = 2) \longrightarrow 5P_{3/2}(F = 3)$ transition, for which the dark states are absent (Fig. 3b). The spectrum exhibits two peaks ($\mp \Delta f$), which are symmetrically split with respect to the center of the $5S_{1/2}(F = 2) \longleftrightarrow 5S_{1/2}(F = 3)$ transition. It was assumed first that these peaks appear due to the Autler–Townes effect for the $5S_{1/2}(F = 3)$ level in the field of the cooling laser because the sifts of resonances depended on the detuning of the cooling laser at the $5S_{1/2}(F = 3) \longrightarrow 5P_{3/2}(F = 4)$ transition. However, one can see from Eq. (2) that the shifts of the quasi-energy levels should be different in the case of the red detuning of the laser. Therefore, the shifts of the resonances in Fig. 3b should be also different, whereas we observe the symmetric shifts and splitting.

The observed effect can be also interpreted in a different way. Because the frequencies of microwave resonances are shifted with respect to the central frequency, they are mainly caused by atoms located in the gradient magnetic field at the periphery of a cold cloud. As the red detuning of the cooling laser from the resonance with the $5S_{1/2}(F = 3) \longrightarrow 5P_{3/2}(F = 4)$ transition decreases, the temperature of atoms increases, resulting in an increase in the cloud size. Therefore, the shifts of microwave resonances increase due to the increase in the Zeeman splitting at the cloud periphery. The increase in the fluorescence signal in the region of resonances in Fig. 3b compared to its decrease in Fig. 3a is caused by the increase in the efficiency of the repump laser at the cloud periphery when microwave radiation is tuned to the resonance. The presence of two resonances in Fig. 3b suggests that magnetic dipole transitions are excited between the extreme Zeeman components of the $5S_{1/2}(F = 2, |m_F| = \pm2)$ and $5S_{1/2}(F = 3, |m_F| = \pm3)$ levels having the largest resonance shifts ($d\nu_{Zeeman}/dB \approx 2.56$ MHz/G). The frequency shifts shown in Fig. 4 correspond to the trap radius from 1 to 1.8 mm, in accordance with analysis of the TV image of the trap.

Although the main features of the spectra presented above were reproducible in different experiments, note that the signal noise and fluctuations were rather large. The signal-to-noise ratio was not substantially improved even in the case of lock-in detection. This is related to a rather long loading time of the trap (~1 s), resulting in the suppression of the alternate component
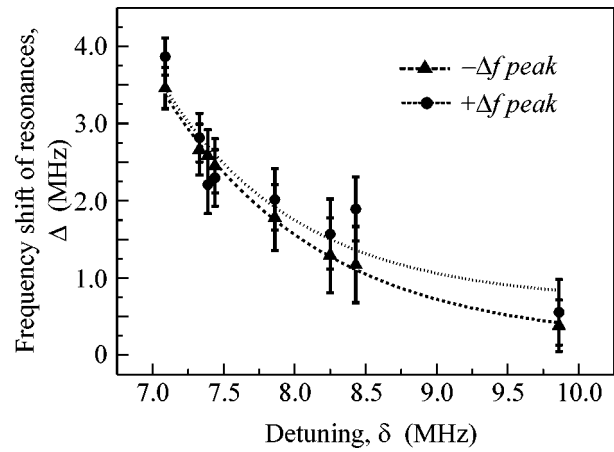

Fig. 4. Frequency shift of resonances in Fig. 3b as a function of the detuning δ of the cooling laser. The dashed curves are the approximations by the method of least squares.

of the fluorescence signal. For this reason, the amplitude of resonances in our experiments did not exceed 0.01 of the total fluorescence intensity level.

At the same time, our experiments showed that the microwave spectroscopy of cold atoms allows one to study fluorescence signals from different regions of a cloud of cold atoms. The switching to the detection of one or another region of the cloud is achieved by a proper choice of one of the transitions for the repump laser. For example, when the $J \longrightarrow J$ transition is used, a change in fluorescence from the central part of the cloud is detected, while in the case of the $J \longrightarrow J + 1$ transitions, fluorescence from the cloud periphery is analyzed. This is directly related to the presence of the "dark states" for the $J \longrightarrow J$ transitions and their absence for the $J \longrightarrow J + 1$ transitions, as was already mentioned in [15]. These features can be used for the development of new methods for diagnostics of cold atoms.

REFERENCES

1. J. Vanier and C. Audoin, *The Quantum Physics of Atomic Frequency Standards*, Ed. by A. Hilger (IOP Press, Bristol, 1989), Vols. 1–2.

2. H. Kopferman, *Kernmomente* (Akademie, Frankfurt, 1956; Inostrannaya Literatura, Moscow, 1960).

3. H. J. Metcalf, P. Van Der Straten, and H. E. Stanley, *Laser Cooling and Trapping* (Springer, New York, 1999).

4. A. G. Martin, K. Helmerson, V. S. Bagnato, *et al.*, Phys. Rev. Lett. **61**, 2431 (1988).

5. D. W. Sesko and C. E. Wieman, Opt. Lett. **14**, 269 (1989).

6. E. A. Donley, T. P. Crowley, T. P. Heavner, *et al.*, in *Proceedings of 2003 Joint Meeting of IEEE International Frequency Control Symposium and EFTF Conference* (2003), p. 135.

7. N. F. Ramsey, *Molecular Beams* (Clarendon Press, Oxford, 1956; Inostrannaya Literatura, Moscow, 1960).

8. R. J. C. Spreeuw, C. Gerz, L. S. Goldner, *et al.*, Phys. Rev. Lett. **72**, 3162 (1994).

9. A. Kaplan, M. F. Andersen, and N. Davidson, Phys. Rev. A **66**, 045401 (2002).

10. V. M. Éntin, A. E. Boguslavskiĭ, I. I. Ryabtsev, *et al.*, Pis'ma Zh. Éksp. Teor. Fiz. **71**, 257 (2000) [JETP Lett. **71**, 175 (2000)].

11. V. M. Entin, I. I. Ryabtsev, A. E. Boguslavsky, *et al.*, Opt. Commun. **207**, 201 (2002).

12. C. S. Fletcher, J. E. Lye, N. P. Robins, *et al.*, Opt. Commun. **212**, 85 (2002).

13. R. W. P. Drever, J. L. Hall, F. V. Kovalski, *et al.*, Appl. Phys. B **31**, 97 (1983).

14. G. C. Bjorklund, M. D. Levinson, W. Lenth, *et al.*, Appl. Phys. B **32**, 145 (1983).

15. A. M. Tumaĭkin and V. I. Yudin, Zh. Éksp. Teor. Fiz. **98**, 81 (1990) [Sov. Phys. JETP **71**, 43 (1990)].

16. S. H. Autler and C. H. Townes, Phys. Rev. **100**, 703 (1955).

17. V. M. Akulin and N. V. Karlov, *Intense Resonant Interactions in Quantum Electronics* (Nauka, Moscow, 1987) [in Russian].

18. B. K. Teo, D. Feldbaum, T. Cubel, *et al.*, Phys. Rev. A **68**, 053407 (2003).

19. S. R. Muniz, K. M. F. Magalhães, E. A. L. Henn, *et al.*, Opt. Commun. **235**, 333 (2004).

Translated by M. Sapozhnikov

Third-Harmonic and Sum-Frequency Generation in a Quadratically Nonlinear Polymer by Time-Ordered Ultrashort Laser Pulses

S. O. Konorov[1], A. A. Ivanov[2], D. A. Akimov[1], A. V. Yakimanskii[3], M. V. Alfimov[2], and A. M. Zheltikov[1, 4, *]

[1] *Physics Department, Moscow State University, Vorob'evy gory, Moscow, 119899 Russia*
* *e-mail: zheltikov@top.phys.msu.su*
[2] *Center of Photochemistry, Russian Academy of Sciences, ul. Novatorov 7a, Moscow, 117421 Russia*
[3] *Institute of Supramolecular Compounds, Russian Academy of Sciences, St. Petersburg, 199004 Russia*
[4] *International Laser Center, Moscow State University, Vorob'evy gory, Moscow, 119899 Russia*
Received June 23, 2004

Third-harmonic and sum-frequency generation in quadratically nonlinear azopolymer films is experimentally studied using femtosecond chromium forsterite laser pulses. A noncollinear geometry of sum-frequency and third-harmonic generation developed and implemented in this work allows the influence of the time ordering of ultrashort laser pump pulses on nonlinear-optical phenomena to be experimentally observed. Femtosecond laser pulses induce transitions of azopolymer molecules to an electronically excited state and produce vibrational wave packets, leading to an asymmetry in the dependence of the efficiency of second- and third-order nonlinear-optical processes on the delay time between the pump pulses. © 2004 MAIK "Nauka/Interperiodica".

PACS numbers: 42.65.–k

Optical harmonic generation is one of the key phenomena in nonlinear optics. Second-harmonic generation was observed for the first time in 1961 by Franken [1], who studied propagation of ruby-laser radiation through crystalline quartz. Subsequent experiments have revealed the potential of optical harmonic generation in nonlinear crystals for highly efficient frequency conversion of laser radiation [2, 3]. The advent of laser systems capable of generating ultrahigh-intensity light fields has resulted in the discovery of high-order harmonic generation [4, 5]. Unprecedentedly broad spectra of optical harmonics, stretching down to the wavelengths of only a few nanometers have been observed in experiments performed in the mid-1990s [6]. Generation of attosecond pulses [7, 8] is one of the most prominent applications of this phenomenon.

In the most widespread regimes of optical harmonic generation, the pump photons are physically indistinguishable, as they originate from a common laser radiation field. A special geometric arrangement of pump beams implemented in this work allows an experimental observation of the time order of ultrashort laser pulses on harmonic generation and optical frequency mixing processes. The proposed experimental technique suggests ways to apply coherent control methods [9, 10] to tailor the nonlinear-optical response of quantum systems in the condensed phase on the femtosecond time scale. Our approach can also be employed to

investigate the dynamics of vibrational wave packets [10–12] in organic nonlinear materials and to create fast switches and logic gates using such materials.

To unveil the physics behind the sensitivity of sum-frequency and optical-harmonic generation to the time order of ultrashort pump pulses, we employ a generic formalism operating with the time-dependent nonlinear-optical susceptibility of a medium. This formalism gives the following standard expression for the third-order nonlinear polarization of the medium responsible for third-harmonic generation $3\omega = \omega + \omega + \omega$ [3]:

$$P^{(3)} = \int_{-\infty}^{\infty} \int_{-\infty}^{\infty} \int_{-\infty}^{\infty} \chi^{(3)}(t_1, t_2, t_3) \tag{1}$$
$$\times E_1(t - t_1) E_2(t - t_2) E_3(t - t_3) dt_1 dt_2 dt_3,$$

where $\chi^{(3)}(t_1, t_2, t_3)$ is the cubic nonlinear-optical susceptibility and $E_i(t)$ are the envelopes of the pump fields.

On a two-photon resonance at the frequency 2ω, with the sum of two of the three pump photon frequencies coinciding with a transition frequency in a nonlinear quantum system, the third-order nonlinear-optical susceptibility is written as [13, 14]

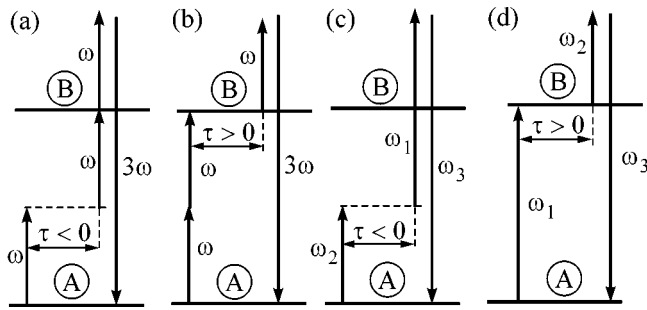$$\chi^{(3)}(t_1, t_2, t_3) = \chi_{TH}(t_1)\delta(t_1 - t_2)\delta(t_3). \tag{2}$$

Fig. 1. Diagrams of nonlinear-optical processes with time-ordered pump: (a, b) third-harmonic generation, $3\omega = \omega + \omega + \omega$, with a two-photon resonance at the frequency 2ω of transitions between states A and B; (c, d) sum-frequency generation, $\omega_3 = \omega_1 + \omega_2$, with a one-photon resonance. One of the ultrashort pump pulses is delayed by time τ with respect to the resonant excitation: (a, c) $\tau < 0$, (b, d) $\tau > 0$.

In the spectral representation, the nonlinear-optical susceptibility (2) depends only on the frequency 2ω, which corresponds to the condition of a two-photon resonance. Substituting Eq. (2) into expression (1) for the nonlinear polarization and assuming that the two-photon-resonant excitation is provided by one of the fields $E_1(t) = E_2(t)$, we arrive at

$$P^{(3)}(t) = E_3(t) \int_{-\infty}^{\infty} \chi_{\text{TH}}(t_1) E_1^2(t - t_1) dt_1. \qquad (3)$$

The power of the third harmonic is then given by

$$W_{\text{TH}}(\tau_3) \propto \int_0^{\infty} E_3^2(t - \tau_3) |Q(t)|^2 dt, \qquad (4)$$

where τ_3 is the delay time of the third pulse and

$$Q(t) = \int_0^{\infty} \chi_{\text{TH}}(t_1) E_1^2(t - t_1) dt_1. \qquad (5)$$

In the regime of a resonant excitation with infinitely short laser pulses, $E_i(t) = E_i\delta(t - \tau_i)$, $i = 1, 2, 3$, we derive

$$W_{\text{TH}} \propto \begin{cases} |\chi_{\text{TH}}(\tau)|^2 E_1^4 E_2^2, & \tau = \tau_3 - \tau_1 > 0, \qquad (6a) \\ 0, & \tau < 0. \qquad (6b) \end{cases}$$

A similar treatment for sum-frequency generation $\omega_3 = \omega_1 + \omega_2$ due to a quadratic nonlinearity

$$\chi^{(2)}(t_1, t_2) = \chi_{\text{SF}}(t_1)\delta(t_2) \qquad (7)$$

with a resonance at the frequency ω_2 in the field of infinitely short pump pulses, $E_{1,2}(t) = E_{1,2}\delta(t - \tau_{1,2})$, yields

the following expression for the power of the sum-frequency signal [14]:

$$W_{\text{SF}} \propto \begin{cases} |\chi_{\text{SF}}(\tau)|^2 E_1^2 E_2^2, & \tau = \tau_2 - \tau_1 > 0, \qquad (8a) \\ 0, & \tau < 0. \qquad (8b) \end{cases}$$

As it follows from Eqs. (6) and (8), a resonantly enhanced nonlinear signal is observed only for $\tau > 0$. A resonant excitation thus induces an asymmetry in the nonstationary nonlinear-optical response with respect to the instant of time when the resonant field is applied. This result can be illustrated with the use of simplified Feynman diagrams [15, 16] adapted to sum-frequency and third-harmonic generation. The diagrams shown in Figs. 1a and 1b represent the term in the quantum-mechanical expression for the nonlinear polarization of the medium that governs third-harmonic generation with a two-photon resonance at the frequency 2ω of a transition between states A and B for $\tau < 0$ and $\tau > 0$, respectively. With $\tau < 0$ (Fig. 1a), the contribution of this diagram to the total nonlinear polarization of the medium is negligibly small [Eq. (6b)] since the frequency ω is far from the transition frequencies of the quantum system. With $\tau > 0$ (Fig. 1b), states A and B become resonantly coupled by the laser field. The third field with the frequency ω is then scattered off the coherence induced in the medium, leading to a resonant generation of the third harmonic [Eq. (6a)]. For sum-frequency generation $\omega_3 = \omega_1 + \omega_2$, which is a process quadratic in the laser field, states A and B become resonantly coupled at the moment of time when the field with the frequency ω_1 is applied. The relevant term in the expression for the nonlinear polarization of the medium (Figs. 1c and 1d) leads to a resonant enhancement of the nonlinear-optical response for $\tau > 0$ [see Eq. (8a)].

Formulas (6) and (8) describe only one type of terms in the quantum-mechanical expressions for the total nonlinear-optical susceptibilities. In the most frequently used, collinear geometry of third-harmonic generation (Fig. 2a), three pump photons that give rise to a photon at a tripled frequency are physically indistinguishable. Introduction of a delay time between the pump pulses in this scheme leads to an interference of several resonant components in the nonlinear polarization of the medium represented by different Feynman diagrams. To select the term in the nonlinear polarization corresponding to the diagram shown in Fig. 1b, we used a noncollinear geometry of third-harmonic generation in the field of two crossing pump beams with wave vectors $\mathbf{k}_1$ and $\mathbf{k}_2$ (Fig. 2a). In this geometry, different resonant channels give rise to spatially separated third-harmonic signals. Detection of the third harmonic generated in this scheme in the direction of $2\mathbf{k}_1 + \mathbf{k}_2$ (Fig. 2a) selects the third-harmonic component represented by the diagram shown in Fig. 1b.

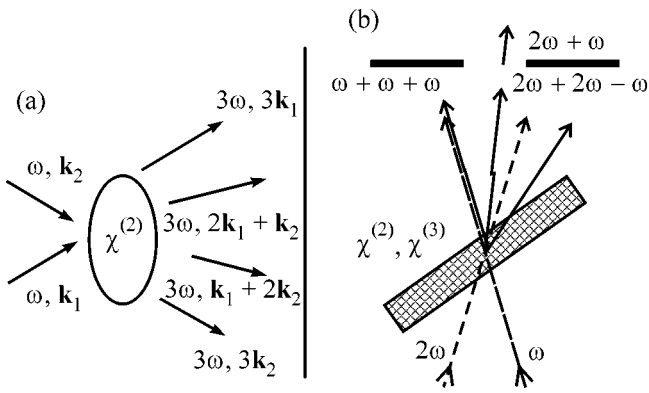The noncollinear geometry of nonlinear-optical interaction also allows a spatial filtering of the signal

Fig. 2. Diagrams of collinear and noncollinear geometries of (a) third-harmonic generation (the third harmonic is generated in the direction of the wave vectors $\mathbf{k}_1$ and $\mathbf{k}_2$ of the pump fields in the collinear regime and in the direction of the vectors $2\mathbf{k}_1 + \mathbf{k}_2$ and $\mathbf{k}_1 + 2\mathbf{k}_2$ in the noncollinear regime) and (b) sum-frequency generation, $3\omega = 2\omega + \omega$, due to a quadratic nonlinearity.

master oscillator, pumped with a fiber ytterbium laser, generated 30–50-fs light pulses with a repetition rate of 120 MHz, a central wavelength of 1250 nm, and a mean power of about 180 mW. These pulses were then transmitted through a stretcher and an isolator to be amplified in a Nd:YLF-laser-pumped amplifier. Amplified pulses with an energy up to 100 μJ were recompressed to a 50–100-fs pulse duration in a grating compressor. Approximately 50% of radiation energy was lost at this stage. An LBO crystal was used to generate the second harmonic of amplified Cr:forsterite-laser radiation. A more detailed description of the femtosecond Cr:forsterite laser system can be found elsewhere [17].

Thin films with azopolymer molecules (inset to Fig. 4), poled by an external electric field (the poling technique is described, e.g., in [18]) were used as samples of nonlinear-optical material in our experiments. In terms of symmetry operations, orientation of molecular dipoles induces a polar axis, removing the inversion center and lifting the prohibition on nonlinear-optical interactions quadratic in the laser field. Strong quadratic nonlinearity of poled azopolymer molecules originates from extended conjugate π-bonds. Delocalized π-electrons forming these bonds give rise to large dipole moments. The thickness of nonlinear films employed in our experiments was about 1 μm. Molecular dipoles were oriented in azopolymer films by poling in an interelectrode gap, with a dc voltage on the order of several kilovolts applied to the electrodes.

generated at the sum frequency $3\omega = 2\omega + \omega$ due to the quadratic nonlinearity of the medium from the signal emitted at the same frequency 3ω via direct and cascaded third-harmonic generation due to the cubic and quadratic nonlinearities, respectively. In the noncollinear geometry, the sum-frequency and third-harmonic signals are generated in different directions, determined by wave-vector matching for each of the processes (Fig. 2b).

The laser system employed in our experiments (Fig. 3) consisted of a Cr^{4+}: forsterite master oscillator, a stretcher, an optical isolator, a regenerative amplifier, a compressor, and a crystal for frequency doubling. The

Femtosecond pulses of fundamental Cr:forsterite laser radiation with a wavelength of 1.25 μm and 625-nm second-harmonic pulses were employed as pump fields ω and 2ω for third-harmonic generation, $3\omega = \omega + \omega + \omega$, and sum-frequency generation, $3\omega =$
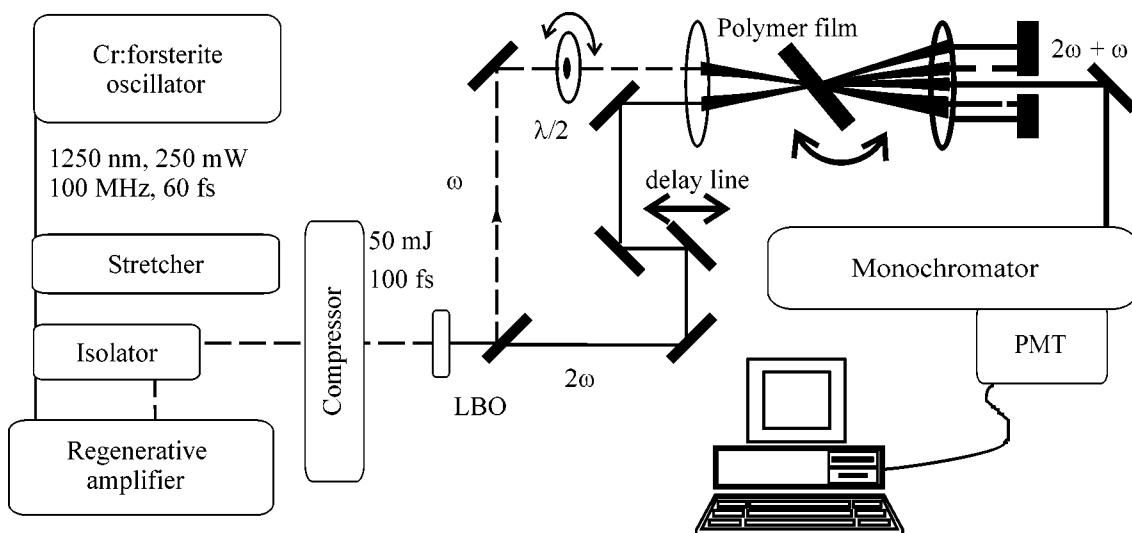

Fig. 3. Diagram of the experimental setup for the investigation of third-harmonic and sum-frequency generation by time-ordered pump in poled azopolymer films.
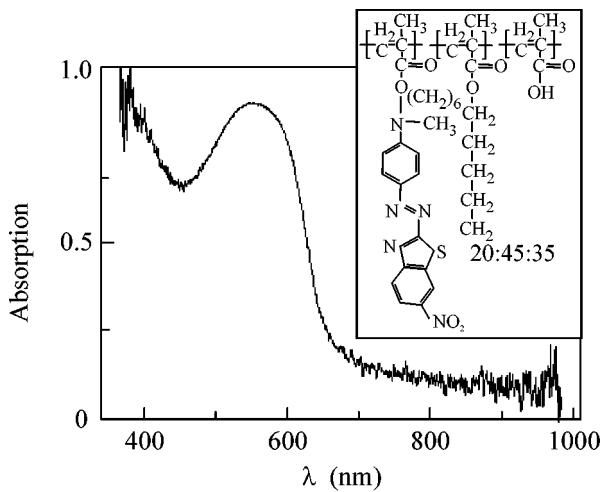
Fig. 4. Absorption spectrum of the film with azopolymer molecules oriented with an external field. The inset shows the chemical formula of azopolymer molecules.
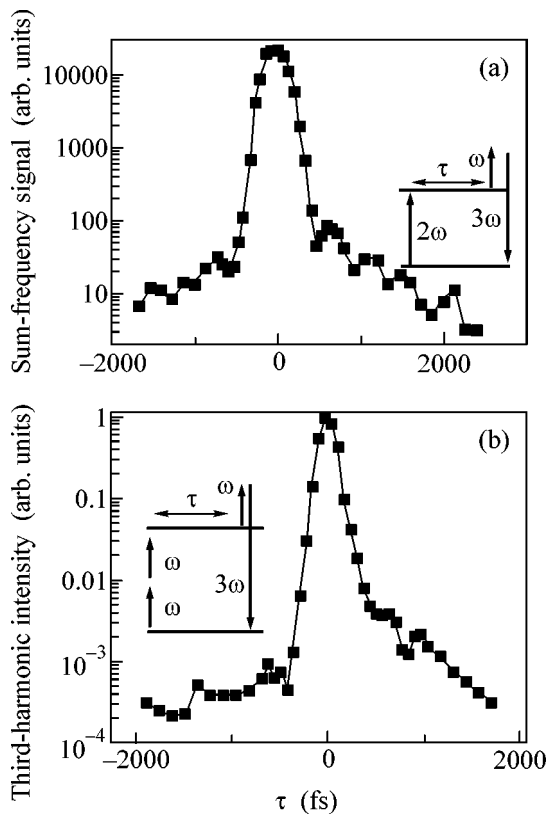

Fig. 5. Intensities of (a) the sum-frequency signal and (b) the third harmonic as functions of the delay time τ between the resonant excitation and the probe pulse. Diagrams of nonlinear-optical processes are shown in the insets.

$2\omega + \omega$. The wavelength of the second harmonic of Cr:forsterite laser radiation falls within the absorption band of azopolymer molecules under study (Fig. 4), leading to the enhancement of nonlinear-optical inter-

actions due to a one-photon resonance with the frequency of electronic transitions in azopolymer molecules in the case of sum-frequency generation and a two-photon resonance for second-harmonic generation.

The results of experimental studies of sum-frequency and third-harmonic generation by time-ordered pump pulses are presented in Figs. 5a and 5b. The zero delay time in both plots is defined as the instant of time when the intensity of the resonant pump field, coupling the ground and electronically excited states of azopolymer molecules, reaches its maximum. The intensities of the sum-frequency signal (Fig. 5a) and the third harmonic (Fig. 5b) as functions of the delay time τ between the resonance excitation and the probing pulse feature an asymmetry with respect to $\tau = 0$. The bandwidth of femtosecond pulses of the resonant pump field is sufficient to excite a whole group of vibrational levels in the electronically excited state of azopolymer molecules. Formation and evolution of vibrational wave packets in the condensed phase have been earlier studied by means of time-dependent coherent four-wave mixing [12]. In our experiments, the dynamics of vibrational wave packets, arising for $\tau > 0$, is manifested in an oscillatory behavior of the third-harmonic signal as a function of the delay time τ (Fig. 5b).

Our experiments thus demonstrate that the time order of ultrashort pump pulses may have a significant influence on the efficiency of optical harmonic generation and frequency mixing in transient regimes of nonlinear-optical interactions. The methodology developed and implemented in this work with the use of noncollinear geometries of sum-frequency and third-harmonic generation allows experimental observation of the influence of the time ordering of ultrashort laser pump pulses on nonlinear-optical phenomena. We have studied sum-frequency generation through three-wave mixing and third-harmonic generation in films with a quadratic nonlinearity related to molecular dipoles in azopolymers oriented by an external electric field. Femtosecond Cr:forsterite laser pulses induce transitions of azopolymer molecules to an electronically excited state and produce vibrational wave packets, leading to an asymmetry in the dependence of the efficiency of second- and third-order nonlinear-optical processes on the delay time between the pump pulses. This phenomenon suggests ways to control the nonlinear-optical response of quantum systems in the condensed phase on the femtosecond time scale. The proposed approach can be also employed to investigate the dynamics of vibrational wave packets in organic nonlinear materials and to create fast switches and logic gates using such materials.

REFERENCES

1. P. A. Franken, A. E. Hill, C. W. Peters, and G. Weinreich, Phys. Rev. Lett. **7**, 118 (1961).

2. V. G. Dmitriev and L. V. Tarasov, *Applied Nonlinear Optics* (Radio i Svyaz', Moscow, 1982) [in Russian].

3. Y. R. Shen, *The Principles of Nonlinear Optics* (Wiley, New York, 1984; Nauka, Moscow, 1989).

4. J. J. Macklin, J. D. Kmetec, and C. L. Gordon III, Phys. Rev. Lett. **70**, 766 (1993).

5. A. Paul, R. A. Bartels, R. Tobey, *et al.*, Nature **421**, 51 (2003).

6. Ch. Spielmann, N. H. Burnett, S. Sartania, *et al.*, Science **278**, 661 (1997).

7. P. M. Paul, E. S. Toma, P. Breger, *et al.*, Science **292**, 1689 (2001).

8. M. Drescher, M. Hentschel, R. Kienberger, *et al.*, Science **291**, 1923 (2001).

9. D. J. Tannor and S. A. Rice, J. Chem. Phys. **83**, 5013 (1985).

10. W. S. Warren, H. Rabitz, and M. Dahleh, Science **259**, 1581 (1993).

11. *Femtosecond Coherent Raman Spectroscopy*, Special Issue of J. Raman Spectrosc. **31** (1/2) (2000), Ed. by W. Kiefer.

12. D. Zeidler, S. Frey, W. Wohlleben, *et al.*, J. Chem. Phys. **116**, 5231 (2002).

13. A. N. Naumov and A. M. Zheltikov, Appl. Phys. B **77**, 369 (2003).

14. A. M. Zheltikov, Laser Phys. (in press).

15. D. Lee and A. C. Albrecht, in *Advances in Chemical Physics,* Ed. by I. Prigogine and S. A. Rice (Wiley, Chichester, 1993), Vol. 83, p. 43.

16. T. Chen, V. Engel, M. Heid, *et al.*, Vibr. Spectrosc. **19**, 23 (1999).

17. A. A. Ivanov, M. V. Alfimov, and A. M. Zheltikov, Usp. Fiz. Nauk **174** (7) (2004, in press).

18. *Nonlinear Optical Properties of Organic Molecules and Crystals*, Ed. by D. S. Chemla and J. Zyss (Academic, Orlando, 1987).

Translated by A. Zheltikov

Phase Transitions in Uranium Dioxide at High Pressures and Temperatures

A. M. Molodets* and V. E. Fortov

Institute of Chemical Physics, Russian Academy of Sciences,
Chernogolovka, Moscow region, 142432 Russia
* e-mail: molodets@icp.ac.ru
Received May 27, 2004; in final form, June 22, 2004

The melting curve is plotted for uranium dioxide with fluorite structure in a pressure range from –2.5 to +100 GPa. This curve has a peak at the point 3348 K, 6 GPa, and has a negative derivative at high pressures. The pressure corresponding to a polymorphic transition of uranium dioxide (37 GPa) at a temperature of 1015 K is determined. The slope of the equilibrium curve of the polymorphic transition in UO_2 in the temperature range 300–1000 K is –56 K/GPa. © 2004 MAIK "Nauka/Interperiodica".

PACS numbers: 64.70.-p

Uranium dioxide UO_2 is a key material in nuclear power engineering. The literature on thermophysical properties of this material is quite extensive (see reviews [1, 2] and the literature cited therein, as well as [3–6]). In most of these publications, UO_2 was studied under atmospheric pressure [1, 2], while the behavior of the material under high pressures (e.g., the study of polymorphic transformation of UO_2 [3]) was seldom investigated. However, interest in the behavior of UO_2 under high pressures and at high temperatures has increased in recent years. For example, the effect of elevated pressure on the melting point of UO_2 was analyzed in [4]. The study of track formation upon bombardment of UO_2 by high-energy particles in [5] necessitated the use of the equation of state for this material under high pressures of shock compression. Finally, to explain the behavior of point defects in UO_2, a number of calculations of potential energy from the first principles were performed for pressures up to tens of gigapascal (see [6]).

It should be noted, in connection with the importance of studying the thermodynamic properties of UO_2 at high pressures and temperatures, that detailed experimental data of shock compression of this material are available [7]. The ranges of pressures corresponding to shock compression and of the initial porosities of samples are such that a considerable part of experimental points obviously belong to the liquid phase of UO_2. Thus, certain experimental information on the properties of the melt and, probably, on polymorphic transformations of this material under the conditions of high pressures and temperatures is contained in the available shock adiabats. Consequently, we can try to extract information on the thermophysical properties of UO_2

from the experimental data on its strong shock compression.

In this communication, new information on the heat-transfer properties of phases, polymorphic transition, and melting of uranium dioxide at high pressures and temperatures is obtained by processing and analysis of experimental shock adiabats.

To calculate the temperature of UO_2 in shock waves and phase equilibrium curves, we used the thermodynamic potential method. The role of the basic thermodynamic potential was played by the Helmholtz energy $F(V, T)$. We used the semiempirical expression for $F(V, T)$ in the form

$$F(V, T) \tag{1}$$
$$= E_x + 3R(\theta/2 + T\ln(1 - \exp(-\theta/T))) - a_s RT + E_m.$$

In this expression, the notation is traditional, but the form of the key functions, namely, the characteristic temperature $\theta = \theta(V)$, which depends only on volume, and the potential energy $E_x = E_x(V)$, is defined by new formulas. These formulas were determined by integrating the Grüneisen coefficient, which depends only on the volume according to the law $\Gamma(V) = 2/3 + 2V/(aV_0 - V)$, where $a = \text{const} = 1 + 2/(\gamma_0 - 2/3)$ and γ_0 is the thermodynamic Grüneisen parameter under initial conditions.

Function $\theta(V)$ was determined by the integration of the equation $d\ln\theta/d\ln V = -\Gamma(V) = -2/3 - 2V/(aV_0 - V)$. To find $E_x(V)$, we used the equation $\gamma(E_x) = \Gamma(V) = 2/3 + 2V/(a_x V_0 - V)$, where a_x is a fitting parameter. In the case of solids, we used the Slater formula for $\gamma(E_x)$ (see [8]), $\gamma(E_x) = \gamma_s(E_x) = -2/3 - 0.5V(d^3E_x/dV^3)/(d^2E_x/dV^2)$. In the case of the melt, we used the Vashchenko–

Zubarev formula from [9]: $\gamma(E_x) = \gamma_{vz}(E_x) = -0.5V(d^2(V^{4/3}(dE_x/dV))/dV^2)/(d(V^{4/3}(dE_x/dV))/dV)$.

Parameter a_s in Eq. (1) is zero for the solid and unity for the melt. Constant E_m in Eq. (1) defines the zero level $E_x(V)$ for each phase. Constant E_m was set zero for solid UO_2. The value of E_m for the melt was determined from tabulated thermophysical characteristics of the UO_2 melt.

Parameter a_x for solid UO_2 was fitted to the experimental dependence of density ρ on temperature T, $\rho(T)$, at a constant atmospheric pressure for UO_2 with the fluorite structure in the temperature range 300–2670 K from the data presented in [1, 2]. The parameters of the material appearing in Eq. (1) (such as the bulk compression modulus, thermal expansion coefficient, density, characteristic temperature and heat capacity) in the initial state (P_0, V_0, T_0) are also taken for UO_2 with fluorite structure.

The semiempirical expression for $F(V, T)$ for liquid UO_2 was constructed using the same approach as for solid UO_2. The dependence $\rho(T)$ for the melt in the temperature range 3120–4000 K was also borrowed from the same publications [1, 2].

Figure 1 shows the shock adiabat for UO_2 with the fluorite structure (curve *1*) and melt (curve *2*), calculated using Eq. (1), against the background of the experimental data [7] obtained for porous UO_2 samples with initial density $\rho_0 = 10.337$ g/cm³ (porosity $m = 1.06$). The same figure shows the results of analogous calculations (curves *5* and *6*) for another initial density $\rho_0 = 6.346$ g/cm³ (porosity $m = 1.73$).

It can be seen from Fig. 1 that the calculated shock adiabats for solid UO_2 (curves *1* and *5*) coincide within the experimental error only with the first experimental points [7] up to pressures ~20–40 GPa. In the range of higher pressures, however, the calculated shock adiabats for melt (curves *2* and *6*) coincide with the experimental data [7]. Such a mutual arrangement of experimental and theoretical results makes it possible to single out two subsets from the set of experimental points [7]—points corresponding to solid UO_2 and points corresponding to the UO_2 melt. At the same time, the coincidence of theoretical shock adiabats 1, 5 and 2, 6 with different subsets of experimental points can be treated as evidence for the validity of the constructed thermodynamic potentials (1). These potentials describe, to a high degree of accuracy, the shock compressions of solid UO_2 up to pressures of ~20–40 GPa and, accordingly, for UO_2 melt in the pressure range ~30–150 GPa.

It should further be noted that the experimental shock adiabat for porosity $m = 1.06$ contains a phase transition accompanied by a decrease in the specific volume. This follows from two kinks on the shock adiabat of UO_2 and from their shape. Indeed (see Fig. 1), we can draw straight line *3* from the point $P = 0$, $u = 0$. Line *3*, $P = $const$u$, is plotted using the least-squares
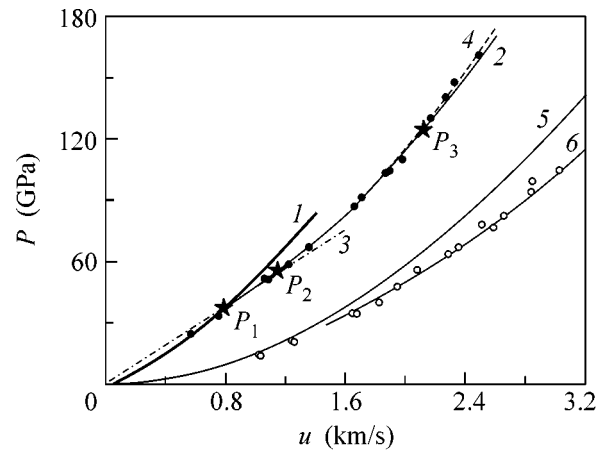

Fig. 1. Shock adiabats of UO_2 in the coordinates shock-compression pressure P vs. mass velocity u. ● and ○ correspond to experimental values [7] measured for $\rho_0 = 10.337$ g/cm³ and $\rho_0 = 6.346$ g/cm³, respectively. Solid curves are (*1*) the results of calculations of shock adiabat for UO_2 with fluorite structure for an initial density of 10.337 g/cm³ of the samples; (*2*) the shock adiabat of UO_2 melt under the shock compression of solid UO_2 samples with an initial density of 10.337 g/cm³; (*5*) the shock adiabat of UO_2 with fluorite structure for an initial density of 6.346 g/cm³; (*6*) the shock adiabat of UO_2 melt under the shock compression of solid UO_2 samples with an initial density of 6.346 g/cm³; the dot-and-dash line (*3*) corresponds to $P = $const$u$; the dashed curve (*4*) corresponds to the quadratic approximation of experimental points (●) that do not belong to UO_2 with fluorite structure. The point P_1 corresponds to the beginning of a polymorphic transition under shock compression; P_2 corresponds to the termination of the polymorphic transition under shock compression, and P_3 marks the end of melting of UO_2 with an unknown structure under the shock-compression conditions.

technique and passes through the point $P = 0$, $u = 0$ and through three experimental points (third, fourth, and fifth from [7]). Line *3* corresponds to a constant velocity $D = 4.54$ km/s of the shock wave. It can be seen that this line defines two kinks at pressures $P_1 = 37$ GPa and $P_2 \approx 55$ GPa. It is well known, however [10, 11], that the reason for such kinks are the transition from elastic to plastic compression and phase transitions. Since the experimental shock adiabat shown in Fig. 1 is the shock adiabat for initially porous samples, elastoplastic effects in such materials are weak. Consequently, the reason for the kinks on the experimental shock adiabat is only associated with a phase transition. The rightward deviation of the segment of the shock adiabat behind the kinks (for $P > P_1$) indicates that this phase transition is accompanied by a decrease in the specific volume. The temperature of shock compression for UO_2 calculated using formula (1) at pressure $P_1 = 37$ GPa is $T_1 = 1015$ K.
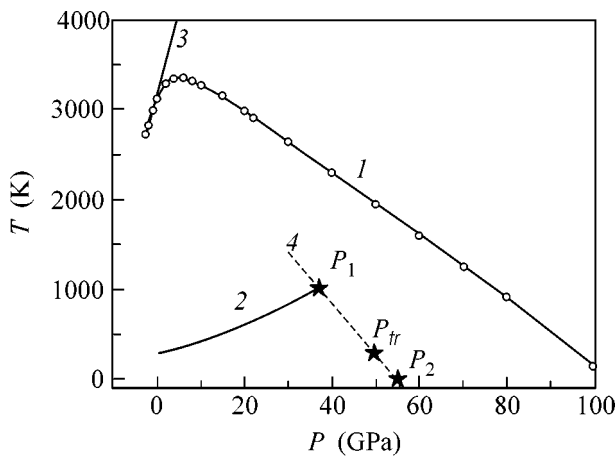
Fig. 2. Phase diagram and thermodynamic states of UO_2 under shock compression in the pressure P vs. temperature T coordinates: (*1*) the theoretical melting curve of UO_2 with fluorite structure; ○ are the results of specific calculations; (*2*) the theoretical shock adiabat for UO_2 with fluorite structure an initial density of 10.337 g/cm^3 of the samples. Straight line *3* describes the experimental slope of the melting curve for UO_2 in the pressure range 0–0.25 GPa from [4]. The dashed line *4* estimates the slope of the equilibrium line for a polymorphic transition in UO_2. The point P_1 correspond to the beginning of a polymorphic transition under shock compression; P_2 corresponds to the termination of the polymorphic transition under shock compression, and P_{tr} is the estimated pressure of the polymorphic transition in UO_2 at room temperature.

It was shown in [12] that the kink on shock adiabats at the point of the stability threshold, which corresponds to the phase transition, is small in the P–u coordinates and, hence, the pair of kinks in these coordinates identifies the beginning and end of the phase transition, to a high degree of accuracy (~1%). Thus, the kinks on the experimental shock adiabat of UO_2 in Fig. 1 determine the beginning of the phase transition under pressure $P_1 = 37$ GPa of shock compression and its termination at $P_2 \approx 55$ GPa. Accordingly, the temperature of this phase transition at pressure $P_1 = 37$ GPa is $T_1 = 1015$ K.

Generally speaking, the role of such a phase transition can be played either by melting {UO_2 *with fluorite structure*} ⟷ {UO_2 *melt*} or by the polymorphic transition {UO_2 *with fluorite structure*} ⟷ {UO_2 *with unknown structure*}. Let us prove that a polymorphic transition occurs in the present case (see Fig. 2).

Figure 2 shows melting curve *1* calculated using Eq. (1) for the transition {UO_2 *with fluorite structure*} ⟷ {UO_2 *melt*} in the range from tensile to megabar pressures. Each point on the melting curve was obtained from the numerical solution of the equality of the chemical potentials of solid UO_2 with fluorite structure and melt. It can be seen that melting curve *1* has a peak. The coordinates of this peak are $P_m = 6$ GPa

for pressure and $T_m = 3348$ K for temperature. At high pressures, melting curve *1* has a negative derivative $(dT/dP)_m < 0$. It can be seen that, in accordance with this curve, UO_2 with fluorite structure under pressures in the vicinity of 100 GPa melts at temperatures close to room temperature. However, in the pressure range near $P_1 = 37$ GPa, the melting point is $T_{ml} \approx 2400$ K, which is more than double the value $T_1 = 1015$ K.

In further analysis, we will use the following empirical rule (see [13]): "anomalous" melting curve with a negative slope $dT/dP < 0$ is a precursor of a polymorphic transition. Together with inequality $T_1 < T_{ml}$, this rule suggests that the phase transition at the point {P_1; T_1} is the polymorphic transition {UO_2 *with fluorite structure*} ⟷ {UO_2 *with unknown structure*}. It should be noted in this connection that melting curve *1* in Fig. 2 indicates the possible location of the triple point {UO_2 *with fluorite structure*} ⟷ {UO_2 *with unknown structure*} ⟷ {UO_2 *melt*}.

Let us estimate the slope of the equilibrium curve of the polymorphic transition {UO_2 *with fluorite structure*} ⟷ {UO_2 *with unknown structure*} and the pressure corresponding to this transition at room temperature. It was noted above that a polymorphic transition in a shock wave is accompanied by a decrease in specific volume. Consequently, the equilibrium curve describing this transition has a negative slope $dT/dP < 0$. Since the shock adiabat in the (P, T) coordinates in the region of mixed phases coincides with the equilibrium line of these phases [14], the temperature on the segment of the shock adiabat between the points P_1 and P_2 decreases. At the same time, the decrease in temperature along the shock adiabat cannot pass through zero temperature. Therefore, setting $T_2 \approx 0$ for estimates, we obtain the slope of the equilibrium line as $(dT/dP)_{tr} = -T_1/(P_2 - P_1) \approx -56$ K/GPa (see straight line *4* in Fig. 2).

The obtained value of $(dT/dP)_{tr}$ makes it possible to estimate the pressure P_{tr} corresponding to the polymorphic transition at room temperature ($T_{tr} \approx 300$ K): $P_{tr} \approx P_1 + (T_{tr} - T_1)/(dT/dP)_{tr} \approx 50$ GPa. It should be noted that the value of P_{tr} exceeds the pressure (29 GPa) of the polymorphic transition from [3].

Finally, let us estimate the pressure of shock compression at the point at which the shock adiabat emerges from the two-phase region {unknown solid phase–melt} by comparing the theoretical shock adiabat for UO_2 melt with experimental data. For this purpose, we note that, although curve *2* coincides to within the spread in experimental points with curve *4* (quadratic approximation of the experiment) (see Fig. 1), these two curves intersect at pressure $P_3 = 125$ GPa. Thus, if we identify the point of intersection of curve *2* and *4* in Fig. 1 with the emergence of the shock adiabat from the two-phase region {unknown solid phase–melt}, we can conclude that the termination of melting

Calculated characteristics of phase transitions in UO_2 with errors

P_1, GPa	T_1, K	P_2, GPa	P_3, GPa	P_{tr}, GPa	$(dT/dP)_{tr}$, K/GPa	P_{max}, GPa	T_{max}, K	$(dT/dP)_m$, K/GPa
37 ± 4	1015 ± 100	55 ± 6	125 ± 25	50 ± 10	-56 ± 30	6 ± 0.6	3348 ± 100	-35 ± 5

under shock compression of UO_2 with an unknown structure occurs at a pressure of 125 GPa.

In conclusion, let us consider the accuracy of the calculated values of pressures and temperatures.

The error in the obtained values is the sum of the errors in the experimental data used and the errors introduced by semiempirical relation (1). We assume that the error in the measurements of shock-wave velocity D and mass velocity u in shock experiments is typically ~1–2%, while the error in the initial density ρ_0 is 1%. Then the error in the experimental pressure of shock compression estimated in calculating the shock compression pressure by the momentum conservation law $P = \rho_0 D u$ is $P \approx 5\%$.

The error in calculation of pressure using formula (1) is mainly determined by the value of fitting parameter a_x. The value of this parameter depends on the precision of the experiment used for fitting the optimal value of a_x. As noted above, we used the available data on $\rho(T)$ from [1, 2]. The error in these data amounts approximately to 1–3%, according to [1, 2]. The variation of parameter a_x corresponding to these values leads to variation of calculated pressures to within 10%. The same value is typical of calculated values of the temperature corresponding to shock compression of solid UO_2.

Summarizing these errors, we obtain the total estimate of the accuracy of calculated values of P and T at 10–15%.

It should be noted that the formal estimate of the error in determining the pressure at the point P_3 is large (on the order of 100%). However, an analysis of the mutual arrangement of experimental points and theoretical curves in the $\{D; u\}$ coordinates makes it possible to reduce the uncertainty in the value of P_3 to $\approx 20\%$.

The table summarizes the quantitative results with errors.

REFERENCES

1. J. K. Fink, M. G. Ghasanov, and L. Leibowitz, J. Nucl. Mater. **102**, 17 (1981).
2. J. K. Fink, J. Nucl. Mater. **279**, 1 (2000).
3. U. Benedict, G. D. Andreetti, J. M. Fournier, *et al.*, Phys. Lett. **43**, L171 (1982).
4. M. Manara, C. Ronchi, and M. Sheindlin, Int. J. Thermophys. **23**, 1147 (2002).
5. C. Ronchi and T. Wiss, J. Appl. Phys. **92**, 5837 (2002).
6. J. P. Crocombette, F. Jollet, L. Thien Nga, *et al.*, Phys. Rev. B **64**, 104 107 (2001).
7. *LASL Shock Hugoniot Data*, Ed. by S. P. Marsh (Univ. of California Press, Berkeley, 1980).
8. A. M. Molodets, Fiz. Goreniya Vzryva **34**, 94 (1998).
9. V. Ya. Vashchenko and V. N. Zubarev, Fiz. Tverd. Tela (Leningrad) **5**, 886 (1963) [Sov. Phys. Solid State **5**, 653 (1963)].
10. L. V. Al'tshuler, Usp. Fiz. Nauk **85**, 197 (1965) [Sov. Phys. Usp. **8**, 52 (1965)].
11. N. M. Kuznetsov, Prikl. Mekh. Tekh. Fiz., No. 1, 111 (1966).
12. A. M. Molodets, High Temp. **40**, 484 (2002).
13. S. M. Stishov, Usp. Fiz. Nauk **96**, 467 (1968) [Sov. Phys. Usp. **11**, 816 (1970)].
14. S. B. Kormer, M. V. Sinitsyn, A. G. Kirillov, *et al.*, Zh. Éksp. Teor. Fiz. **48**, 1033 (1965) [Sov. Phys. JETP **21**, 689 (1965)].

Translated by N. Wadhwa

Dynamics and Spectra of Excited States of Water–Micellar Suspensions of Single-Walled Carbon Nanotubes

V. A. Nadtochenko[1, *], A. S. Lobach[1], F. E. Gostev[2], O. M. Sarkisov[2], D. O. Shcherbinin[2], and E. D. Obraztsova[3]

[1] *Institute of Energy Problems of Chemical Physics, Chernogolovka Branch, Russian Academy of Sciences, Chernogolovka, Moscow region, 142432 Russia*
*e-mail: nadto@icp.ac.ru
[2] *Semenov Institute of Chemical Physics, Russian Academy of Sciences, ul. Kosygina 4, Moscow, 101999 Russia*
[3] *Institute of General Physics, Russian Academy of Sciences, ul. Vavilova 38, Moscow, 119991 Russia*
Received June 3, 2004; in final form, June 22, 2004

The dynamics of the photoinduced differential absorption and excited-state bleaching spectra of single-walled carbon nanotubes suspended in a micellar solution were studied in the spectral range from 40 to 1000 nm within a time interval from 70 fs to 150 ps under excitation by 50-fs pulses with photon energies 2 and 4 eV. The bleaching and absorption bands were observed in the spectra; the positions of the bleaching peaks were independent of the photon energy of the exciting femtosecond pulse in the range 2–4 eV. It was established that, for delay times shorter than 1 ps, the shape of the differential spectrum of excited nanotubes coincided with the shape of the second derivative of the absorption spectrum of unexcited nanotubes in the frequency range of exciting pulse above 18000 cm^{-1} (the range of absorption bands of metallic nanotubes). In the frequency range below 16000 cm^{-1} (the range of absorption peaks of semiconducting nanotubes), the bleaching peaks in the differential spectrum of excited nanotubes undergo a high-frequency shift of 200–300 cm^{-1} with respect to the second-derivative spectrum of unexcited nanotubes. The excited-state relaxation rate constants were measured. They are well approximated by the exponential dependences and depend on the probe-pulse wavelength. An assumption was made about the nature of the observed spectra of excited nanotubes and about the excitation relaxation. © *2004 MAIK "Nauka/Interperiodica".*

PACS numbers: 82.70.Kj; 78.67.Ch

Single-walled carbon nanotubes (SCNs) are of interest as a new material for nonlinear optical and optoelectronic devices [1]. In this connection, information about the nature of electron-excited states of nanotubes, their spectra, and relaxation dynamics is of great importance. The first results on the excited-state relaxation dynamics of SCN suspended in a detergent were recently obtained by the methods of absorption and fluorescence femtosecond spectroscopy by excitation in the E_{11} transition range [2–5]. In those works, optical schemes with narrow-band spectral tuning of the probe pulse were used. We report data on the spectra of electron-excited states of SCN in a water–micellar suspension over a broad spectral range from 400 to 1000 nm obtained through excitation by 50-fs light pulses with photon energies of 2.0 eV (616 nm) and 4.0 eV (308 nm).

EXPERIMENTAL

SCNs prepared by catalytic decomposition of carbon oxide on iron at high CO pressure (30–50 atm) and a temperature of 900–1100°C (HiPco method [6]) were used in the experiment. The starting nanotube material (Carbon Nanotechnologies) contained 80 wt % pure nanotubes and ~20 wt % iron in the form of metal nanoparticles encapsulated into graphene layers. Nanotube suspensions in a 1 wt % water–micellar solution of sodium dodecyl sulfate were prepared by the following procedure. A batch of nanotubes (2.5 mg) was poured over with 20 ml of 1 wt % water–micellar solution of sodium dodecyl sulfate and dispersed for 2 h using ultrasound (UZDN-1, frequency 35 kHz, power 500 W) [7]. The suspension solution was centrifuged for 5 h with an acceleration of 8000, whereupon the centrifugate was decanted and used in optical experiments. After centrifuging, the residue was filtered through a track membrane (0.2 μm), dried, and weighed. The concentration of nanotubes in the centrifugate was determined from the difference between the weights of the starting nanotubes and the residue. It was found to be 22 μg/ml. The final value pH = 6. The homogeneous solution of nanotube suspension was stable for more than three months. The nanotube distribution in diameters was determined from the visible and near-IR absorption spectra and from Raman spectra. The diameters were found to lie within 0.7–1.1 nm [8].

The dynamics of the photoinduced differential spectra were measured using femtosecond absorption spectroscopy by the pump–probe technique. The excitation

was accomplished by a 50-fs laser pulse with the wavelength $\lambda = 616$ nm or $\lambda = 308$ nm and a pulse energy of 3 μJ. A white-supercontinuum pulse ($\lambda = 390$–1000 nm) obtained by the transformation of the pulse of wavelength $\lambda = 616$ nm in water was used as a probe pulse. The polarizations of the pump and probe pulses were oriented at a magic angle. Experiments were carried out in a 1-mm flow cell at room temperature under aerobic conditions. The spectra were recorded in a two-channel optical scheme using two diode gages after spectral decomposition of the white-supercontinuum pulse in a spectrograph. The quantity $\Delta D(\nu, t) = -\log(E(\nu, t)/E_0(\nu, t))$ was measured, where $E(\nu, t)$ is the probe-pulse energy at frequency ν and at time delay t and $E_0(\nu, t)$ is the pulse energy in the reference channel. The details of the experimental setup and the method of processing experimental data are described in [9].

RESULTS AND DISCUSSION

Figure 1 shows the differential absorption spectra $\Delta D(\nu)$ of the nanotube suspensions excited by a pulse with photon energy (a) 2 and (b) 4 eV and a time delay up to 1 ps. For comparison, a fragment of the absorption spectrum of the unexcited nanotubes in the sample under study is also shown in these figures. The $\Delta D(\nu)$ spectra were obtained with a fluence of 3 mJ/cm^2, for which, as was established, the signal in the differential spectrum $\Delta D(\nu)$ becomes saturated.

The absorption spectra of SCNs were studied in detail in [4, 10–12]. Based on the results of those works, it may be thought that the absorption peaks of our sample in the range above 18000 cm^{-1} can be assigned to the metallic nanotubes, the peaks in the range 12000–16000 cm^{-1} are due to E_{22}-type transitions of the nanotubes with semiconducting properties, and the peaks in the range below 12000 cm^{-1} are due to E_{11} transitions of the semiconducting nanotubes. The sample under study contains nanotubes of various chirality and size (0.7–1.1 nm). It is suggested that the individual peaks in the absorption spectra of nanotubes in water–micellar suspensions can be assigned to the transitions of the individual nanotubes with a particular diameter and chiral angle [10]. The peaks in the absorption spectra correspond to the Van Hove singularities in the density of states [13]. A broad shoulder in the absorption spectrum in Fig. 1 is the sum of contributions from the plasmon peak [14] with a maximum near 5 eV (4.8 eV for this sample) and from the nonresonance absorption of energy bands.

The following characteristic features are observed in the differential spectra $\Delta D(\nu)$ after excitation by a pulse with a photon energy of 2 eV and a pulse with a photon energy of 4 eV. The spectra contain bleaching peaks $\Delta D < 0$, whose positions are independent of the exciting-pulse energy (2 or 4 eV); a broad bleaching band appears in the range from 10000 to 20000 cm^{-1}
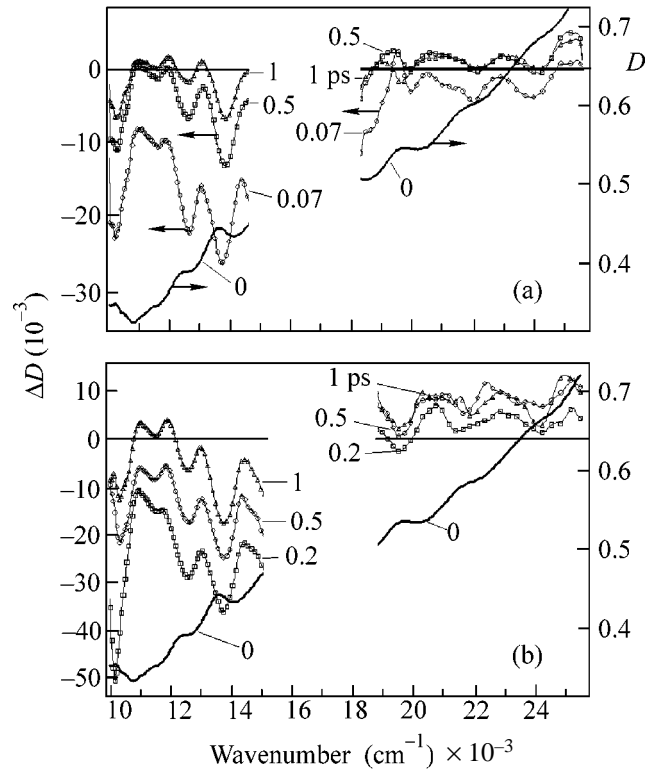

Fig. 1. Absorption spectrum of SCN in a 2-mm cell (line 0) and differential absorption spectra for various delay times after excitation by a femtosecond pulse with photon energies (a) 2 and (b) 4 eV.
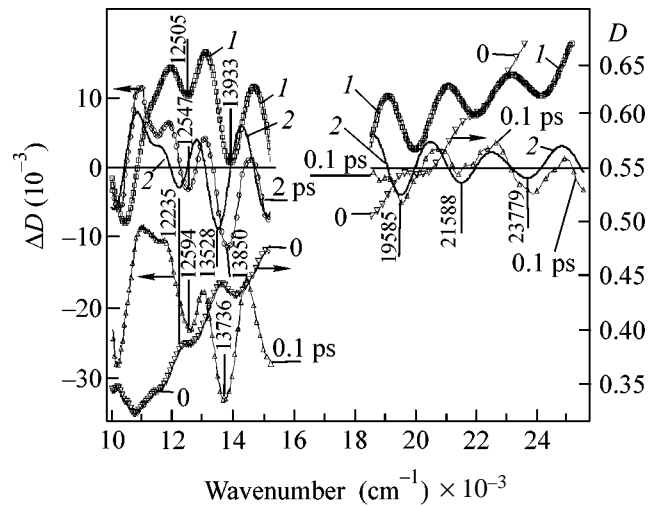

Fig. 2. Comparison of the differential absorption spectra $\Delta D(\nu)$ for various delay times with the absorption spectrum $D(\nu)$ (line 0), first derivative $dD(\nu)/d\nu$ (line 1), and second derivative $d^2D(\nu)/d\nu^2$ (line 2).

(for delays shorter than 100 fs), whose intensity increases upon moving to its low-frequency side; and the absorption bands $\Delta D > 0$ appear, which are
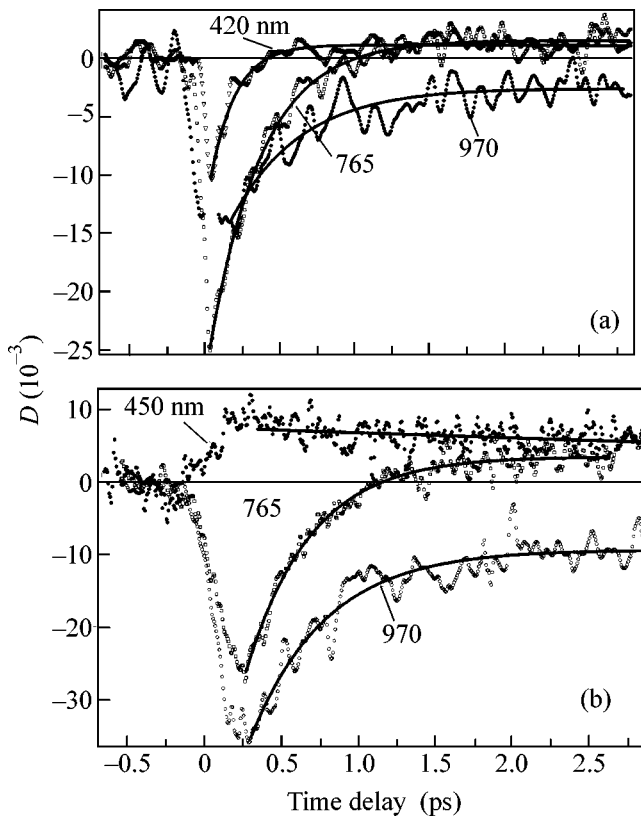
Fig. 3. Relaxation curves for various wavelengths after the excitation of nanotube suspension by a femtosecond pulse with photon energy (a) 2 and (b) 4 eV. Relaxation constants for various wavelengths: (a) $k_{420} = 6.0 \pm 0.2$ ps^{-1}, $k_{765} = 2.91 \pm 0.047$ ps^{-1}, and $k_{970} = 2.18 \pm 0.11$ ps^{-1}; (b) for the ascending phase, $k_{450}^{a} = 3.5 \pm 0.9$ ps^{-1}, $k_{765}^{a} = 4.76 \pm 0.64$ ps^{-1}, and $k_{970}^{a} = 5.6 \pm 0.8$ ps^{-1}; and for the descending part, $k_{450}^{d} = 0.10 \pm 0.02$ ps^{-1}, $k_{765}^{d} = 2.39 \pm 0.05$ ps^{-1}, and $k_{970}^{d} = 2.04 \pm 0.08$ ps^{-1}.

observed, along with the bleaching signal $\Delta D < 0$, for certain delay times. It is likely that the broad bleaching band in the form of a "background" for the bleaching peaks is caused by the plasmon excitation in nanotubes.

The positions of bleaching peaks in the differential spectra $\Delta D(\nu)$ replicate the absorption peaks in $D(\nu)$ of the unexcited sample, but with a frequency shift. As the delay time between the exciting and probe pulses increases, the bleaching peaks undergo a frequency shift. One can see in Fig. 2, e.g., that the maxima of bleaching peaks at 13 736 and 12 594 cm^{-1} for a delay time of 100 fs shift to the maxima, respectively, at 13 850 and 12 547 cm^{-1} for a delay time of 1 ps.

It is conceivable that multielectron interactions in SCN are at the basis of the observed features in the femtosecond absorption spectra. The spectrum of excited SCN is determined by two factors: (1) optical transitions of quasiparticles (excitons, electron–hole pairs,

etc.) that are formed as a result of the excitation and (2) optical transitions of the remaining unexcited electronic system in the valence band. The appearance of a considerable concentration of nonequilibrium excited states (quasiparticles) in SCN under the action of femtosecond pulses can noticeably disturb the whole electronic system through the correlation effects in the electron–electron interaction. After excitation, this disturbance manifests itself as a shift and/or broadening of absorption bands of the remaining unexcited electronic system in the valence band. As a result, the differential spectrum $\Delta D(\nu, t) = D^*(\nu, t) - D(\nu)$ consists of a series of bleaching and absorption bands. In Fig. 2, the absorption spectra $D(\nu)$ of nanotube suspensions, their first derivative $dD(\nu)/d\nu$, and second derivative $d^2D(\nu)/d\nu^2$ are compared with the postexcitation differential spectra $\Delta D(\nu)$. In the region below 16 000 cm^{-1} (semiconducting SCNs), the bleaching peaks in $\Delta D(\nu)$ are shifted by 200–300 cm^{-1} to high frequencies from the peaks in the absorption spectrum $D(\nu)$. Below 16 000 cm^{-1}, the second derivative $d^2D(\nu)/d\nu^2$ of the absorption spectrum qualitatively replicates the shape of differential spectra $\Delta D(\nu)$ for delays of 100 fs and 1 ps, but the differential spectra $\Delta D(\nu)$ are shifted to high frequencies relative to the second-derivative spectrum. In the region higher than 18 000 cm^{-1} (metallic SCN), the differential spectrum $\Delta D(\nu)$ for a delay time of 100 fs coincides, to a rather high accuracy, with the shape of $d^2D(\nu)/d\nu^2$. In the region $\nu > 18 000$ cm^{-1}, the shift of bleaching peaks in $\Delta D(\nu)$ from the peaks in the absorption spectrum $D(\nu)$ is small.

The low-energy shift of absorption peaks $D^*(\nu)$ of an excited SCN from the peaks ΔD of unexcited SCN and the broadening of these peaks in $D^*(\nu)$ upon excitation must lead to the appearance of the bleaching peaks in the differential spectrum $\Delta D(\nu) = D^*(\nu) - D(\nu)$. The analogous similarity effect between the shapes of the second derivative of the absorption spectrum and the postexcitation differential spectrum was observed for the C$_{60}$ films in [15]. For C$_{60}$, the appearance of random local electric fields $\Delta \mathbf{E}_i$ upon optical excitation of charge carriers was assumed to be the cause of broadening [15]. This resulted in the broadening of the density of states and "spreading" of the spectral features associated with the transitions at the critical points. As a result of these effects, the absorption spectrum changes, and the shape of the postexcitation $\Delta D(\nu)$ spectrum replicates the $d^2D(\nu)/d\nu^2$ shape of the unexcited sample. The broadening in $D^*(\nu)$ can also be caused by an increase in the scattering rate of excited carriers and other effects [16]. The observed shift for the semiconducting nanotubes is likely caused by the electron–electron and exciton interactions in SCNs [17].

An additional qualitative proof for the appearance of the bleaching peaks in $\Delta D(\nu, t)$ because of the excitation-induced shift and broadening of valence electrons is the fact that the peak positions weakly depend on

photon energy upon changing from 2 to 4 eV. This indicates that it is the number of excited states that plays the main role rather than their energy distribution.

Figure 3 shows that the relaxation curves for different frequencies of the probe pulse in a time interval shorter than 2 ps are well approximated by the exponential increase and decrease of the signal. The relaxation constants are different for different wavelengths of the probe pulse. The difference in the relaxation constants can be explained by the trivial effect of the presence of nanotubes with different properties and having different absorption peaks and different relaxation constants. Moreover, it is improbable that the relaxation constants can depend on the excitation energy for individual tubes [15, 18].

Note that the relaxation constants of the bands in the range below 16000 cm^{-1} (semiconducting nanotubes) are close to 2–3 ps^{-1}. These data are in agreement with the data on the relaxation constants for the excited water–micellar suspension of semiconducting nanotubes in the edge of E_{11} transitions ($\nu < 12000$ cm^{-1}). According to the data of those works, the relaxation constants also lie in the range of 2–3 ps^{-1} [2, 3, 5]. The bleaching relaxation at frequencies higher than 18000 cm^{-1} (metallic tubes) is faster, as is seen from Fig. 3, and is caused by electron and hole cooling. The relaxation after excitation by 4 eV is slightly slower than for 2 eV. After excitation by 4 eV, the increase in the intensity of bleaching peaks is observed at delay times shorter than 150 fs.

Figure 4 shows that, on the picosecond time scale, the differential spectra $\Delta D(\nu)$ show the same system of bleaching and absorption peaks as for the femtosecond time delays. However, the broad bleaching band disappears at these time delays.

The typical relaxation curves for the picosecond range are shown in Fig. 5. The relaxation constants for different probe frequencies differ appreciably, indicating the presence of different tubes in the sample. Note that the $\Delta D(\nu)$ spectra are quite similar for the picosecond delay times with excitation by 2- and 4-eV photons. But the relaxation constants are different for these photons. Whereas the fast relaxation for semiconducting tubes with constants 2–3 ps^{-1} can be attributed to the intraband relaxation, the picosecond relaxation with constants 0.03–0.14 ps^{-1} should be attributed to the interband relaxation [2, 3]. It is conceivable that the differential spectrum $\Delta D(\nu)$ on the picosecond time scale is caused by the absorption of trapped carriers and/or excitonic states [19].

Note in conclusion that we have used the method of femtosecond absorption spectroscopy with a broadband probe pulse to observe some effects in the electron–electron interactions in SCNs: (1) the appearance of bleaching and absorption peaks on the background of a broad bleaching band for short delay times of 1–1.5 ps. The bleaching intensity decays with a character-
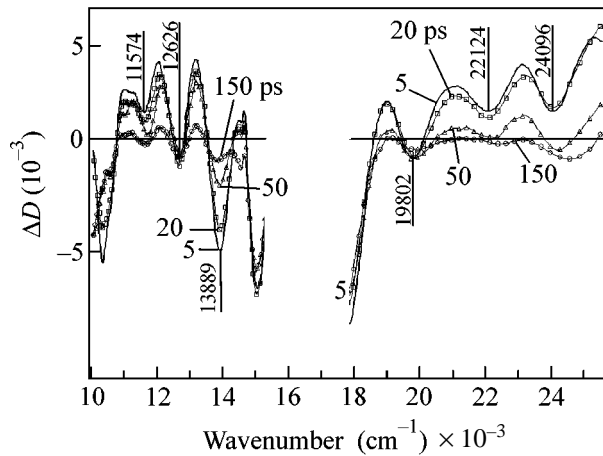
Fig. 4. Differential absorption spectra after excitation by a pulse with a photon energy of 2 eV in the region of picosecond delay times. For a spectrum with a delay time of 5 ps, the positions of bleaching peaks are indicated.
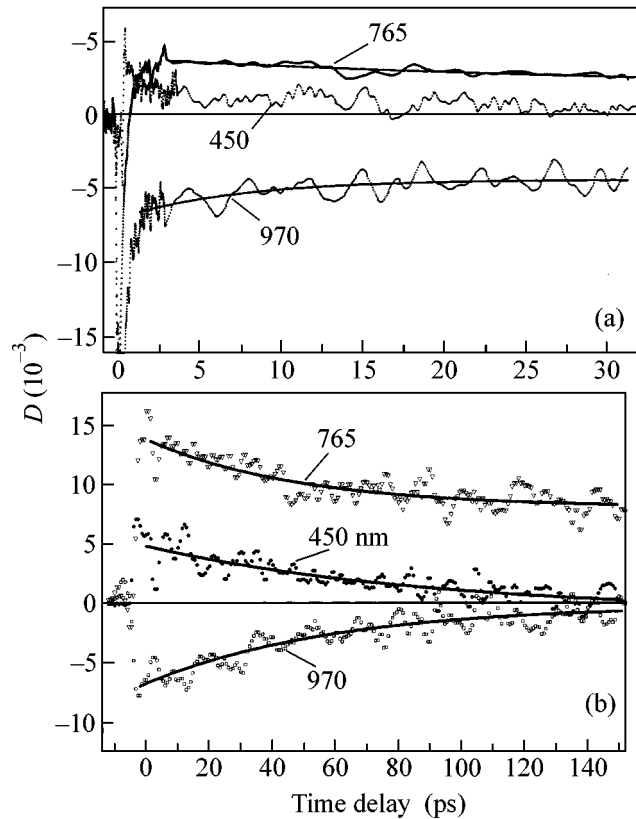

Fig. 5. Relaxation curves for various wavelengths after the excitation of nanotube suspension by a femtosecond pulse with photon energy (a) 2 and (b) 4 eV. The long-lived part of the relaxation curve is approximated by the exponent with relaxation constants (a) $k_{760\,nm} = 0.031 \pm 0.008$ ps^{-1}, $k_{450\,nm} = 0.14601 \pm 0.0215$ ps^{-1}, and $k_{970\,nm} = 0.13671 \pm 0.016$ ps^{-1}; (b) $k_{765\,nm} = 0.021 \pm 0.0028$ ps^{-1}, $k_{450\,nm} = 0.0113 \pm 0.0025$ ps^{-1}, and $k_{970\,nm} = 0.017 \pm 0.002$ ps^{-1}.

istic time from 100 to 500 fs, depending on the probe wavelength; (2) the differential spectrum coincides with the second derivative $d^2D(\nu)/d\nu^2$ of the spectrum of unexcited metallic SCNs; (3) the peaks in the differential spectrum are shifted by 200–300 cm^{-1} from the peaks in the absorption spectrum of unexcited semiconducting SCNs, while the differential spectra and the second derivative $d^2D(\nu)/d\nu^2$ of the unexcited semiconducting SCNs are similar. Long-lived excited states with a lifetime from 70 to 150 ps have been observed in metallic and semiconducting SCNs. The characteristic lifetime depends on the probe wavelength and photon energy of exciting light.

REFERENCES

1. D. A. Akimov, M. V. Alfimov, S. O. Konorov, *et al.*, Laser Phys. **13**, 1279 (2003).

2. J. Kono, G. N. Ostojic, S. Zaric, *et al.*, Appl. Phys. A: Mater. Sci. Process. **78**, 1093 (2004).

3. G. N. Ostojic, S. Zaric, J. Kono, *et al.*, Phys. Rev. Lett. **92**, 117402 (2004).

4. Y.-Z. Ma, J. Stenger, J. Zimmerman, *et al.*, J. Chem. Phys. **120**, 3368 (2004).

5. H. Hippler, A.-N. Unterreiner, J.-P. Yang, *et al.*, Phys. Chem. Chem. Phys. **6**, 2387 (2004).

6. P. Nikolaev, M. J. Bradley, F. Rohmund, *et al.*, Chem. Phys. Lett. **313**, 91 (1999).

7. A. S. Lobach, N. G. Spitsyna, S. V. Terekhov, and E. D. Obraztsova, Fiz. Tverd. Tela (St. Petersburg) **44**, 457 (2002) [Phys. Solid State **44**, 475 (2002)].

8. E. D. Obraztsova, M. Fujii, S. Hayashi, *et al.*, in *Nano-engineered Nanofibrous Materials*, Ed. by S. I. Guceri, Y. Gogotski, and V. Kuznetsov; NATO ASI Ser., Ser. 2 **169**, 389 (2004).

9. E. N. Ushakov, V. A. Nadtochenko, V. A. Gromov, *et al.*, Chem. Phys. **298**, 251 (2004).

10. S. M. Bachilo, M. S. Strano, C. Kittrell, *et al.*, Science **298**, 2361 (2002).

11. V. C. Moore, M. S. Strano, E. H. Haroz, *et al.*, Nano Lett. **3**, 1379 (2003).

12. M. J. O'Connell, S. M. Bachilo, C. B. Huffman, *et al.*, Science **297**, 593 (2002).

13. M. F. Lin, Phys. Rev. B **62**, 13153 (2000).

14. S. Kazaoui, N. Minami, H. Yamawaki, *et al.*, Phys. Rev. B **62**, 1643 (2000).

15. V. M. Farztdinov, A. I. Dobryakov, V. S. Letokhov, *et al.*, Phys. Rev. B **56**, 4176 (1997).

16. S. Stagira, M. Nisoli, and S. De Silvestri, Chem. Phys. **251**, 259 (2000).

17. C. L. Kane and E. J. Mele, Phys. Rev. Lett. **90**, 207401 (2003).

18. T. Hertel, R. Fasel, and G. Moos, Appl. Phys. A: Mater. Sci. Process. **75**, 449 (2002).

19. O. J. Korovyanko, C.-X. Sheng, Z. V. Vardeny, *et al.*, Phys. Rev. Lett. **92**, 17403 (2004).

Translated by V. Sakun

Reflection Spectrum of a Cholesteric Liquid Crystal with Structural Defects

A. V. Shabanov[1], S. Ya. Vetrov[2,] *, and A. Yu. Karneev[1]

[1] *Kirenskii Institute of Physics, Siberian Division, Russian Academy of Sciences, Krasnoyarsk, 660036 Russia*
[2] *Krasnoyarsk State Technical Unversity, Krasnoyarsk, 660074 Russia*
*e-mail: chery@escapenet.ru
Received May 17, 2004; in final form, June 22, 2004

An expression is obtained for the reflection coefficient of circularly polarized light normally incident on the film of a cholesteric liquid crystal with a variable helix pitch. It is shown that, in the case of a single defect (local change in the helix pitch), the spectrum of light reflection from a cholesteric acquires a dip corresponding to the defect mode. New qualitative features appear in the reflection spectrum of a cholesteric with two defects as the distance between them varies. © *2004 MAIK "Nauka/Interperiodica".*

PACS numbers: 78.20.Ci

In dielectric media known as photonic crystals, whose dielectric properties periodically vary within a spatial scale on the order of the optical wavelength, a fundamentally new electromagnetic effect can be realized. This is the phenomenon of light localization in defect modes with discrete frequencies lying in the band gaps of an unperturbed photonic crystal [1, 2]. The defect modes can be used to create narrowband filters [3, 4] in information and communication technologies [5, 6], and for low-threshold lasers [7]. In recent years, interest has been expressed in cholesteric liquid crystals (CLCs), which are one-dimensional photonic crystals with a photon band gap for light propagating along the helix axis of a CLC with a circular polarization coinciding with the sign of the cholesteric helix [8]. Light waves with the opposite circular polarization are transmitted through the cholesteric medium without distortion. For CLCs, two ways of defect introduction were proposed: a thin layer of an isotropic substance introduced between two cholesteric layers [9] and a defect caused by the phase jump in the cholesteric helix at the interface between two layers of a cholesteric polymer film [10]. The fact that a defect mode can be induced in a CLC by introducing a phase jump in the helix was experimentally verified in [11].

In this paper, we investigate the reflection spectrum of a CLC with a defect of a new type: a local change in the helix pitch. We also study the features of the reflection spectrum of a cholesteric with two structural defects depending on the distance between them. The structure under consideration is a CLC film whose width is equal to N helix pitches, and the external medium is isotropic and characterized by the mean refractive index of the cholesteric under study: $n = $

$\frac{1}{2}(n_\parallel + n_\perp)$. We assume that the helix pitch may locally deviate from the pitch P of a perfect CLC, which is commensurate with the light wavelength. We assume that the structure is right-handed and that clockwise-polarized light is normally incident on the film and propagates along the axis of the helix. This geometry of the problem makes it possible to adjust to our needs a simple method of investigation that was developed for X-ray diffraction by perfect crystals and successfully used for describing the reflection spectrum of a perfectly organized CLC [12]. In the general case, the problem stated has a solution in the framework of the rigorous approach based on the theory of electromagnetism with the use of the method developed for describing the optical properties of inhomogeneous anisotropic layered media [13]. However, in the case under consideration, where light is normally incident on the film surface and propagates along the helix axis, the solution is simplified. At the same time, the results of calculating the reflection coefficient for a perfect cholesteric in the absence of dielectric boundaries in terms of the dynamic diffraction theory (Fig. 1) and the rigorous approach based on the electromagnetic theory virtually coincide [8, 12]. In addition, when the external medium outside the cholesteric is isotropic with a refractive index of the cholesteric under study $n = \frac{1}{2}(n_\parallel +$

$n_\perp)$, the Fresnel reflection from the film surface and the interference fringes from the boundary surfaces are weak. Such conditions can easily be realized in an experiment. In terms of the dynamic model, the reflection of light from the cholesteric is only determined by the diffraction by its structure, which allows us to correctly investigate the effect of defects on the reflection
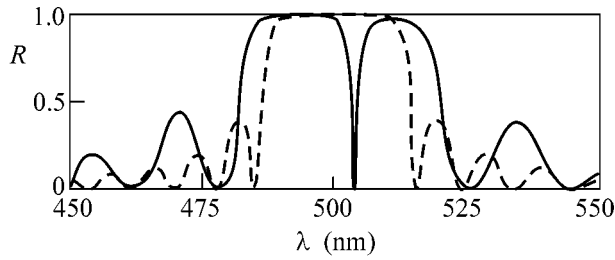
Fig. 1. Dependence of the reflection coefficient on the wavelength at normal incidence of light on the CLC. The dashed line corresponds to a perfect structure, and the solid line, to the structure with a defect. The parameters of the perfect CLC are $n = 1.5$, $\delta n = 0.07$, and $\lambda_0 = nP = 500$ nm, and the film thickness is $25P$. The helix pitch of the defect positioned in the middle of the medium is $P_D = 0.8P$.

spectra. The dynamic theory is inapplicable in the case of a very small film thickness or where the distance within which the amplitude of the incident wave decreases by a factor of e, $l = Pn/\pi\delta n$ (where $\delta n = n_\parallel - n_\perp$ is the birefringence of the quasi-nematic layer, is comparable with the helix pitch).

We assume that the CLC consists of nonequidistant parallel planes separated from one another by a distance equal to the helix pitch varying along the helix axis. In other words, each plane replaces m layers, and the amplitude reflection coefficient of the plane is expressed as [12]

$$r = -iQ = -i\pi\delta n/n. \tag{1}$$

To take into account the effect of multiple reflections from the planes, it is necessary to write the difference equations. Let A_l and B_l be the complex amplitudes of the incident and reflected waves at a point immediately above the nth plane. Then, the difference equations for a cholesteric with a varying helix pitch have the form

$$B_l = -iQA_l + \exp(-i\varphi_l)B_{l+1},$$

$$A_{l+1} = \exp(-i\varphi_l)A_l - iQ\exp(-2i\varphi_l)B_{l+1}, \tag{2}$$

$$l = 0, 1, ..., N-1,$$

where the phase difference φ_l, which arises when light travels the distance between the planes, has the form $\varphi_l = 2\pi nP_l/\lambda$ [12]; here, λ is the light wavelength in vacuum and P_l is the helix pitch corresponding to the lth plane. Note that Eqs. (2) are reduced to the difference equations for a perfect CLC [12] if we ignore the subscript l in the expression for the phase difference φ_l. In deriving Eqs. (2), we assumed that the reflection coefficient is the same on both sides of the plane.

The set of equations (2) can be represented as a matrix equation

$$\begin{pmatrix} B_l \\ A_l \end{pmatrix} = \hat{T}_l \begin{pmatrix} B_{l+1} \\ A_{l+1} \end{pmatrix}, \tag{3}$$

where the transfer matrix has the form

$$\hat{T}_l = \begin{pmatrix} e^{-i\varphi_l} & -iQe^{i\varphi_l} \\ iQe^{-i\varphi_l} & e^{i\varphi_l} \end{pmatrix}. \tag{4}$$

From Eq. (3) it follows that the amplitudes A_0 and B_0 are related to A_N and B_N as follows:

$$\begin{pmatrix} A_0 \\ B_0 \end{pmatrix} = \hat{M} \begin{pmatrix} B_N \\ A_N \end{pmatrix}, \tag{5}$$

where

$$\hat{M} = \hat{T}_0, \hat{T}_1, ..., \hat{T}_{N-1}. \tag{6}$$

The energy reflection coefficient $R(\lambda)$ is determined under the condition that reflection is absent on the right-hand side of the CLC sample:

$$R(\lambda) = \left| \left(\frac{A_0}{B_0} \right)_{B_{N=0}} \right|^2. \tag{7}$$

Using Eq. (5), we obtain

$$R(\lambda) = \left| \frac{M_{12}}{M_{22}} \right|^2, \tag{8}$$

where M_{12} and M_{22} are elements of the matrix $\hat{M}$.

Let us now consider the features of the reflection spectrum of CLC with one and two structural defects by using a numerical solution to the equation for reflection coefficient (8) while varying the parameters of photonic crystal. In what follows, the parameters of the bare structure, which satisfy the conditions of applicability of the dynamic mode, are assumed to be identical to those given in [12] in the study of a perfect CLC film with a thickness of $25P$: $n = 1.5$, $\delta n = 0.07$, and $\lambda_0 = nP = 0.5$ μm.

Figure 1 shows the dependence of the reflection coefficient of the CLC film on the wavelength varying within the region of existence of the band gap for a perfect CLC film and for the case where the helix pitch at the center of the film is smaller than the pitch of the perfect structure and is equal to $0.8P$. The boundaries of the spectral region of the band gap in a perfect cholesteric determine the wavelengths $\lambda_1 = 485$ nm and $\lambda_2 = 515$ nm. The value of the reflection coefficient for the CLC without defects reaches unity in the selective reflection band and decreases with a decrease in both the film thickness and the anisotropy of the cholesteric δn. As is seen from Fig. 1, a dip occurs in the middle of the band gap because of the structural defect, and the width of the band gap in the CLC with the defect proves to be greater than the band gap in the perfect cholesteric. The oscillations of the reflection coefficient
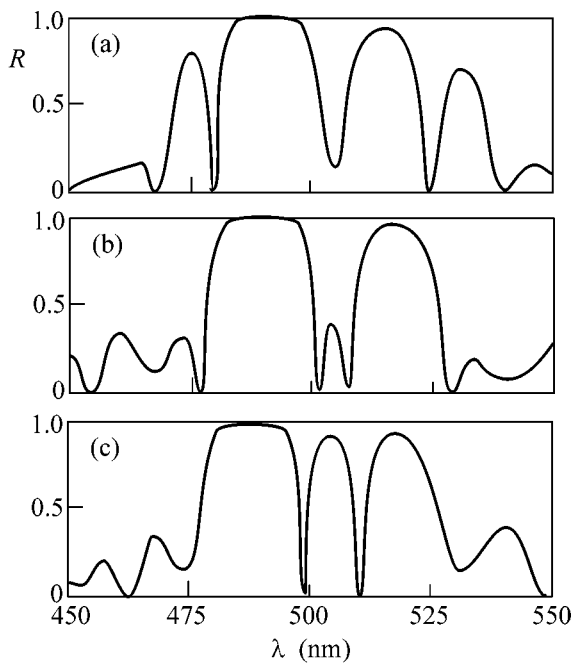
Fig. 2. The dependence of the reflection coefficient on the wavelength at normal incidence of light on the CLC with two identical structural defects. The parameters of the perfect structure are the same as in Fig. 1. The distance between the defects symmetrically positioned with respect to the center of the film is equal to (a) $13P$, (b) $9P$, and (c) $5P$.
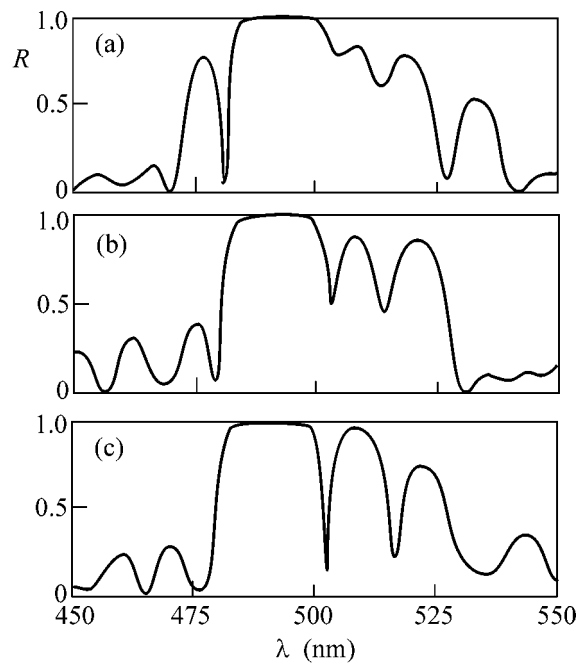
Fig. 3. Dependence of the reflection coefficient on the wavelength at normal incidence of light on the CLC with two different structural defects: $0.8P$ and $0.9P$. The other parameters are the same as in Fig. 2.

observed as the wavelength moves away from the selective reflection region are caused by the light diffraction by a bounded volume, and, for a semibounded space occupied by the cholesteric, such oscillations of the reflection coefficient are absent [12].

The reflection spectrum of a CLC with two identical structural defects is shown in Fig. 2 for different distances between the defects. One can see that, as the distance between the defects increases, or, in other words, as the mutual effect of electromagnetic modes localized at the defects becomes weaker, the reflection spectrum exhibits qualitative changes. In the selective reflection region, two dips induced by the defects merge into one; i.e., a degeneration of the frequencies of electromagnetic modes localized at the defects takes place, and the positions of the boundaries of the spectral region of the band gap change. The oscillations of the reflection coefficient for the wavelengths near the selective reflection region undergo considerable changes (e.g., for wavelengths smaller than 480 nm and greater than 525 nm in Fig. 2a).

Figure 3 shows the reflection spectrum of a CLC with two different defects with a helix pitch of $0.8P$ and a pitch of $0.9P$. The defects are at approximately equal distances from the middle of the film, these distances being the same as in the case of two identical defects (Fig. 2). One can see that the dips observed in the selective reflection band do not merge for the defect separa-

tions reaching $13P$ (Fig. 3a); i.e., no degeneration of the defect-mode frequencies takes place. In addition, as seen from a comparison of Figs. 3b, 3c with Figs. 2b, 2c, the dip depths are smaller for the CLC with different defects. These are the main features that differentiate these spectra from the reflection spectra shown in Fig. 2, which indicate the resonance nature of the mutual influence of the electromagnetic defect modes in a cholesteric with identical defects.

REFERENCES

1. E. Yablonovitch, Phys. Rev. Lett. **58**, 2059 (1987).

2. J. D. Joannopoulos, R. D. Meade, and J. N. Winn, *Photonic Crystals: Molding the Flow of Light* (Princeton Univ. Press, Princeton, N.J., 1995).

3. E. Yablonovitch, T. J. Gmitter, R. D. Meade, *et al.*, Phys. Rev. Lett. **67**, 3380 (1991).

4. S. Ya. Vetrov and A. V. Shabanov, Zh. Éksp. Teor. Fiz. **120**, 1126 (2001) [JETP **93**, 977 (2001)].

5. A. M. Zheltikov, Usp. Fiz. Nauk **172**, 743 (2002) [Phys. Usp. **45**, 687 (2002)].

6. S. O. Konorov, O. A. Kolevatova, A. B. Fedotov, *et al.*, Zh. Éksp. Teor. Fiz. **123**, 975 (2003) [JETP **96**, 857 (2003)].

7. O. Painter, R. K. Lee, A. Scherer, *et al.*, Science **284**, 1819 (1999).

8. V. A. Belyakov and S. A. Sonin, *Optics of Cholesteric Liquid Crystals* (Nauka, Moscow, 1982) [in Russian].

9. Y.-C. Yang, C.-S. Kee, J.-E. Kim, *et al.*, Phys. Rev. E **60**, 6852 (1999).

10. V. I. Kopp and A. Z. Genack, Phys. Rev. Lett. **89**, 033901 (2002).

11. J. Schmidtke, W. Stille, and H. Finkelmann, Phys. Rev. Lett. **90**, 083902 (2003).

12. S. Chandrasekhar, *Liquid Crystals* (Cambridge Univ. Press, Cambridge, 1977; Nauka, Moscow, 1980).

13. S. P. Palto, Zh. Éksp. Teor. Fiz. **119**, 638 (2001) [JETP **92**, 552 (2001)].

Translated by E. Golyamina

Interwell Excitons in a Lateral Potential Well in an Inhomogeneous Electric Field

A. V. Gorbunov* and V. B. Timofeev

Institute of Solid-State Physics, Russian Academy of Sciences, Chernogolovka, Moscow region, 142432 Russia
* e-mail: gorbunov@issp.ac.ru
Received June 28, 2004

The luminescence of interwell excitons in double quantum wells based on GaAs/AlGaAs semiconductor heterostructures (*n–i–n* structures) in a lateral trap prepared with the use of an inhomogeneous electric field was studied at helium temperatures. A rather strong and inhomogeneous electric field occurred in the depth of the heterostructure when a current passed through the contact between the conducting tip of a tunneling microscope and the heterostructure surface to the bulk region containing a built-in gate. Because of the Stark shift of energy bands in the electric field, the photoexcited electrons and holes are spatially separated in neighboring quantum wells by a tunnel-transparent barrier and are bound into interwell quasi-two-dimensional excitons. These excitons have a dipole moment even in the ground state. Therefore, electrostatic forces in the inhomogeneous electric field cause the excitons to move in the plane of quantum wells toward the maximum field region and eventually accumulate in the lateral trap artificially prepared in such a way. The maximum trap depth achieved through the inhomogeneous electric field was 13.5 meV, and its lateral size was about 10 μm. It is shown that, in the traps prepared in this way, photoexcited interwell excitons behave with increasing concentration at sufficiently low temperatures (*T* = 2 K) in the same fashion as in the lateral traps caused by large-scale fluctuations of the random potential. At concentrations exceeding the percolation threshold, the interwell excitons condense into the lowest energy state in the trap. © *2004 MAIK "Nauka/Interperiodica"*.

PACS numbers: 71.35.Cc; 78.67.De

Semiconductor systems with spatially separated electron–hole layers have been attracting great interest for many years and are objects of intensive studies [1–18]. Such objects are, in particular, heterostructures with double tunnel-coupled quantum wells (*p–i–n* and *n–i–n* structures). Upon switching on a sufficiently strong electric field, the energy bands between the quantum wells are shifted. Under these conditions, the photoexcited electrons and holes are spatially separated between the neighboring quantum wells and, because of the Coulomb interaction, are bound into interwell excitons. Such quasi-two-dimensional excitons have a dipole moment and, because of dipole–dipole repulsion, form no stable complexes in the ground state. In the rarefied gas of interwell excitons, their Bose condensation can occur if the exciton density and temperature reach their critical values and the dimensionless parameter $r_s \gg 1$ ($r_s = (\pi N_s a_B^2)^{-1/2}$, where N_s is the density of interwell excitons, and a_B is their Bohr radius). Such condensation was observed in GaAs/AlGaAs heterostructures with double quantum wells (DQWs) given large-scale fluctuations of the random potential (at exciton densities on the order of 10^{10} cm^{-2}, $r_s \approx 5$) [15]. In fact, such fluctuations create a large-scale potential relief in the plane of quantum wells and lateral traps for interwell excitons related to this relief. The number of states in the lateral traps is finite, and, what

is most important, excitons in such traps can be accumulated more easily [7]. Therefore, it is in the lateral traps that the critical conditions corresponding to the Bose condensation of interwell excitons are simpler to accomplish. Work with single domains (traps) was carried out using a metal mask on a heterostructure surface containing micron-sized windows, through which interwell excitons were excited by light and their luminescence was detected [15]. The Bose condensation of interwell excitons was accompanied by the threshold-like appearance of a very narrow luminescence line corresponding to the radiative decay of interwell excitons. In the temperature range studied (1–4 K), the luminescence line intensity associated with the Bose condensate of excitons at a fixed density linearly decreased with increasing temperature. The critical temperature T_c almost linearly increased with increasing exciton density in accordance with the current concepts of Bose condensation in two-dimensional systems with lateral confinement, namely,

$$T_c \approx 2\pi\hbar^2 N_s / g_{ex} k_B m_{ex} \ln(N_s S),$$

where S is the domain (trap) area, g_{ex} is the spin degeneracy factor of excitons, and m_{ex} is the translational exciton mass in the plane.

In the case of lateral traps caused by large-scale fluctuations of the random potential, the question of the
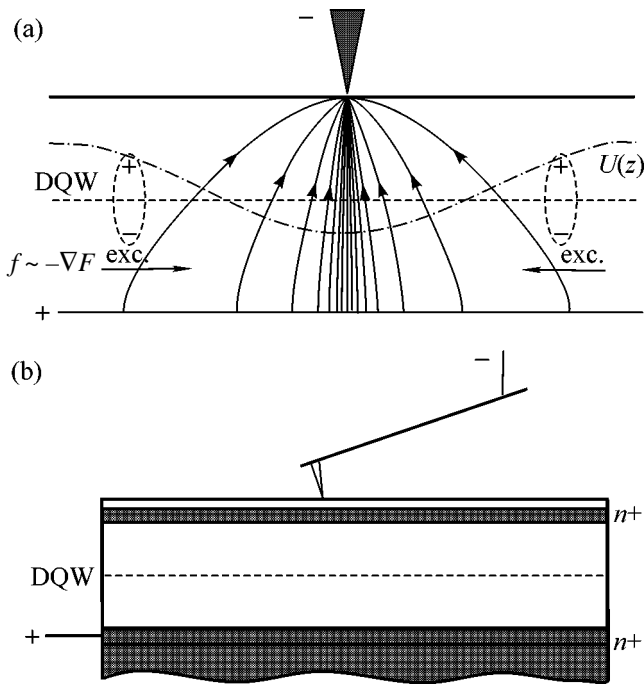
Fig. 1. Experimental setup. (a) Schematic diagram of an inhomogeneous electric field in the structure with an electrical current passing through the point contact (lines with arrows are electric field lines near the tip; the dash-dotted line shows the potential well for interwell excitons due to the inhomogeneous electric field; the dashed straight line is the section of the DQW); in an inhomogeneous electric field, the electrostatic forces cause the interwell excitons (dipoles) to move toward the center of the potential well. (b) Qualitative scheme of the sequence of layers in the heterostructure and the cantilever tip contact with its surface.

shape of the potential well, its actual depth, and the lateral size remains open. In this connection, the artificial preparation of lateral traps with the use of an external action when the parameters of the potential trap could be specified and controlled with greater definiteness becomes an important task. The use of an inhomogeneous electric field could be the most appropriate solution to this problem. The action of an inhomogeneous electric field on interwell excitons is schematically illustrated in Fig. 1a. Imagine that, under conditions of point contact between the tip of a tunneling microscope and the surface of a DQW-containing heterostructure, an electrical current is triggered into the structure bulk under an applied electrical bias between the conducting tip and the back gate built in the structure. The electric field inside the structure will be strongly inhomogeneous (electric field lines are shown schematically in Fig. 1a). The electric field shifts the size-quantization levels in the tunnel-coupled quantum wells and causes the spatial separation of photoexcited electrons and holes between the neighboring quantum wells. The largest shift of the energy bands between the neighboring quantum wells will be in the region where the formed field is a maximum under conditions when a

current passes through the structure. It is natural to expect that the field will reach a maximum directly under the tip. The electric field in the plane of quantum wells is strongly inhomogeneous: the field is very weak at large distances from the contact and is a maximum in the vicinity of the contact (see Fig. 1a). In the plane of quantum wells, such a field can create a rather deep potential well for interwell excitons. The depth of the lateral potential well in this case is $\Delta U = -eF_{max}d$, where d is the distance between the DQWs, and F_{max} is the maximum field at the center of the well. The magnitude of the electric field can be monitored experimentally by the spectral shift of the luminescence line of interwell excitons with respect to the luminescence of intrawell excitons. Recall that, for the interwell excitons to be observed, the Stark shift of the energy bands must exceed the difference between the binding energies of the intrawell (direct) and interwell excitons $eFd \geq E_D - E_I$. The minimum expected lateral size of the trap can be estimated. This size must be at least no less than the distance between the contact of the tip with the structure surface and the built-in gate (it is assumed that the size of the contact itself is much smaller than this distance). The real size of the potential well will be determined by the conditions for current passage in the structure.

Moreover, the interwell excitons are dipoles even in the ground state; therefore, such excitons in an inhomogeneous field will experience electrostatic forces ($f \sim -e\nabla F$) that cause the excitons to move toward the center of the potential well, which serves as a trap for interwell excitons. The distance at which the excitons can drift is determined by the field gradient, the exciton lifetime, and exciton mobility. The dash-dotted line in Fig. 1a shows the form of the potential well qualitatively. The two-dimensional interwell excitons can move freely only in the DQW plane (the corresponding section in Fig. 1a is shown by a dashed line).

Work was carried out with n–i–n GaAs/AlGaAs heterostructures with a double GaAs/AlAs quantum well. The GaAs quantum wells were 120 Å in width and separated by a narrow AlAs barrier 11 Å in width. The heterostructure was grown by molecular beam epitaxy on a doped n-type GaAs substrate having the (001) crystallographic orientation (the concentration of the donor impurity of Si atoms in the substrate was 2×10^{18} cm^{-3}). First, a doped buffer n-GaAs layer about 0.5 μm in thickness was grown on the substrate. Next was an insulating $Al_xGa_{1-x}As$ ($x = 0.35$) layer 120 nm thick containing ten periods of the $AlAs/Al_xGa_{1-x}As$ superlattice ($x = 0.35$, the superlattice period was 3 nm), followed by the GaAs/AlAs/GaAs DQW. After it, an insulating $Al_xGa_{1-x}As$ ($x = 0.35$) layer 120 nm thick containing ten periods of the $AlAs/Al_xGa_{1-x}As$ superlattice ($x = 0.35$, the superlattice period was 3 nm) was grown again. Narrow AlAs barriers (the AlAs barrier width was 11 Å) were located between the GaAs quantum wells and the insulating regions. The last in the upper

part of the structure was a silicon-doped GaAs layer (the layer thickness was about 100 nm, and the silicon concentration was 2×10^{18} cm^{-3}), which was covered with an insulating layer of undoped GaAs 10 nm thick (so-called cap layer). A contact region to the doped buffer n layer, which served as the built-in back gate, was etched on the structure by photolithography. Next, contacts to the buffer layer and to the doped layer were mounted in the upper part of the mesa.

The inhomogeneous electric field inside the heterostructure was created using the tip of the tunneling microscope (shown schematically in Fig. 1b). For this purpose, a commercial silicon cantilever of the tunneling microscope was used with the following parameters of the tip: the shape was a tetrahedral pyramid with a height-to-base ratio of 3 : 1, the height was no less than 7 μm, and the typical radius of curvature of the tip end was about 10 nm. The cantilever with the tip covered with a gold film about 20 nm in thickness was mounted on a coupled pair of bimorph piezoelectric ceramic plates. The design allowed soft contact of the tip with the structure surface to be accomplished when an electric voltage was applied across the piezoelectric ceramic plates. All the construction together with the heterostructure was housed inside an optical cryostat in superfluid helium. The contact of the cantilever tip with the heterostructure surface was monitored by direct observation in an optical microscope and also by the deflection of the probe laser beam. Upon the contact of the tip with the structure surface, when an electric voltage was applied between the built-in back gate and the cantilever, a current started to pass across the structure.

Photoexcitation was performed using a He–Ne laser focused on the sample surface onto a spot of size less than 30 μm. The spectra were analyzed using a double monochromator and were detected by a multichannel CCD detector cooled by liquid nitrogen.

Figure 2a demonstrates the behavior of the luminescence spectra upon variation of the electrical bias between the doped upper and buffer flat n-layers under photoexcitation by a He–Ne laser. In the absence of an electrical bias, only the luminescence band of intrawell heavy-hole excitons is present in the spectrum (1sHH exciton state). The doublet structure is associated with the localized (long-wavelength component) and free (short-wavelength component) intrawell excitons. At voltages $V \le -0.4$ V, the luminescence line of interwell excitons appears in the spectra on the side of lower energies. As the voltage increases, this line moves toward lower energies in proportion to the bias, in accordance with the linear Stark shift of size-quantization levels, and becomes dominant in the spectra. In this case, the intensity of the luminescence line of intrawell excitons decreases by several orders of magnitude as compared with the intensity of the interwell exciton line. When the focused photoexcitation was displaced within the mesa (the mesa size was 1.5×1.5 mm^2) at a fixed applied voltage, the spectral shift of the luminescence line of interwell excitons and the line width remained unchanged to a high accuracy. This fact points to a rather high homogeneity of the electric field between the doped upper and buffer flat layers.
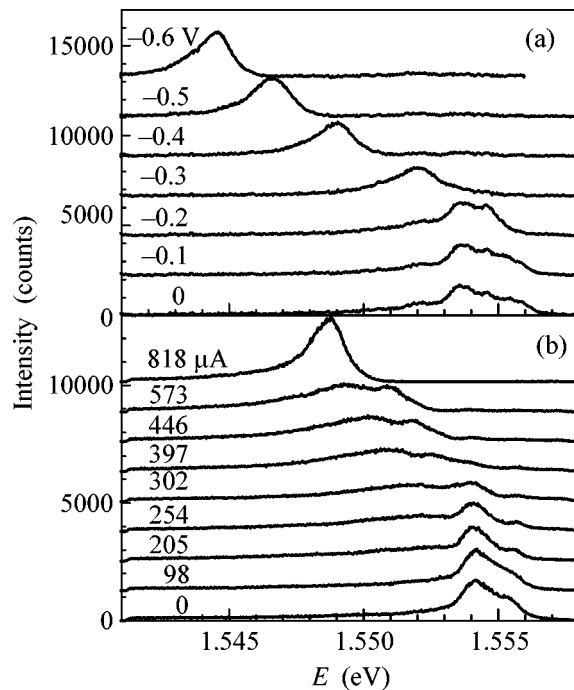

Fig. 2. Luminescence of interwell and intrawell excitons. (a) Spectra measured at different voltages applied between the upper and buffer flat doped layers. (b) Spectra measured under voltage applied between the cantilever tip and the buffer gate at various magnitudes of the current passing through the structure (photoexcitation by a He–Ne laser beam focused onto a spot no less than 30 μm in the contact region). The luminescence is detected directly from the excitation region. The power in the beam is 5 μW, $T = 2$ K.

A different situation arises when, under conditions of cantilever-tip contact with the heterostructure surface, an electric voltage is applied between the tip and the doped buffer layer (back gate in Fig. 1b). Figure 2b illustrates the behavior of the luminescence spectra upon variation of the current passing through the structure when photoexcitation is focused into a spot less than 30 μm in size directly in the region of tip contact with the surface. In the absence of current, only the luminescence of intrawell excitons is observed in the spectrum. Upon switching on the voltage, a current started to pass through the structure. This current increased with increasing applied voltage; however, the corresponding current–voltage characteristic was not linear. As the current increased, the luminescence of intrawell excitons decreased and the luminescence band of interwell excitons started to appear on the side of lower energies. The intensity of this line increased with increasing current. The magnitude of the spectral shift with respect to the line of intrawell excitons increased with increasing current. With a weak current
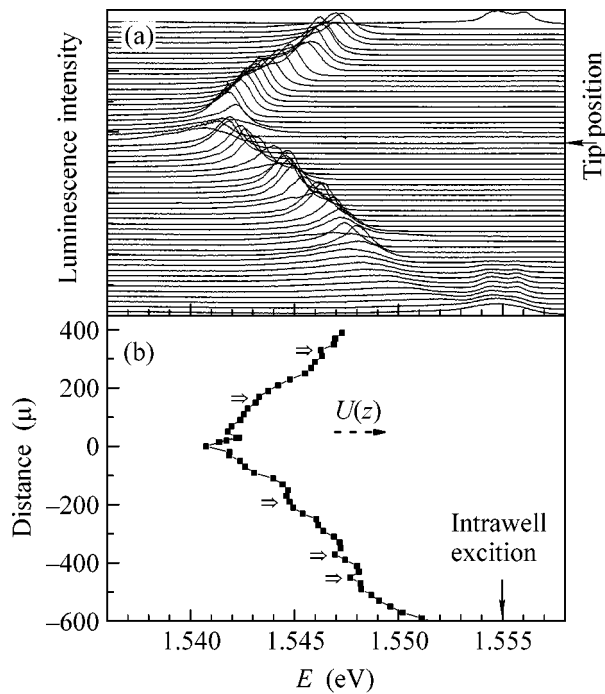
Fig. 3. Experimental profile of the potential well generated by an inhomogeneous electric field. (a) Luminescence spectra of interwell and intrawell excitons measured as a function of the distance between the photoexcitation spot and the point contact (the luminescence is detected only from the excitation region). (b) Position of the luminescence line maximum of interwell excitons as a function of the same distance. The current through the contact is ≈27 μA, the voltage is 4.9 V, the power in the beam is 3 μW, and $T = 2$ K.

through the structure, the luminescence band of interwell excitons was broad. As the current increased, the corresponding potential well became deeper and the luminescence line significantly shifted toward lower energies. At a voltage in the range 0.1–10 V, this evolution of spectra was observed at strongly different magnitudes of the current through the contact (from tens of nA to hundreds of μA), depending apparently on the contact conditions. The luminescence line of interwell excitons disappeared if the laser spot exciting the luminescence moved from the contact (the luminescence at such displacements was detected directly from the photoexcitation region). At such displacements, simultaneously with the disappearance of the line of interwell excitons, the line of intrawell excitons appeared. This behavior at displacements of the laser spot was close to axially symmetric. These experiments demonstrate that, a lateral potential well in which interwell excitons can accumulate arises in the vicinity of the tip contact with the heterostructure surface when a current passes through the heterostructure.

Consider now the shape the potential well takes as current passes through the structure. For this purpose, the luminescence spectra of excitons were measured as a function of the position that the sharply focused laser spot exciting the luminescence occupies with respect to

the point contact (see Fig. 3). In these measurements, the luminescence was detected directly from the region of the exciting laser spot. This region was singled out by special diaphragms in the intermediate image plane and was projected onto the entrance slit of the spectrometer. Figure 3a demonstrates the behavior of the luminescence spectra of interwell and intrawell (direct) excitons upon variation of the distance from the point contact. Figure 3b displays the behavior of the spectral position of the line maximum of interwell excitons as a function of the same distance. In fact, this figure reproduces the shape of the lateral potential well for interwell excitons: $U(x) = eF(x)d + E_I(x)$. First of all, it is seen that the largest spectral shift of the luminescence line of interwell excitons with respect to the line of intrawell excitons is observed directly in the point-contact region. At this place, the well is deepest and the spectral shift is 13.5 meV when the current through the structure is 27 μA. From the value of this shift, one can easily estimate the maximum value of the electric field, which in this case equals 1.1×10^4 V/cm. As the distance from the point-contact region increases, the electric field decreases and the line of intrawell excitons appears at distances larger than 500 μm. Under these conditions, the luminescence line of interwell excitons is weakly shifted on the energy scale and its intensity is suppressed. The pattern of the field distribution around the point contact is close to axially symmetric. However, the radial distribution of the electric potential itself is not a monotonic function of the distance from the contact. First, a narrow and rather deep dip in the potential well is observed in the immediate vicinity of the contact. The most striking and unexpected finding was the fact that such narrow and rather deep dips in the potential curve are observed at large distances from the center of the well (shown by wide arrows in Fig. 3b). These narrow dips are observed, as a rule, at current magnitudes higher than 1 μA, and their distance from the center of the well increases with increasing current magnitude. The origin of these dips in the potential curve is a separate, yet unsolved problem. The possible reason for their appearance is associated with the nonlinear screening of the electric field inside the structure by photoexcited carriers. However, it is evident that the narrow dips in the potential curve can, in principle, themselves serve as lateral traps for interwell excitons.

Of interest is the behavior of the luminescence of interwell excitons under laser excitation focused directly onto such traps (Fig. 4). In the case of the central trap located directly below the point contact, the luminescence line of interwell excitons is always broad (the width is about 3 meV or larger). This is connected with the strong overheating of the near-contact region, where the current density is maximum. In this connection, of great interest are the regions of dips in the potential curve far away from the contact site, where overheating can be neglected. These regions are also potential traps for interwell excitons. Consider the luminescence of excitons under excitation into such a
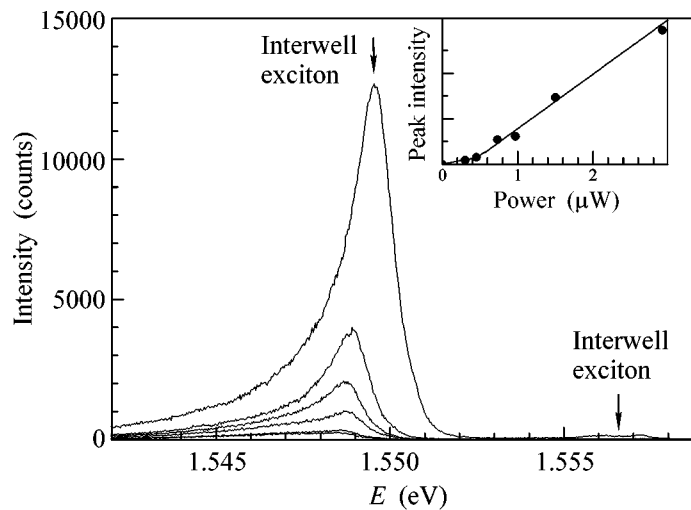
Fig. 4. Luminescence spectra of interwell excitons upon variation of the photoexcitation power. The spectra were measured directly from the potential well (trap) generated by the inhomogeneous electric field and separated from the center of the well by ≈80 μm. The current through the contact ≈820 μA, the voltage is 0.41 V, $T = 2$ K.

trap remote from the center. At low pumping less than 300 nW, a broad asymmetric luminescence band (with a band width of about 3 meV) is observed in the spectrum. Its long-wavelength tail smoothly decreases in intensity. The shape of this band remains unchanged upon variation of the excitation power below 300 nW. This band is inhomogeneously broadened and originates from the radiative decay of strongly localized interwell excitons. Their localization is connected with short-period fluctuations of the random potential generated by charged centers in the vicinity of the DQW. At pumping higher than 300 nW, a rather narrow line of delocalized interwell excitons 1 meV in width arises in a threshold way on the violet side of the asymmetric structureless band. The intensity of this line near the threshold increases superlinearly relative to the structureless background under it. Only at high pumping (>3 μW), the luminescence line of interwell excitons starts to broaden and to shift toward high energies because of the screening of the electric field. The behavior of the spectra of interwell excitons in a lateral trap turns out to be qualitatively similar to that exhibited by interwell excitons upon condensation into the lowest state in a lateral domain (trap) due to large-scale fluctuations of the random potential.

REFERENCES

1. Yu. E. Lozovik and V. I. Yudson, JETP Lett. **22**, 274 (1975).

2. D. Yoshioka and A. H. MacDonald, J. Phys. Soc. Jpn. **59**, 4211 (1990).

3. X. M. Chen and J. J. Quinn, Phys. Rev. Lett. **67**, 895 (1991).

4. T. Fukuzawa, E. E. Mendez, and J. M. Hong, Phys. Rev. Lett. **64**, 3066 (1990).

5. J. E. Golub, K. Kash, J. P. Harbison, and L. T. Flores, Phys. Rev. B **41**, 8564 (1990).

6. L. V. Butov, A. Zrenner, G. A. Abstreiter, *et al.*, Phys. Rev. Lett. **73**, 304 (1994); L. V. Butov, in *Proceedings of the 23rd International Conference on Physics of Semiconductors* (Berlin, 1996).

7. Xuejun Zhu, P. L. Littlewood, M. S. Hybersten, and T. Rice, Phys. Rev. Lett. **74**, 1633 (1995).

8. V. B. Timofeev, A. V. Larionov, A. S. Ioselevich, *et al.*, JETP Lett. **67**, 613 (1998).

9. J. F. Jan and Y. C. Lee, Phys. Rev. Lett. **58**, R1714 (1998).

10. V. V. Krivolapchuk, E. S. Moskalenko, A. L. Zhmodikov, *et al.*, Solid State Commun. **111**, 49 (1999).

11. L. V. Butov, A. Imamoglu, A. V. Mintsev, *et al.*, Phys. Rev. B **59**, 1625 (1999).

12. A. V. Larionov, V. B. Timofeev, J. M. Hvam, *et al.*, JETP **90**, 1093 (2000).

13. L. V. Butov, A. V. Mintsev, Yu. E. Lozovik, *et al.*, Phys. Rev. B **62**, 1548 (2000).

14. A. V. Larionov, V. B. Timofeev, J. M. Hvam, *et al.*, JETP Lett. **75**, 200 (2002).

15. A. V. Larionov, V. B. Timofeev, P. A. Ni, *et al.*, JETP Lett. **75**, 570 (2002).

16. J. Fernandez-Rossier and C. Tejedor, Phys. Rev. Lett. **78**, 4809 (1997).

17. Yu. E. Lozovik and O. L. Berman, JETP **84**, 1027 (1997).

18. Yu. E. Lozovik and I. V. Ovchinnikov, JETP Lett. **74**, 288 (2001).

Translated by A. Bagatur'yants

Magnetic Resonance of Cu and of Gd in Insulating $GdSr_2Cu_2NbO_8$ and in Superconducting $GdSr_2Cu_2RuO_8$[¶]

J. D. Dow[1, *], H. A. Blackstead[2], Z. F. Ren[3], and D. Z. Wang[3]

[1] *Department of Physics, Arizona State University, Tempe, Arizona 85287-1504, USA*
* e-mail: catsc@cox.net
[2] *Department of Physics, University of Notre Dame, Notre Dame, Indiana 46556, USA*
[3] *Physics Department, Boston College, Chestnut Hill, MA 02167, USA*
Received July 5, 2004

Weak-ferromagnetic (or antiferromagnetic) resonance of Cu and electron spin resonance (ESR) of Gd are observed both in insulating $GdSr_2Cu_2NbO_8$ and in superconducting $GdSr_2Cu_2RuO_8$. The Cu resonance implies that the CuO_2 planes are magnetic and indicates that the superconducting layer of $GdSr_2Cu_2RuO_8$ is SrO (not CuO_2), as in its related superconducting compound without cuprate planes, doped Sr_2YRuO_6. © *2004 MAIK "Nauka/Interperiodica".*

PACS numbers: 76.50.+g; 76.30.Kg; 74.25.Nf; 74.72.Jt

1. INTRODUCTION

$GdSr_2Cu_2NbO_8$ is an especially interesting material because it is an insulator that does *not* superconduct, although a compound of similar structure exhibits high-temperature superconductivity, $GdSr_2Cu_2RuO_8$ [1–7]. In an attempt to determine which facts about electronic structure are essential to high-temperature superconductivity, we compare magnetic resonance measurements of superconducting $GdSr_2Cu_2RuO_8$ with similar measurements of nonsuperconducting $GdSr_2Cu_2NbO_8$.

One might have expected $GdSr_2Cu_2NbO_8$ and $GdSr_2Cu_2RuO_8$ to behave the same, because both materials have essentially the same crystal structure (Fig. 1) and differ only in that the Ru ion, which is primarily in the Ru^{+5} charge-state, replaces Nb^{+5} [4]. (The Mössbauer data indicate that a minority of the Ru ions may be in the Ru^{+4} charge state [6].) However, $GdSr_2Cu_2NbO_8$ does not superconduct and is a charge-balanced insulator, although $GdSr_2Cu_2RuO_8$ does superconduct, with an onset transition temperature for superconductivity of order 45 K. (See Figs. 2 and 3 and compare them with Fig. 2 of [6].) This difference between Nb and Ru materials appears to be attributable completely to the different electronic bands and their electron occupations in the two materials. Nb^{+5} has completely filled 4*s* and 4*p* shells (and an empty 4*d* shell), and Ru^{+5} has three 4*d* electrons outside its full 4*s* and 4*p* shells. (Ru^{+4} has four 4*d* electrons outside its 4*s* and 4*p* shells.) Clearly, the electronic structures of the Nb and Ru ions must play important roles in determin-

ing why $GdSr_2Cu_2NbO_8$ does not superconduct, while $GdSr_2Cu_2RuO_8$ does superconduct.

2. NB BANDS ARE OCCUPIED

We propose that the reason for the difference between $GdSr_2Cu_2RuO_8$, on the one hand, and $GdSr_2Cu_2NbO_8$, on the other, is that the Ru bands are
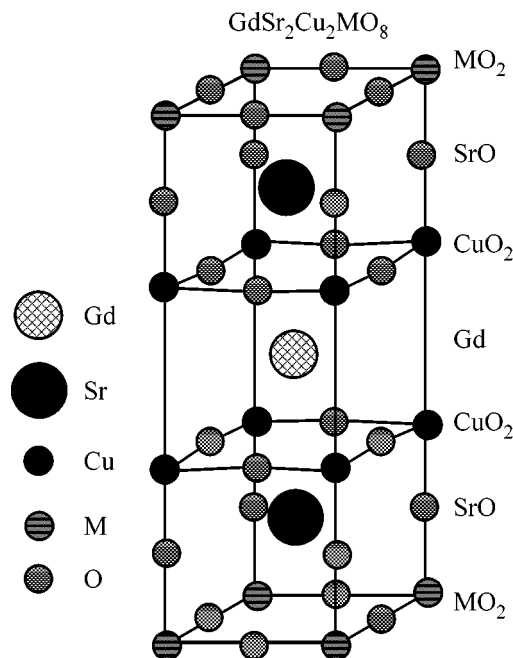

Fig. 1. Crystal structure of $GdSr_2Cu_2MO_8$ for M = Ru or Nb.

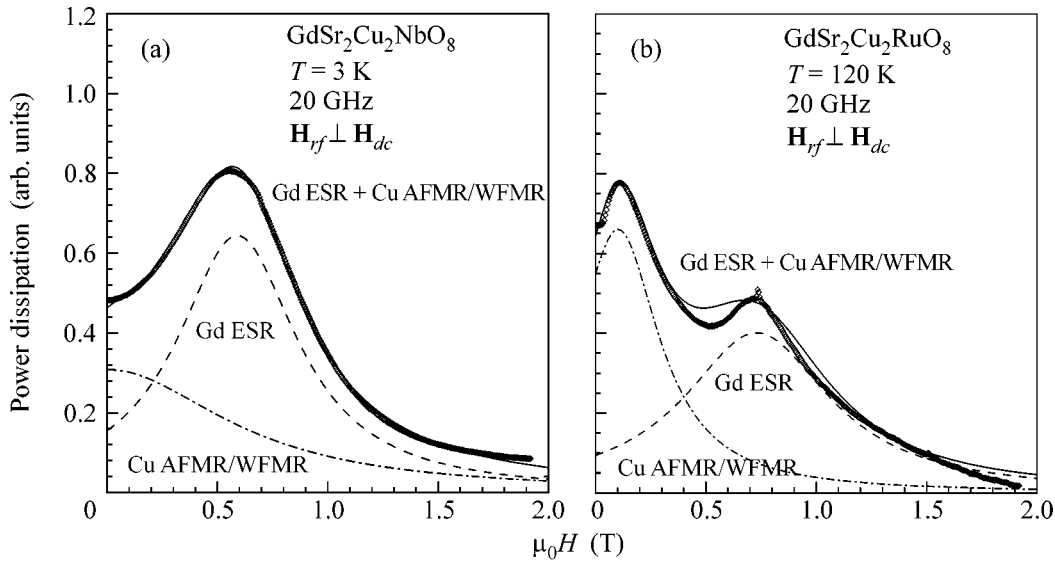
[¶] This article was submitted by the authors in English.

Fig. 2. Power dissipation (in arbitrary units) (a) in $GdSr_2Cu_2NbO_8$ and (b) in $GdSr_2Cu_2RuO_8$ vs. applied magnetic field μ_0H in Tesla for $\mathbf{H}_{rf} \perp \mathbf{H}_{dc}$. The data are the heavy line. The dashed curve, which shows the electron spin resonance of Gd, and the dashed-dotted curve, which shows the Cu weak-ferromagnetic resonance (or antiferromagnetic resonance), add up to the composite fit (thin solid line). The data were taken at 20 GHz and at a temperature of 3 K for $GdSr_2Cu_2NbO_8$ and 120 K (well above T_c) for $GdSr_2Cu_2RuO_8$. We attribute the broad low-field signals to Cu; one of these, for $GdSr_2Cu_2RuO_8$, has been assigned to Ru by other authors [2].

broader and partially filled with electrons, while the corresponding Nb bands are narrower, are fully occupied, and lie completely below the Fermi surface.

3. Gd ESR AND Cu WFMR OR AFMR

The measurements discussed below were all performed with a custom spectrometer which has the following three features: (i) the applied magnetic field $\mathbf{H}_{dc}$ (also denoted $\mathbf{H}$) can be rotated to be either parallel or perpendicular to the *rf* field $\mathbf{H}_{rf}$ in the microwave cavity; (ii) the spectrometer does not utilize field modulation, and so direct dissipation rather than its derivative is measured; (iii) the microwave cavity resonates in a TE_{101} mode, and for these experiments, the sample is at the bottom-center of the cavity.

Electron spin resonance (ESR) of Gd produces a $g = 2$ spectral peak in both $GdSr_2Cu_2NbO_8$ and in $GdSr_2Cu_2RuO_8$ for $\mathbf{H}_{rf} \perp \mathbf{H}_{dc}$ (dashed lines of Fig. 2), but not for $\mathbf{H}_{rf} \parallel \mathbf{H}_{dc}$ because of the ESR selection rules.

Nonsuperconducting $GdSr_2Cu_2NbO_8$ and superconducting $GdSr_2Cu_2RuO_8$ both also exhibit two weak-ferromagnetic resonances (WFMR) or antiferromagnetic resonances (AFMR) at low fields $\mathbf{H}_{dc}$ (both for $\mathbf{H}_{rf} \perp \mathbf{H}_{dc}$ and for $\mathbf{H}_{rf} \parallel \mathbf{H}_{dc}$ [8]), as shown in Figs. 2 and 3. The magnon energy gaps at $\mathbf{H}_{dc} = 0$ may exceed the microwave photon energies $\hbar\omega$, in which case we see only the "tails" of the resonant modes (see Fig. 3b). These weak-ferromagnetic (or antiferromagnetic) resonance features are prominent and similar in $GdSr_2Cu_2NbO_8$ and

in $GdSr_2Cu_2RuO_8$, but our method of measurement does not determine whether the modes are WFMR or AFMR.

For $GdSr_2Cu_2NbO_8$, we assign the low-field weak-ferromagnetic (or antiferromagnetic) resonance modes to Cu, because nonmagnetic Nb (being Nb^{+5}) and nonmagnetic Sr cannot resonate, leaving Cu as the only possible choice. (The separation of the signals in Fig. 2 was accomplished by nonlinear least squares fitting of two Lorentzian lineshapes to the data. In Fig. 3, only one Lorentzian was employed.)

For $GdSr_2Cu_2RuO_8$, similar data for the weak-ferromagnetic (or antiferromagnetic) modes are given in Figs. 2b (dashed-dotted line) and 3b (thin solid line) for a temperature (120 K) well above the superconducting transition temperature. We also attribute the broad low-field lines to Cu weak-ferromagnetism (or antiferromagnetism) due to their similarity to the data from the $GdSr_2Cu_2NbO_8$ sample and the fact that no resonance signal of any kind has been detected in several materials with either Ru^{+5} or Ru^{+4}. Fainstein *et al.* [2] have observed resonances at 142 and 143 K, more than 9 K above the Ru transition temperature (133 K), and we have seen such resonances at several temperatures up to 180 K. These observations rule out Ru as the source, leaving only Cu as a candidate for the observed resonances.

The Cu signals are robust: the integrated intensities for both $GdSr_2Cu_2RuO_8$ and $GdSr_2Cu_2NbO_8$ with parallel *rf* and *dc* fields in Fig. 3 exceed those of the paramagnetic Gd in perpendicular *rf* and *dc* fields (Fig. 2).
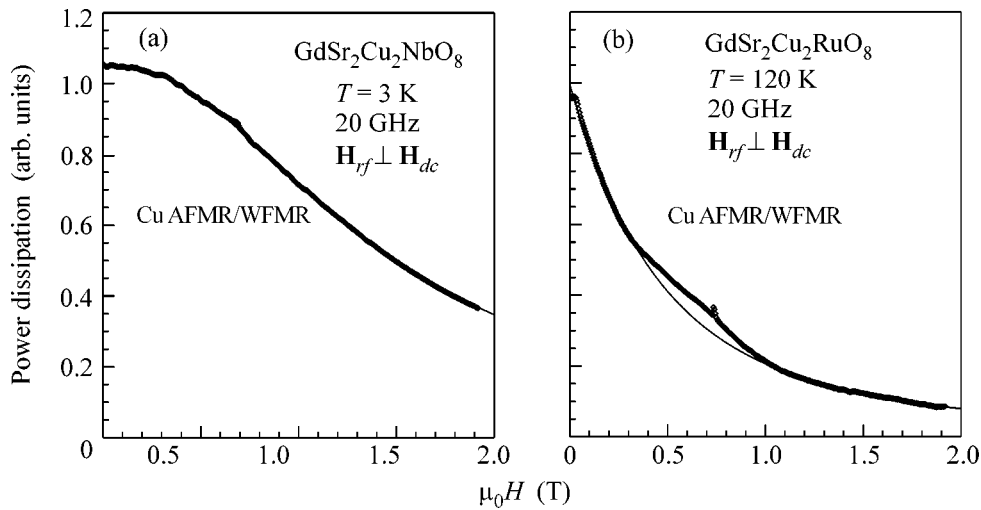
Fig. 3. The power dissipation (in arbitrary units) of (a) GdSr$_2$Cu$_2$NbO$_8$ and (b) GdSr$_2$Cu$_2$RuO$_8$ vs. applied magnetic field $\mu_0 H$ in Tesla for the radio frequency field parallel to the *dc* field, $\mathbf{H}_{rf} \parallel \mathbf{H}_{dc}$. The data and the Lorentzian fits are given by the heavy and the solid lines. The microwave frequency is 20 GHz, and the temperature is 3 K for GdSr$_2$Cu$_2$NbO$_8$ and 120 K for GdSr$_2$Cu$_2$RuO$_8$ (above the superconducting transition temperature). The weak broad feature near 0.7 T is due to Gd moments which evidently see a net field that is not precisely parallel to the applied field. The Cu signals observed in this configuration are more intense than the corresponding Gd ESR signals (Fig. 2).

In Fig. 3b, there is evidence that the Gd moments "see" a local field which is not precisely parallel to the applied field. The composite fits to the data of Figs. 2 and 3 are denoted by thin solid lines and are in good general agreement with the data.

The authors of [2] have evidently assigned the low-field resonance of Fig. 2b incorrectly to *ferromagnetic* Ru. Other evidence supporting the assignment of our "Cu resonance" in GdSr$_2$Cu$_2$RuO$_8$ to Cu rather than to Ru is given by YBa$_2$Cu$_3$O$_7$ data [9, 11, 12]: When Co is partially substituted for Cu in the chains of YBa$_2$Cu$_3$O$_7$, it causes the cuprate planes to order magnetically. The same effect may be expected to occur (and does) when YBa$_2$Cu$_3$O$_7$ is transmuted first to hypothetical GdSr$_2$Cu$_3$O$_7$ and then to GdSr$_2$Cu$_2$RuO$_8$ by replacing all of its CuO chains with magnetic RuO$_2$ layers. Ru in GdSr$_2$Cu$_2$RuO$_8$ orders at ≈ 133 K, and the cuprate planes order at an even higher temperature (>180 K).

We have other data which support the assignment of the weak-ferromagnetic (or antiferromagnetic) resonances in GdSr$_2$Cu$_2$RuO$_8$ to Cu rather than to Ru: one compound, PrSr$_2$Cu$_2$TaO$_8$ (which does not superconduct), but which exhibits resonances apparently due to Cu, features the same resonances we assign to Cu in GdSr$_2$Cu$_2$NbO$_8$ (neither material superconducts).

4. Cu RESONANCES IN SIMILAR MATERIALS

Additional evidence for the $\mathbf{H}_{dc} \parallel \mathbf{H}_{rf}$ resonance being associated with Cu comes from (a) the closely related compounds (rare-earth)$_{2-z}$Ce$_z$Sr$_2$Cu$_2$RuO$_{10}$, (b) a comparison of GdSr$_2$Cu$_2$RuO$_8$ with SrRuO$_3$, and

(c) Ba$_2$GdRuO$_6$, either undoped or doped with Cu on Ru sites.

4a. Gd$_{2-z}$Ce$_z$Sr$_2$Cu$_2$RuO$_{10}$. Gd$_{2-z}$Ce$_z$Sr$_2$Cu$_2$RuO$_{10}$ and Eu$_{2-z}$Ce$_z$Sr$_2$Cu$_2$RuO$_{10}$ both begin superconducting around ~45 K and also have resonances similar to the one we have identified as associated with Cu in GdSr$_2$Cu$_2$RuO$_8$. Gd$_{2-z}$Ce$_z$Sr$_2$Cu$_2$RuO$_{10}$ has the same layers as GdSr$_2$Cu$_2$RuO$_8$ plus two Gd$_{1-z/2}$Ce$_{z/2}$ layers and one O$_2$ layer (the three of which replace one Gd layer between two staggered half-cells of GdSr$_2$Cu$_2$RuO$_8$). The three layers of this Gd$_{2-z}$Ce$_z$O$_2$ partial structure (which is additional to half of GdSr$_2$Cu$_2$RuO$_8$ minus Gd) should not superconduct, because (i) the O$_2$ oxygen ions are too close to the Gd (and so should have any Cooper pairs associated with them broken by the Gd) and (ii) neither Gd$_{2-z}$Ce$_z$CuO$_4$ itself nor the combination of O$_2$, two Gd$_{1-z/2}$Ce$_{z/2}$ layers, and the adjacent cuprate plane superconducts (because Gd$_{2-z}$Ce$_z$CuO$_4$ does not superconduct). Consequently, the superconducting layers in Gd$_{2-z}$Ce$_z$Sr$_2$Cu$_2$RuO$_{10}$ are undoubtedly the same layers as those that superconduct in GdSr$_2$Cu$_2$RuO$_8$ (the SrO layers).

4b. Comparison of GdSr$_2$Cu$_2$RuO$_8$ with SrRuO$_3$. It is instructive to compare GdSr$_2$Cu$_2$RuO$_8$ with SrRuO$_3$, a nonsuperconducting ferromagnet which orders magnetically near 160 K and exhibits no radio frequency response whatsoever at the frequencies employed in our measurements. This is pertinent because the sequence of layers /SrO/RuO$_2$/SrO/ of SrRuO$_3$ is precisely the stacking sequence found in

superconducting $GdSr_2Cu_2RuO_8$. The small difference in the magnetic ordering temperatures of $GdSr_2Cu_2RuO_8$ (133 K) and $SrRuO_3$ (160 K) indicates a significant similarity of the magnetic properties of the two compounds. Hence, the lack of a magnetic resonance in $SrRuO_3$ implies that the observed resonances in $GdSr_2Cu_2RuO_8$ and $Gd_{2-z}Ce_zSr_2Cu_2RuO_{10}$ are due to Cu, rather than due instead to Ru.

4c. Ba_2GdRuO_6 undoped and doped with Cu. Ba_2GdRuO_6, whether doped with Cu or not [10], does not superconduct, although its homologous compound without pair-breaking Gd, Sr_2YRuO_6, does superconduct beginning at ~49 K [6, 10, 13–15] when doped with Cu. (With decreasing temperature, the superconductivity of Cu-doped Sr_2YRuO_6 becomes complete at ~23 K.) Ba_2GdRuO_6 exhibits a $g = 2$ exchange-narrowed paramagnetic Gd resonance over a wide range of temperatures, from room temperature down to the ~48 K Ru-ordering temperature.

Cu doping of Ba_2GdRuO_6 results in an additional weak-ferromagnetic (or antiferromagnetic) low-field resonance, detectable from below the ~86 K Cu-ordering temperature to the lowest temperatures [10]. Clearly, this low-field resonance is associated with Cu. No Ru resonance was detected.

Hence, the only reasonable interpretation of these many facts is that Cu, not Ru, is responsible for the observed low-field weak-ferromagnetic resonance (or antiferromagnetic resonance) in $GdSr_2Cu_2RuO_8$.

5. SUMMARY

Therefore, the two materials, $GdSr_2Cu_2MO_8$, with M = Ru and with M = Nb, (i) each exhibit two modes of Cu weak-ferromagnetic resonance (or antiferromagnetic resonance); (ii) each show a strong Gd electron spin resonance; and (iii) each exhibit a charge of approximately +5 on the ion M, which is not itself the determining factor for why one material superconducts and the other does not. Thus, the three or four outer-shell electrons of Ru play a decisive role in determining the electronic structure and metallic character of the superconducting material.

$GdSr_2Cu_2RuO_8$ has four chemical layers that are candidates for superconductivity: (i) RuO_2, (ii) Gd, (iii) CuO_2, and (iv) SrO. (i) The RuO_2 layer can be eliminated from consideration because Ru is a magnetic ion and because no comparable magnetically ordered layer is known to superconduct at temperatures as high as ~45 K. (ii) The Gd layer itself clearly does not superconduct (especially p type). (iii) The cuprate planes can be ruled out because Gd has $L = 0$ and $J \neq 0$, which indicates that the Gd energy levels are unsplit by the crystal fields: Gd should break Cooper pairs in the adjacent (cuprate) planes, as it does in $Gd_{2-z}Ce_zCuO_4$ and in the BaO layers of Cu-doped Ba_2GdRuO_6 [10, 16]. Moreover, the Cu ions themselves are magnetically

ordered and exhibit weak-ferromagnetism (or antiferromagnetism), ruling out their participation in superconductivity, according to most theories. (iv) That leaves the SrO layers which are sufficiently remote from the pair-breaking Gd to superconduct in $GdSr_2Cu_2RuO_8$, as the SrO layers do in Cu-doped Sr_2YRuO_6, which has no cuprate planes [17].

Similar arguments can be extended to $Gd_{2-z}Ce_zSr_2Cu_2RuO_{10}$, which also begins to superconduct at around ~45 K, and has almost the same layers as $GdSr_2Cu_2RuO_8$, with two $Gd_{1-z/2}Ce_{z/2}$ layers and one O_2 layer (the three of which replace one Gd layer) between two staggered half-cells of $GdSr_2Cu_2RuO_8$ (without its Gd).

From this perspective, it comes as no surprise that the three ruthenate compounds, doped Sr_2YRuO_6, $GdSr_2Cu_2RuO_8$, and $Gd_{2-z}Ce_zSr_2Cu_2RuO_{10}$, all *begin* to superconduct around ~45 K, even though full superconductivity sets in at lower temperatures for some of the compounds (i.e., 23 K for Cu-doped Sr_2YRuO_6).

The cuprate plane Cu is not expected to be both weak-ferromagnetic (or antiferromagnetic) and superconducting, and so these data are inconsistent with a spin-fluctuation model [10].

The same Cu resonance occurs in both systems, $GdSr_2Cu_2NbO_8$ and $GdSr_2Cu_2RuO_8$, which implies that it is caused by Cu, not by Ru.

To our knowledge, no one has explained why $GdSr_2Cu_2RuO_8$ superconducts at ~45 K, instead of at ~90 K, as observed for $GdBa_2Cu_3O_7$. In our view, the reduction of T_c from ~90 K for $GdBa_2Cu_3O_7$ to ~45 K for $GdSr_2Cu_2RuO_8$ is due to pair-breaking in the SrO layers by the adjacent Ru, as observed in Sr_2YRuO_6 (doped with Cu) [16], and so is further evidence against the superconductivity occupying the cuprate planes.

6. CONCLUSIONS

We have looked at two structures, the first of which is $GdSr_2Cu_2RuO_8$ in which Ru can be replaced by Nb and the second of which is Ba_2GdRuO_6, into which we have substituted Cu on Ru sites. We have found that the low-field resonances in $GdSr_2Cu_2RuO_8$ occur independent of replacement of Ru by Nb. Therefore, we have assigned these resonances to Cu. Our previous magnetic resonance studies of $Ba_2GdRu_{1-u}Cu_uO_6$ have shown that Ru^{+5} contributed no resonant response and that the low-field resonance observed was associated with Cu.

The evidence is conclusive: the magnetic sublattice responsible for the low-field resonance is the one containing Cu. Hence, the cuprate planes should not superconduct (according to most theories), and the SrO layers must superconduct.

We conclude that (1) the $RSr_2Cu_2RuO_8$ materials superconduct for R = Gd (and for R = Eu or Y) because

the superconducting SrO layers are remote from the pair-breaking rare-earth ion Gd; (2) the $R_{2-z}Ce_zSr_2Cu_2RuO_{10}$ sister materials superconduct for R = Gd (and R = Eu) for similar reasons; (3) the material Ba_2GdRuO_6, whether undoped or doped with Cu on Ru sites, does not superconduct because Gd, having $L = 0$ and $J \neq 0$, breaks Cooper pairs in its adjacent BaO layers; and (4) Cu-doped Sr_2YRuO_6 does superconduct in its SrO layers, because Y, unlike Gd, which has $J \neq 0$, is not a Cooper pair-breaker.

The superconducting materials, (i) doped-Sr_2YRuO_6, (ii) (rare-earth)$Sr_2Cu_2RuO_8$, and (iii) (rare-earth)$_{2-z}Ce_zSr_2Cu_2RuO_{10}$, are simply explained as superconductors whose SrO layers all superconduct with (onset) T_c near ~45 K, while Cu-doped Ba_2GdRuO_6 does not superconduct because of Gd pair-breaking. Materials such as $GdSr_2Cu_2NbO_8$ do not superconduct but are insulators because their Nb electrons occupy filled orbitals and filled bands below the Fermi energy.

ACKNOWLEDGMENTS

REFERENCES

1. C. Bernhard, J. L. Tallon, Ch. Niedermayer, *et al.*, Phys. Rev. B **59**, 14099 (1999).
2. A. Fainstein, E. Winkler, A. Butera, and J. Tallon, Phys. Rev. B **60**, 12597 (1999).
3. O. Chmaissem, J. D. Jorgensen, H. Shaked, *et al.*, Phys. Rev. B **61**, 6401 (2000).
4. K. Nakamura, K. T. Park, A. J. Freeman, and J. D. Jorgensen, Phys. Rev. B **63**, 024507 (2000).
5. J. W. Lynn, B. Keimer, C. Ulrich, *et al.*, Phys. Rev. B **61**, 14964 (2000).
6. H. A. Blackstead, J. D. Dow, D. R. Harshman, *et al.*, Physica C (Amsterdam) **354–365**, 305 (2001).
7. P. Monthoux and D. Pines, Phys. Rev. Lett. **69**, 961 (1992).
8. E. A. Turov, *Physical Properties of Magnetically Ordered Crystals* (Academic, New York, 1965), pp. 65, 157.
9. H. A. Blackstead, J. D. Dow, D. R. Harshman, *et al.*, *Recent Progress in the Study of Ruthenate High-Temperature Superconductivity* (in press).
10. H. A. Blackstead, J. D. Dow, D. R. Harshman, *et al.*, Phys. Rev. B **63**, 214412 (2001).
11. J. A. Hodges, P. Bonville, and A. Forget, J. Magn. Magn. Mater. **204**, 49 (1999).
12. J. A. Hodges, Y. Sidis, P. Bourges, *et al.*, Phys. Rev. B **66**, 020501 (2002).
13. H. A. Blackstead, J. D. Dow, I. Felner, *et al.*, Phys. Rev. B **62**, 1244 (2000).
14. D. R. Harshman, W. J. Kossler, A. J. Greer, *et al.*, Physica B (Amsterdam) **364–365**, 392 (2001).
15. D. R. Harshman, W. J. Kossler, A. J. Greer, *et al.*, Phys. Rev. B (in press).
16. H. A. Blackstead, J. D. Dow, D. R. Harshman, *et al.*, Eur. Phys. J. B **15**, 649 (2000).
17. The $YRuO_4$ layers of Sr_2YRuO_6, because of their Ru ions, are ferromagnetically ordered in each $YRuO_4$-layer. Since there is no known case of a material that features ferromagnetism and superconductivity in the same layer, at temperatures near ~45 K, the superconductivity must occur in the SrO layers. Nearest-neighbor $YRuO_4$ layers in the *c*-direction are oppositely polarized magnetically in their *a–b* planes with a SrO layer in between, implying that the magnetic field in each SrO layer (between two oppositely polarized $YRuO_4$ layers) vanishes.
18. D. R. Harshman, W. J. Kossler, A. J. Greer, *et al.*, Physica B (Amsterdam) **289–290**, 360 (2000).

Pseudogap Behavior of Nuclear Spin Relaxation in High-T_c Superconductors in Terms of Phase Separation¶

L. P. Gor'kov[1, 2] and G. B. Teitel'baum[3, *]

[1] *National High Magnetic Field Laboratory, Florida State University, Tallahassee, FL 32310, USA*
[2] *Landau Institute for Theoretical Physics, Chernogolovka, Moscow region, 142432 Russia*
[3] *Zavoiskii Institute for Technical Physics, Russian Academy of Sciences, Kazan, 420029 Russia*
*e-mail: grteit@dionis.kfti.knc.ru
Received July 7, 2004

We analyze anew experiments on the NMR in cuprates and find an important information on their phase separation and its strip character hidden in the dependence of $1/^{63}T_1$ on the degree of doping. In a broad class of materials, $1/^{63}T_1$ is the sum of two terms: the temperature-independent one attributed to "incommensurate" strips that occur at external doping and a "universal" temperature-dependent term ascribed to moving metallic and antiferromagnetic subphases. We argue that the frustrated first-order phase transition in a broad temperature interval bears a dynamical character. © 2004 MAIK "Nauka/Interperiodica".

PACS numbers: 74.25.Hf; 74.72.-h; 76.60.-k

Soon after the discovery of high-temperature superconductivity (HTSC) in cuprates by Bednorz and Muller in 1986, it was suggested theoretically [1] that the materials should manifest a tendency to inherent phase segregation involving both lattice and electronic degrees of freedom. Later, other models revealed similar tendency to an inhomogeneous electronic ground state [2–5]. (For an experimental summary, see, e.g., [6–8].) It is currently common to discuss microscopic phase separation (PS) in cuprates as a pattern of the alternating spin-charge strips [9], dynamical or pinned by static defects seen, e.g., in $(LaNd)_{2-x}Sr_xCuO_4$ [10] with Nd doping.

The most intriguing phenomenon in the normal state of cuprates is the pseudogap (PG) seen as a new energy scale or a crossover temperature, T^*, in NMR, tunneling spectra, resistivity, etc. (for review, see, e.g., [11, 12]). We address this highly debated issue by considering the PG regime as a regime of the phase segregation.

Our premise is that $T^*(x)$ marks a temperature below which the system enters mesoscopic dynamical regime of a frustrated first-order phase transition with sizes of the subphases determined by electroneutrality [1, 13]. Unlike [14, 15], changes in the normal properties below such a T^* come not from a symmetry breaking but due to interweaving of regions with different hole contents.

The NMR fingerprints of a static strip phase were observed for the low-temperature tetragonal (LTT) compounds $(LaEu)_{2-x}Sr_xCuO_4$ [16] and

$(LaNd)_{2-x}Sr_xCuO_4$ [17]. Dynamical features are seen in inelastic neutron experiments at frequencies of 10^{12}–10^{13} s^{-1}, exceeding the NMR scale.

In the present paper, we analyze anew vast *experimental* data on nuclear spin relaxation in cuprates to show that, for a broad class of materials, $^{63}T_1^{-1}$ in the PG regime is the *sum of two terms*: the temperature-independent one that we attribute to strips caused by the presence of dopants and a "universal" temperature-dependent term related to the moving metallic and antiferromagnetic (AF) subphases. We argue that, for LSCO, T^* is above the "dome" of superconductivity (SC).

For guidance, we adopt a qualitative two-band view [1, 13]. Basic to it is the assumption that, in the absence of interactions, the energy spectrum of holes for the CuO_2 plane consists of an itinerant band and the periodic array of local levels identified with the d^9 Cu configuration. Although the hole concentration is not a thermodynamic variable, we suggest that doping is accompanied by changes in the charge transfer gap and implements a first-order Mott transition. (The low-temperature Hall effect [18–20] shows that the number of itinerant holes rapidly increases up to one per unit cell near $x = 0.15$.)

New features in [1, 13] as compared to other models [2–5] concern Cu spins: (1) a hole on a d^9 Cu site is bound by the lattice (remnants of the Jahn–Teller effect); (2) a local hole on a d^9 Cu site distorts surrounding lattice, so that the distortions on different sites interact with each other. The elastic energy minimizes

---

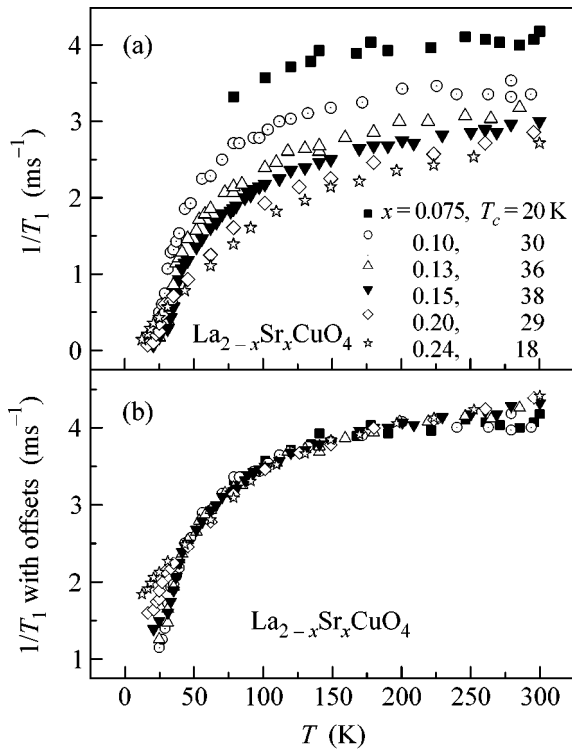¶ This article was submitted by the authors in English.

Fig. 1. The temperature dependence of $1/^{63}T_1(x)$ for LSCO:
(a) the plots for different x and T_c (see inset) are taken from
[23]; at higher temperatures, all of them converge to the
same value of 2.7 ms^{-1} [24]; (b) the same dependences col-
lapsing to the single curve after the corresponding vertical
offsets.

itself by bringing occupied Cu sites together, thus form-
ing nuclei of a dense "liquid" phase of local centers (in
the language of the lattice "liquid–gas"). It is the *lattice*
that triggers liquid–gas transition! An exchange
between holes' spins on the neighboring sites tends to
organize spins of liquid AF subphase.

For holes localized on Cu's in the CuO$_2$ plane, the
lattice liquid–gas transition at some T^* is well known
from the exact solution of the familiar 2D Ising prob-
lem. Taking hole-doped La$_{1-x}$Sr$_x$CuO$_4$, for the sake of
argument, missing (with respect to the Sr ionicity)
holes' density in the AF area must be recompensed by
local metallic inclusions or droplets with higher hole's
content.

We speculate that the tiny structure of subphases
leads to strong fluctuations in islands' sizes and posi-
tions [1]. Boundaries between them move rapidly.
Moving boundary itself is due to the new notion that a
Cu site can merely lose spins when a "metallic" region
crosses over the position of that ^{63}Cu nuclear spin.
Experimentally, one sees only one nuclear resonance
frequency; this provides strict evidence in favor of the
dynamical picture.

In what follows, we address only $1/^{63}T_1$ behavior
because, for cuprates, AF fluctuations prevail over the
Korringa mechanisms.

We now turn to experimental data on $1/^{63}T_1$ for a
number of cuprates. At high enough temperatures, itin-
erant holes and Cu d^9 states form a homogeneous
phase. In particular, we will also address means to
determine T^*, which, because of the Coulomb effects,
manifests itself only as a start of a new fluctuation
regime.

A widespread view is that PG $T^*(x)$ is a density of
states (DOS) crossover. In the (T, x) plane, it crosses the
SC dome, T_c (see, e.g., [21, 22]). We take a different
view. In Fig. 1a, we collected data on $1/^{63}T_1$ in LSCO
from [23]. The following comments are of relevance
here: (1) according to [24], $1/^{63}T_1(T)$ at higher temper-
atures tends to 2.7 ms^{-1} *for all* Sr concentrations, in
spite of the considerable spread seen in Fig. 1a. The
beginning of deviation from that value could be a defi-
nition of $T^*(x)$; (2) note that $1/^{63}T_1$, i.e., dissipation,
monotonically decreases with the decrease of disorder
from small x to 0.24; (3) after an appropriate *vertical*
offset, all curves in Fig. 1a collapse onto the T depen-
dence of $1/^{63}T_1$ for the "optimal" $x = 0.15$ above 50 K
(Fig. 1b). The same tendency is seen in Figs. 2a and 2b
for YBCO (6.5) doped with Ca: the data in Fig. 2a for
different z in Y$_{1-z}$Ca$_z$Ba$_2$Cu$_3$O$_{6.5}$ [25] all fall on the top
of each other in Fig. 2b.

This prompts us to verify whether the same "offset-
tings" of the $1/^{63}T_1$ data apply to a broader group of
materials. The stoichiometric YBa$_2$Cu$_4$O$_8$ possesses no
structural or defect disorder, and we adjust all data to
the $1/^{63}T_1$ behavior for this material [21]. Figure 2c
shows that, after a vertical shift in $1/^{63}T_1$, all the materi-
als indeed follow the same universal temperature
dependence above their T_c and below 300 K. In other
words, in this temperature range, the nuclear spin relax-
ation in these cuprates is a sum of contributions from
two parallel processes:

$$1/^{63}T_1 = 1/^{63}\overline{T}_1(x) + 1/^{63}\widetilde{T}_1(T). \qquad (1)$$

In Eq. (1), $1/^{63}\overline{T}_1(x)$ depends on a material and a degree
of disorder (x) but does not depend on temperature,
while $1/^{63}\widetilde{T}_1(T)$ depends only on temperature, is the
same for all these compounds and coincides with the
$1/^{63}T_1$ for the two chains YBCO 124 above its $T_c = 62$ K.

The decomposition (1) into two parallel dissipation
processes shows that usual definitions of T^* [22] have
no grounds. In Fig. 1a, the LSCO data with $x < 0.15$ are
spread even above 250 K. As a rough estimate for T^*, it
is much higher than the SC onset temperature.

Figure 3 and the table present the dependence on x
for $1/^{63}\overline{T}_1$ in La$_{2-x}$Sr$_x$CuO$_4$ and provide the offsets

(i.e., $1/{}^{63}\overline{T}_1$ terms) for other materials. We return to discussion of the two terms of Eq. (1) later.

The observation that is central for the following is that, in all the materials with nonzero $1/{}^{63}\overline{T}_1$, incommensurate (IC) peaks have been observed in neutron scattering [28]. Peaks are close to the $[\pi, \pi]$ point: at $[\pi(1 \pm \delta), \pi]$ and $[\pi, \pi(1 \pm \delta)]$ [10]. We will now look for the connection between these two phenomena.

Discovery of IC spin fluctuations presented a challenge for explaining the NMR results for the oxygen spin relaxation times: hyperfine field "leaks" originated by the AF incommensurate fluctuations would considerably increase the oxygen's relaxation rates, but this was not seen experimentally. Slichter (see [29]) interpreted these contradictions in terms of "discommensurations": a periodic array of soliton-like walls separating regions with a short-range AF order. Unlike neutrons, the NMR as a local probe does not feel the overall periodicity.

As a theory attempt to put the IC peaks into the context of the *dynamical* PS separation, consider first a stoichiometric material like YBCO 124. Below some T^*, we expect the system to break-up into subphases: the one with a richer content of the Cu spins (AF phase), and the second, with an excess of carriers [1, 13]. The system passes T^* gradually and remains macroscopically homogeneous. PS would express itself in strong fluctuations that provide for the $1/{}^{63}\widetilde{T}_1(T)$ term in Eq. (1).

Under doping, the system (LSCO) must screen excess charge (Sr^{2+}) in AF regions. External doping introduces features that may have something to do with pinning or structural changes. For the Nd-doped LSCO, $La_{2-x-y}Nd_ySr_xCuO_4$ (for the summary below, see experiments [30–33]), doping of $La_{1.6}Nd_{0.4}CuO_4$ with Sr reproduces all features, including SC at lower temperatures, of $La_{1-x}Sr_xCuO_4$ itself with that important difference that strips easily become static. *Elastic lattice/charge* IC peaks were seen in [32] at $\pi[2 \pm \delta, 0, 0]$ with the lattice distortions along the modulation direction (IC peaks positions in [32] are defined by $\epsilon = \delta/2$). Lattice peaks appear first at cooling, followed by the static magnetic peaks. According to [32], pinning of IC distortions can be ascribed to the pattern of the octahedra tilts and redistribution of the Cu–O bonds in the LTT phase that sets in LaNdSCO at higher temperatures [30]. (Unlike the high-temperature tetragonal phase (HTT), the LTT phase contains four formula units per primitive cell.) Strips of AF ordered phase alternate with metallic domain walls. Such strip arrangement by itself is nothing but an optimization of the competing Coulomb and lattice forces [3].

Note that the strips at low temperature finally acquire a long-range order even in LSCO (at smaller x [34]), breaking the symmetry of the ground state. The way of the "coexistence" of SC and the strip order in
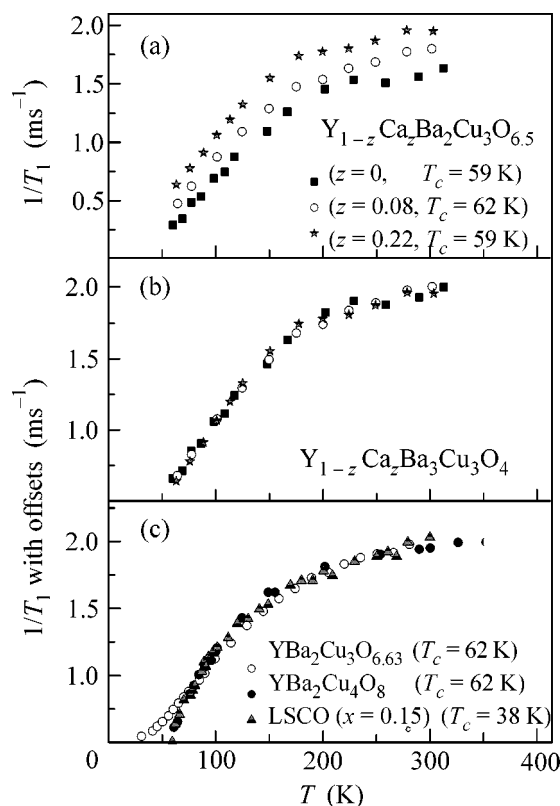

Fig. 2. The temperature dependence of $1/{}^{63}T_1$ for different compounds: (a) for $Y_{1-z}Ca_zBa_2Cu_3O_{6.5}$ with different Ca content z [25]; (b) the same curves overlaid at each other by the vertical offsets; (c) the $1/{}^{63}T_1$ for YBCO (123) [26] overlaid with that for LSCO [23] and YBCO (124) [21].
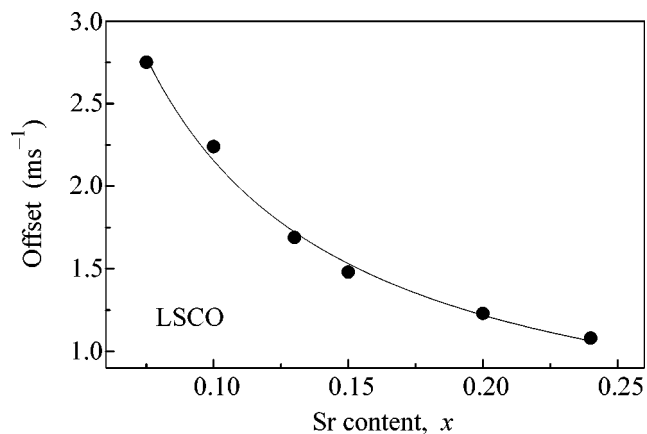

Fig. 3. The offset $1/{}^{63}\overline{T}_1(x)$ vs. Sr content x for LSCO (relative to that for YBCO 124); the line is a visual guide. Inset: the offsets for some other compounds (data for underdoped (u) and overdoped (o) BISCCO 2212 deduced from [27]; to compare BISCCO with LSCO and YBCO materials, the hyperfine constants have to be properly adjusted).

Table

Material		Offset
YBCO 124		0
BISCO-u	($T_c = 90$ K)	0.11
BISCO-o	($T_c = 77$ K)	0.15
YBCO 123	Ca = 0	0.13
YBCO 123	Ca = 0.08	0.26
YBCO 123	Ca = 0.22	0.45
LSCO	Sr = 0.15	1.47

the same sample remains unresolved: one view treats the new strip symmetry as a superstructure superimposed on the Fermi surface that change the energy spectrum like any SDW/CDW can do it (e.g., [9]). Another plausible alternative would be a spatially inhomogeneous coexistence of the nonsuperconducting IC AF phase and a metallic phase with strong fluctuations.

Coexistence of an SC and the IC AF phases at low temperatures was confirmed recently by the neutron diffraction experiments [35] for $La_{2-x}Sr_xCuO_4$ ($x = 0.10$) in the vortex state. (The coexistence of SC and AF formations was also found from the μSR spectra [36].)

One can now say that, with the temperature increase, the static phase coexistence melts into the dynamical regime governed by the Coulomb interactions. "Discommensurations" suggested by Slichter (see [29]) ought to be corrected: IC excitations should indeed consist of alternating strips of the short-range AF order but separated by walls that store the compensating charge. Direct correspondence between x and δ: $\delta/2 \ (\equiv \epsilon) \approx x$ found for $0.05 \leq x \leq 1/8$ saturates for $x > 1/8$ at $d \approx 1/4$ [37]. Figure 3 allows to consider the tendency as an increase in the share of the metallic fraction.

We shall now make an attempt to agree on a semiquantitative level the observed IC magnetic peaks in $La_{2-x}Sr_xCuO_4$ with the values of the first term in Eq. (1). We concentrate on $La_{1.86}Sr_{0.14}CuO_4$ for which the most detailed data are available [38].

With the notation from [39]

$$1/T_1 = \frac{k_B T}{2\mu_B^2 \hbar^2 \omega} \sum_i F(Q_i) \int \frac{d^2 q}{(2\pi)^2} \chi''(q, \omega \longrightarrow 0), \quad (2)$$

where Q_i stands for one peak, hyperfine "tensor" $F(Q) = \{A_\perp + 2B[\cos(Q_x) + \cos(Q_y)]\}^2$, and for $\chi''(q, \omega \longrightarrow 0)$, we take near single peak, say $[\pi(1 - \delta), \pi]$

$$\chi''(q, \omega) = \frac{\chi''_{peak}(T)\omega}{[1 + (x\xi_x)^2 + (y\xi_y)^2]^2}, \quad (3)$$

where $(x, y) = (q_x - \pi(1 - \delta); q_y - \pi)$ and ξ_x and ξ_y are the correlation lengths in the two proper directions.

After integration, the contribution from strips with q along the x direction is

$$1/^{63}T_1 = \frac{k_B T}{\pi \mu_B^2 \hbar \xi_x \xi_y} \{A_\perp - 2B[\cos(\pi\delta) + 1]\}^2 \chi''_{peak}. \quad (4)$$

Experimentally [38], $\chi''_{peak}(T) \propto T^{-2}$ and, for $x = 0.14$, $\delta = 0.245 \sim 1/4$. Assuming the T^{-1} dependence [38] only for the one of ξ's, ξ_x, and using for $A_\perp$ and B the known values [39], one obtains $1/^{63}T_1 = (4/\xi_y)$ ms^{-1}. With the AF correlation length $\xi_y \sim 4$, this is the correct order of magnitude.

The descending dependence of the offset (Fig. 3) agrees qualitatively with the behavior of $\delta(x)$ [37] in Eq. (4). For a quantitative description, one needs to know the x dependence for $\chi''_{peak}(T)$. Such data in the absolute units are so far lacking, except [38]. In addition, with the x increase, buckling in the CuO_2 planes is known to decrease, diminishing pinning effects and making the local symmetry of the CuO_2 unit the same as in other materials from the class with small offset in Fig. 3. The system grows metallic with a high hole content [18–20].

Thus, the only pseudogap feature in the NMR data that survives in Fig. 2c is the one for YBCO 124: a change of the regime between 130 and 180 K. Similar drop in the width for the Ho crystal field excitations was found in [40] for another 124-compound, Ho-124, in about the same temperature interval. It would be tempting to view the regime change again in the PS terms. However, note that the AF fluctuations cancel at the Ho positions, and the relaxation seen in [40] appears as metallic Korringa law. In [40], DOS's, as characterizing linear slops in T dependences outside the crossover interval, are almost the same, so that whatever is meant by the transitional area in Fig. 2c for Ho-124, it is not a simple gap opening [21]. Recall that properties of both YBCO 124 and the optimally doped LSCO (for review, see [11]) are unusual in a very broad temperature interval and are best understood in terms of the "marginal" Fermi liquid model [41]. Therefore, we leave the origin of the universal term in Eq. (1) open to further discussions.

Two words regarding our choice (ξ_x, ξ_y). We assumed anisotropic spin correlation widths with the one along *commensurate* AF direction to be temperature-independent. Asymmetry is expected, although the experimental verification remains to be done. Rapid growth of the width of the neutron peak along modulation direction, q_x (linear in temperature [38]), reflects the low energy cost for magnetic excitations in LSCO ($x = 0.14$) (the width from the strips "bending" should have given the $T^{1/2}$ dependence for both ξ's).

To summarize, we have found that, in a temperature interval above T_c and below some $T^* \sim 300$ K, the nuclear spin relaxation for a broad class of cuprates comes from two independent mechanisms: relaxation

on the "striplike" excitations that leads to a temperature-independent contribution to $1/^{63}T_1$ (originating due to the presence of external doping or disorder) and a universal temperature-dependent term. For $La_{1.86}Sr_{0.14}CuO_4$, we obtained a correct quantitative estimate for the value of the first term. We argue that the whole pattern fits well the notion of the dynamical PS into coexisting metallic and IC magnetic phases. Experimentally, it seems that, with the temperature decrease, dynamical PS acquires a static character with the IC symmetry breaking for AF phase dictated by the competition between the lattice and the Coulomb forces.

REFERENCES

1. L. P. Gor'kov and A. V. Sokol, JETP Lett. **46**, 420 (1987).
2. J. E. Hirsch *et al.*, Phys. Rev. B **39**, 243 (1989).
3. J. Zaanen *et al.*, Phys. Rev. B **40**, 7391 (1989).
4. V. J. Emery *et al.*, Phys. Rev. Lett. **64**, 475 (1990).
5. M. Grilli *et al.*, Phys. Rev. Lett. **67**, 259 (1991).
6. T. Egami and S. J. L. Billinge, in *Physical Properties of High-Temperature Superconductors V*, Ed. by D. M. Ginsberg (World Sci., Singapore, 1996), p. 265.
7. S. H. Pan *et al.*, Nature **413**, 282 (2001).
8. C. Howald *et al.*, Phys. Rev. B **67**, 014533 (2003).
9. M. I. Salkola *et al.*, Phys. Rev. Lett. **77**, 155 (1996); R. S. Markiewicz *et al.*, Phys. Rev. B **65**, 064520 (2002).
10. J. M. Tranquada *et al.*, Nature **375**, 561 (1995).
11. T. Timusk and B. Statt, Rep. Prog. Phys. **62**, 61 (1999).
12. J. L. Tallon and J. M. Loram, Physica C (Amsterdam) **349**, 53 (2001).
13. L. P. Gor'kov, J. Supercond. **14**, 365 (2001).
14. S. Chakravarty *et al.*, Phys. Rev. B **63**, 094503 (2001).
15. A. Kaminsky *et al.*, Nature **416**, 610 (2002).
16. G. Teitel'baum *et al.*, Phys. Rev. Lett. **84**, 2949 (2000).
17. G. Teitel'baum *et al.*, Phys. Rev. B **63**, 020507 (2001).
18. S. Uchida *et al.*, Physica C (Amsterdam) **162–164**, 1677 (1989).
19. T. Nishikawa *et al.*, J. Phys. Soc. Jpn. **62**, 2568 (1993).
20. F. Balakirev *et al.*, Nature **424**, 912 (2003).
21. G. V. M. Williams *et al.*, Phys. Rev. B **58**, 15053 (1998).
22. J. Schmalian *et al.*, Phys. Rev. B **60**, 667 (1999).
23. S. Oshugi *et al.*, J. Phys. Soc. Jpn. **63**, 700 (1994).
24. T. Imai *et al.*, Phys. Rev. Lett. **70**, 1002 (1993).
25. P. M. Singer *et al.*, Phys. Rev. Lett. **88**, 187601 (2002).
26. M. Takigawa *et al.*, Phys. Rev. B **43**, 247 (1991).
27. R. E. Walstedt *et al.*, Phys. Rev. B **44**, 7760 (1991).
28. S. W. Cheong *et al.*, Phys. Rev. Lett. **67**, 1791 (1991); H. A. Mook *et al.*, Nature **395**, 580 (1998); M. Arai *et al.*, Phys. Rev. Lett. **83**, 608 (1999); A. Bianconi, Int. J. Mod. Phys. B **14**, 3289 (2000); P. Dai *et al.*, Phys. Rev. B **63**, 054525 (2001).
29. V. Barzykin *et al.*, Phys. Rev. B **50**, 16052 (1994).
30. M. K. Crawford *et al.*, Phys. Rev. B **44**, 7749 (1991).
31. J. M. Tranquada *et al.*, Phys. Rev. Lett. **78**, 338 (1997).
32. J. M. Tranquada *et al.*, Phys. Rev. B **54**, 7489 (1996).
33. J. M. Tranquada *et al.*, Phys. Rev. B **59**, 14712 (1999).
34. M. Fujita *et al.*, Phys. Rev. B **65**, 064505 (1991).
35. B. Lake *et al.*, Nature **415**, 299 (2002).
36. Ch. Niedermayer *et al.*, Phys. Rev. Lett. **80**, 3843 (1998).
37. K. Yamada *et al.*, Phys. Rev. B **57**, 6165 (1998).
38. H. Aeppli *et al.*, Science **278**, 1432 (1997).
39. Y. Zha *et al.*, Phys. Rev. B **54**, 7561 (1996).
40. D. Rubio Temprano *et al.*, Phys. Rev. Lett. **84**, 1990 (2000).
41. C. M. Varma *et al.*, Phys. Rev. Lett. **63**, 1996 (1989).

Long-Wavelength Magnetic Excitations in the Fe$_{65}$Ni$_{35}$ Alloy

Yu. N. Mikhailov* and V. A. Kazantsev

Institute of Metal Physics, Ural Division, Russian Academy of Sciences,
ul. S. Kovalevskoi 18, Yekaterinburg, 620219 Russia
* e-mail: mikhailov@uraltc.ru
Received July 7, 2004

A theoretical analysis of small-angle neutron scattering is performed for the Fe$_{65}$Ni$_{35}$ alloy at a temperature $T = 0.9T_C = 450$ K. The results obtained indicate the existence of long-wavelength magnetic excitations that do not correspond to spin waves of the Holstein–Primakoff type. The possible nature of these excitations is discussed. © 2004 MAIK "Nauka/Interperiodica".

PACS numbers: 75.30.–m; 75.25.+z

1. INTRODUCTION

Measurements of the temperature dependence of intensity of small-angle neutron scattering at fixed wave vectors **q** in the Fe$_{65}$Ni$_{35}$ and Fe$_3$Pt alloys show wide maxima at $T < T_C$ (second-type scattering) [1], apart from the peaks of adiabatic critical scattering at the Curie point (scattering of the first type). The intensities of these maxima and the temperature ranges in which they exist depend on the magnitude of **q** and the sample. Earlier, second-type scattering was observed in Fe and was ascribed only to neutron scattering by spin waves [2]. However, such treatment does not agree with the experimental results obtained on Fe$_{65}$Ni$_{35}$ and Fe$_3$Pt alloys [1], since the cutoff angles for spin-wave neutron scattering (at appropriate temperatures) are smaller than those at which second-type scattering continues to exist. Therefore, we may suppose that second-type scattering contains some additional magnetic contribution, apart from the spin-wave one.

The total cross section for critical neutron scattering in ferromagnets at $T < T_C$ is written as [3]

$$d^2\sigma/d\Omega d\varepsilon \sim [(1 - \cos^2\alpha)\chi_\parallel(q)F_\parallel(q, \varepsilon) \\ + (1 + \cos^2\alpha)\chi_\perp(q)F_\perp(q, \varepsilon)], \tag{1}$$

where $\chi_\parallel(\mathbf{q})$ and $\chi_\perp(\mathbf{q})$ are the longitudinal and transverse static magnetic susceptibilities, respectively; $F_\parallel(\mathbf{q}, \varepsilon)$ and $F_\perp(\mathbf{q}, \varepsilon)$ are the functions of the spectral density of longitudinal and transverse spin components; and α is the angle between the scattering vector and the direction of magnetization ($\cos^2\alpha = 1/3$ without an external magnetic field). For the directions $\mathbf{H} \parallel \mathbf{q}$ and $\mathbf{H} \perp \mathbf{q}$ of the external saturation magnetic field, Eq. (1) takes the form $[2\chi_\perp(\mathbf{q})F_\perp(\mathbf{q}, \varepsilon)]$ and $[\chi_\parallel(\mathbf{q})F_\parallel(\mathbf{q}, \varepsilon) + \chi_\perp(\mathbf{q})F_\perp(\mathbf{q}, \varepsilon)]$, respectively; from a comparison of these expressions with experimental data of [1], we see that

$$[2\chi_\perp(\mathbf{q})F_\perp(\mathbf{q}, \varepsilon)] \\ < [\chi_\parallel(\mathbf{q})F_\parallel(\mathbf{q}, \varepsilon) + \chi_\perp(\mathbf{q})F_\perp(\mathbf{q}, \varepsilon)]. \tag{2}$$

Inequality (2) indicates the existence of a noticeable contribution of $\chi_\parallel(\mathbf{q})F_\parallel(\mathbf{q}, \varepsilon)$ to the critical scattering cross section in the Fe$_{65}$Ni$_{35}$ and Fe$_3$Pt alloys. Therefore, it is of significant interest to perform an energy analysis of the second-type scattering in these alloys.

2. RESULTS

In this work, the measurements were carried out using a polycrystalline Fe$_{65}$Ni$_{35}$ alloy on a triaxial spectrometer (TASP, SINQ, Paul Scherrer Institute, Villingen, Switzerland). All experiments were conducted at a temperature of $T = 0.9T_C = 450$ K. Using the $\mathbf{Q}$ = const method (without an external magnetic field, at $E_f = 4.9$ meV), we measured peaks of inelastic neutron scattering for several wave vectors. The results obtained are shown by solid circles in Fig. 1 (curve *1*). As is known, the expression for the energy of spin waves (of the Holstein–Primakoff type) in an isotropic ferromagnet has the form [4]

$$E_q = [(Dq^2 + g\mu_B H) \\ \times (Dq^2 + g\mu_B H + 4\pi g\mu_B M_O \sin^2\vartheta_q)]^{1/2}. \tag{3}$$

For comparison, Fig. 1 also displays the calculated dispersion curve *2* without an external magnetic field $E_q = [D^2q^4 + 4Dq^2\pi g\mu_B M(450 \text{ K})\sin^2\vartheta_q]^{1/2}$ at D (450 K) = 70 meV Å^2 borrowed from [5]. It is seen that the experimental curve *1* is less steep, and the extrapolation to $q = 0$ yields, unlike the calculated curve, an energy gap.

Then, we obtained the $\mathbf{Q} = 0$ spectra for $q = 0.06$ Å^{-1} in a magnetic field $\mathbf{H} = 500$ Oe perpendicular to **q** and

without a field. The results of these measurements at two energies of scattered neutrons (E_f = 3.9 and 4.9 meV) are displayed in Fig. 2. The inelastic-scattering peaks with the loss and gain of energy by neutrons are cut because of kinematic restrictions associated with the small wave number of the primary neutron beam k_i, at which the maximum energy transfer is E_{max} = $\pm 2C_q k_i$, where C = 2.0719 meV Å^2. It follows from the spectra obtained that the ratio of the intensities of inelastic peaks in a magnetic field and without a field for various E_f is opposite. This behavior of the intensities of inelastic peaks cannot be related only to the scattering by spin waves; it is most likely caused by some other magnetic excitations.

To test this assumption, we performed an energy analysis in that region of the E–q plane where the section of the ellipsoid of the spectrometer resolution (whose total dimensions in this plane are $\Delta E \cong$ 0.24 meV and $\Delta q \cong 0.05$ Å^{-1} at E_i = 3.9 meV) does not touch curves 1 and 2. To fulfill this condition at small wave vectors and remove the kinematic energy limitation, we performed measurements by scanning at a constant scattering angle. The inset in Fig. 3 shows the results of such energy analysis for q_0 = 0.12 Å^{-1} for the energy of incident neutrons E_i = 3.9 meV. After a mathematical treatment of the experimental data (approximation of the central elastic peak by a Gaussian and of the side peaks by Lorentzians), it is seen that the spectrum has a three-peak structure, with the side peaks located at the energy transfer $E \cong \pm 0.3$ meV. In Fig. 1, part of the scanning trajectory recorded by the constant-scattering-angle method is shown as curve 3. The open circle in this curve corresponds to the energy and the wave vector of one of the resolved side maxima.

3. DISCUSSION

The $Fe_{65}Ni_{35}$ and Fe_3Pt alloys [5] exhibit a significant discrepancy between the experimentally measured temperature dependences of the spontaneous magnetization $M(T)$ and calculated magnetizations $M_s(T)$ obtained in terms of the spin-wave theory

$$M_s(T) = M(0)(1 - BT^{3/2}), \qquad (4)$$

where $M(0)$ is the magnetization at T = 0 K and B = $[2.612\, g\, \mu_B/M(0)][k_B/4\pi D(T)]^{3/2}$. This fact is ascribed to the difference in the coefficients of spin-wave stiffness $D(T)$ determined from magnetic and neutron-scattering measurements. The possible reasons for this difference may be anomalous softening or strong damping of long-wavelength spin waves. However, the neutron-diffraction experiments performed in [6, 7] showed that the behavior of the above spin-wave parameters in these alloys agrees with the conventional theory of a Heisenberg ferromagnet. A satisfactory agreement between $M(T)$ and $M_s(T)$ can be obtained if we assume the existence of additional magnetic excitations in $Fe_{65}Ni_{35}$ and
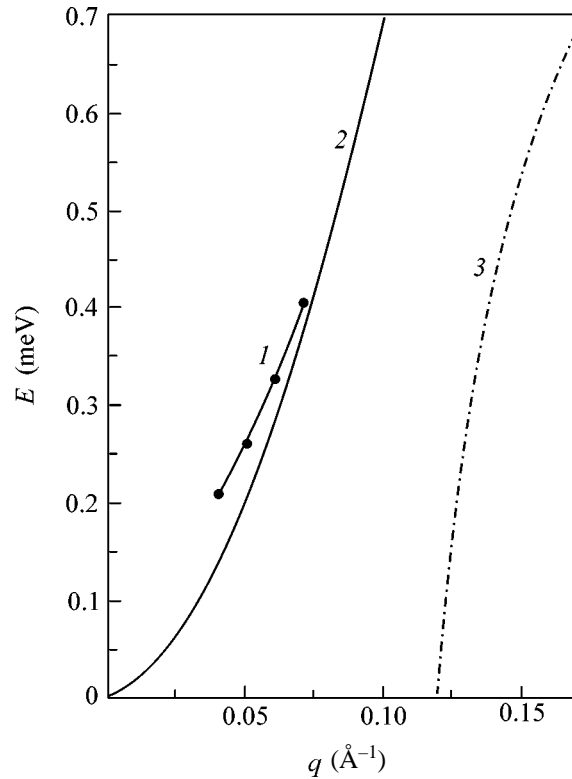

Fig. 1. (1) Energy of neutron-inelastic-scattering peaks as a function of the wave vector, (2) calculated dispersion curve of spin waves in the $Fe_{65}Ni_{35}$ alloy at T = $0.9T_C$, and (3) part of the scanned trajectory obtained using the constant-scattering-angle method at q_0 = 0.12 Å^{-1}.

Fe_3Pt [5]. According to [5], the energy of "hidden" magnetic excitations cannot exceed $E \sim 1$ meV, and the excitations themselves must be observed at small wave vectors.

Let us discuss the possible ways that such excitations may appear. The long-wavelength magnetic dynamics in a multidomain ferromagnet was considered in [8] (see also references therein). It was shown there that, in this case, apart from the intradomain (Holstein–Primakoff) branch of d magnons, two additional branches of magnetic excitations prove to be significant. One of these—w branch—corresponds to vibrations of domain walls (intrawall magnons) and the other—nw branch—is localized near domain walls. The energy of nw magnons is greater than that of d magnons because of the dipole interaction of oscillations of the neighboring-domain magnetizations, which are antiparallel to one another. The wave vectors of magnetic excitations of both types have components only parallel to the plane of the domain wall; therefore, their dispersion relations are anisotropic. At small wave vectors, all three branches are separated, and the spectra of the w and nw magnons have energy gaps even in an isotropic ferromagnet. With increasing wave vector, the w and nw branches merge with d magnons. Such a behavior is caused by both the relative magnitude of
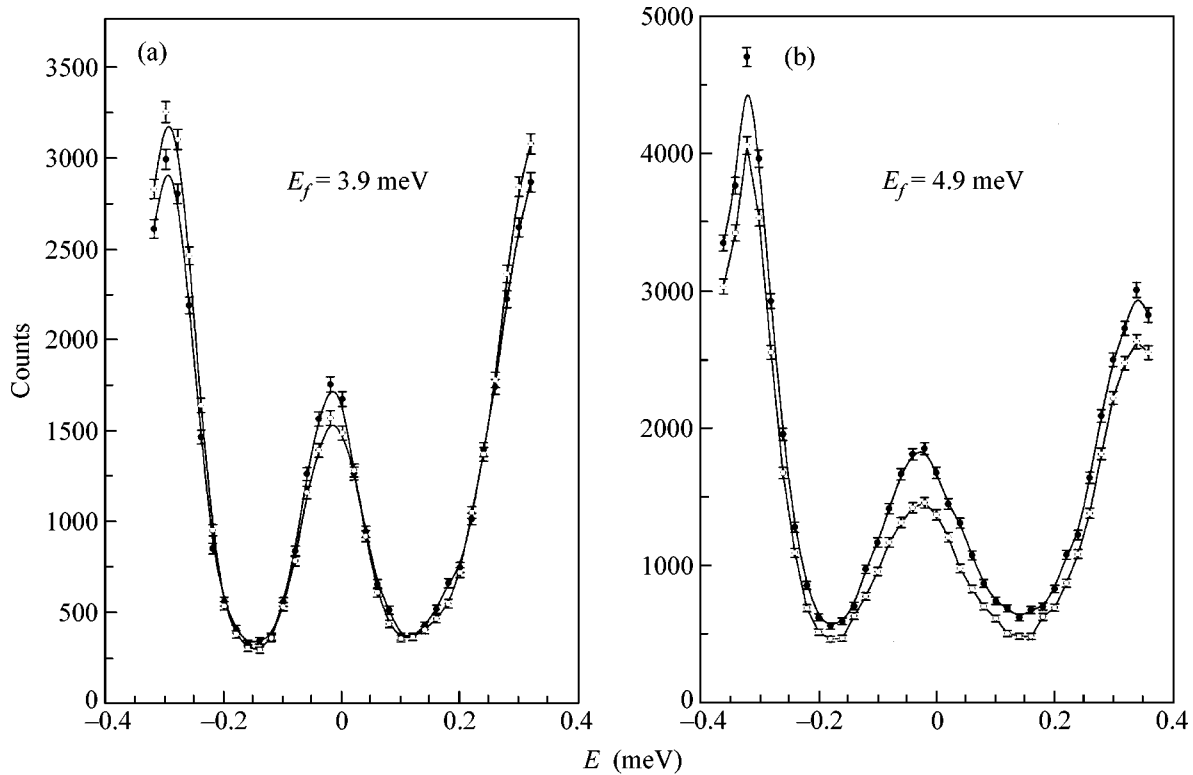
Fig. 2. $\mathbf{Q}$ = const spectra of the $Fe_{65}Ni_{35}$ alloy at $T = 0.9T_C$ and $q = 0.06$ Å^{-1}; ($\circ$) $\mathbf{H} = 0$; ($\bullet$) $\mathbf{H} = 500$ Oe ($\mathbf{H} \perp \mathbf{q}$); (a) $E_f = 3.9$ meV and (b) $E_f = 4.9$ meV.

dipole and exchange interactions and the relationship between the dipole correlation length and the width of the domain wall. Therefore, the spectra of long-wavelength magnetic excitations of realistic (multidomain) ferromagnets significantly differ in different ranges of wave vectors.

Allowing for this circumstance, we can qualitatively explain the dependence of the energies of inelastic peaks on the wave vector in Fig. 1 (curve *1*). At $\mathbf{Q}$ = const scanning, the ellipsoid of resolution of the spectrometer involves regions of the *w* and *nw* branches (noncoincident with *d* magnons in the region of small wave vectors), in which neutron scattering gives noticeable contributions to the inelastic peaks. These contributions shift the experimental peaks toward higher energies. The shifts increase as the wave vector for which scanning is performed decreases, leading to a less steep dispersion curve *1* than in the case of *d* magnons (calculated curve *2*).

Another candidate for the role of "hidden" magnetic excitations are longitudinal spin fluctuations (LSFs). To date, several theoretical works concerning neutron scattering by LSFs have been published. These theories predict single-peak [9], two-peak [10], and three-peak [11, 12] scattering spectra, which, respectively, represent (1) a quasi-elastic central maximum; (2) inelastic peaks corresponding to spin-wave energies; and (3) a central peak with two inelastic maxima at the frequencies of spin waves [11], or with a linear dependence of

the energy of these maxima on the wave vector at a constant temperature [12]. The results of experimental works on neutron scattering by LSFs are also controversial. Using scattering of unpolarized neutrons in an external magnetic field, Ishikawa *et al.* [13] found the existence of LSFs near $E = 0$ in $Fe_{65}Ni_{35}$ and their absence in Fe_3Pt. Later investigations performed using polarized neutrons showed that LSFs exist (also in the form of a diffuse maximum near $E = 0$) in the $Fe_{72}Pt_{28}$ alloy as well [14]. Three-peak spectra caused by LSFs were observed in amorphous ferromagnets [15]. The possible origin of the discrepancies in the results of neutron-scattering studies of LSFs in ferromagnets were discussed in [12].

As is well-known [16–19], a competing exchange interaction exists in the ferromagnetic fcc $Fe_{65}Ni_{35}$ alloy, which leads to an inhomogeneous magnetic structure observed over a wide temperature range below T_C. This inhomogeneous magnetic structure is characterized by not only transverse but also longitudinal spin fluctuations (to a greater extent than in homogeneous ferromagnets) over the entire temperature range. Therefore, we suppose that the low-energy magnetic excitations that were revealed by the constant-scattering-angle method at $q_0 = 0.12$ Å^{-1} (see Fig. 3) are caused by fluctuations of longitudinal components of magnetic moments.
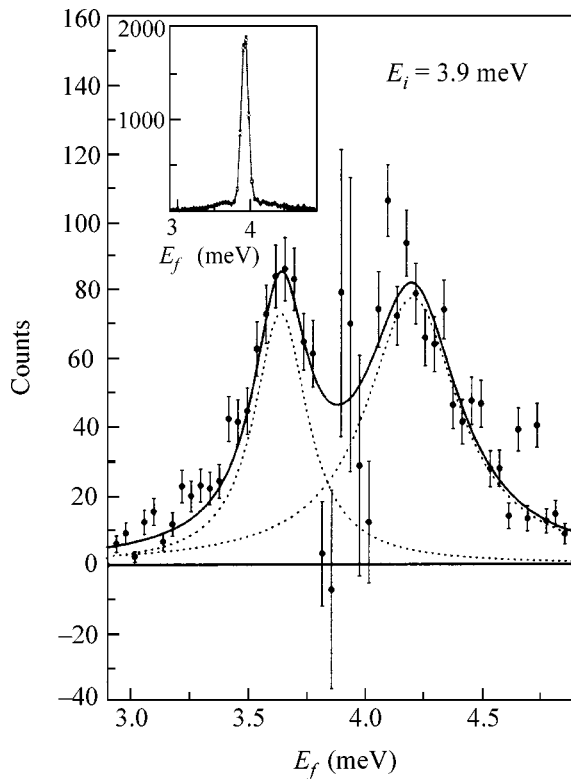
Fig. 3. Side maxima of the spectrum separated by mathematical processing. Inset: energy spectrum in the $Fe_{65}Ni_{35}$ alloy at $T = 0.9 T_C$ and $q_0 = 0.12$ Å^{-1} obtained by the constant-scattering-angle method.

The opposite relationship between the intensities of inelastic peaks obtained in an external magnetic field and without a field at various E_f in Figs. 2a and 2b also can be explained by the presence of LSFs (at smaller wave vectors). To this end, we should take into account the dimensions of the ellipsoid of the spectrometer resolution at two different energies of scattered neutrons ($E_f = 3.9$ and 4.9 meV). The intensity of the inelastic peaks is determined by the dimensions of that part of the $E–q$ space which is swept by the ellipsoid of resolution upon scanning. In the case of the smaller ellipsoid (Fig. 2a, $E_f = 3.9$ meV), an increase in the intensity that comes from LSFs in a magnetic field **H** = 500 Oe perpendicular to **q**, which is related to the first term in Eq. (1), proves to be insufficient to compensate the decrease in the intensity caused by the second term. In the case of the greater ellipsoid of resolution (Fig. 2b, $E_f = 4.9$ meV), when it involves a larger region of the $E–q$ space with smaller wave vectors, the situation is opposite, since, according to [12, Fig. 9b], the intensity due to LSFs increases sharply with decreasing wave vector at temperatures close to the Curie point (e.g., at $\tau = T/T_C = 0.9$, as in our case).

In our opinion, further investigations, using polarized neutrons, should be carried out in this direction in order to determine dispersion relations for all the afore-mentioned magnetic excitations, which may help to explain the anomalous temperature dependence of spontaneous magnetization in the $Fe_{65}Ni_{35}$ alloy.

REFERENCES

1. A. Z. Menshikov, A. Chamberod, and M. Roth, Solid State Commun. **44**, 243 (1982).
2. P. A. Egelstaff, *Thermal Neutron Scattering* (Academic, London, 1965; Atomizdat, Moscow, 1970).
3. Yu. A. Izyumov and N. A. Chernoplekov, in *Neutron Spectroscopy*, Ed. by R. P. Ozerov (Énergoatomizdat, Moscow, 1983; Consultants Bureau, New York, 1994), Vol. 3.
4. S. V. Maleev, Zh. Éksp. Teor. Fiz. **48**, 1448 (1965) [Sov. Phys. JETP **21**, 969 (1965)].
5. Y. Ishikawa, S. Onodera, and K. Tajima, J. Magn. Magn. Mater. **10**, 183 (1979).
6. J. W. Lynn, N. Rosov, M. Acet, *et al.*, J. Appl. Phys. **75**, 6069 (1994).
7. N. Rosov, J. W. Lynn, J. Kastner, *et al.*, J. Appl. Phys. **75**, 6072 (1994).
8. M. I. Kurkin and A. P. Tankeev, Fiz. Met. Metalloved. **36**, 1149 (1973).
9. G. F. Mazenko, Phys. Rev. B **14**, 3933 (1976).
10. J. Villain, in *Critical Phenomena in Alloys, Magnets, and Superconductors*, Ed. by R. E. Mills, E. Ascher, and R. I. Jaffe (McGraw-Hill, New York, 1971), p. 423.
11. V. G. Vaks, A. I. Larkin, and S. A. Pikin, Zh. Éksp. Teor. Fiz. **53**, 1089 (1967) [Sov. Phys. JETP **26**, 647 (1968)].
12. Yu. A. Izyumov and N. I. Chashchin, Fiz. Met. Metalloved. **93**, 23 (2002).
13. Y. Ishikawa, S. Onodera, and K. Tajima, Solid State Commun. **38**, 561 (1981).
14. N. Rosov, J. W. Lynn, J. Kastner, *et al.*, J. Magn. Magn. Mater. **140**, 235 (1995).
15. J. W. Lynn, N. Rosov, and G. Fish, J. Appl. Phys. **73**, 5369 (1993).
16. V. E. Arkhipov, A. Z. Men'shikov, and S. K. Sidorov, Pis'ma Zh. Éksp. Teor. Fiz. **12**, 356 (1970) [JETP Lett. **12**, 243 (1970)].
17. V. I. Goman'kov, I. M. Puzeĭ, V. N. Sigaev, *et al.*, Pis'ma Zh. Éksp. Teor. Fiz. **13**, 600 (1971) [JETP Lett. **13**, 428 (1971)].
18. S. Komura, G. Lippmann, and W. Schmatz, J. Magn. Magn. Mater. **5**, 123 (1977).
19. Y. Wang, G. M. Stocks, D. M. C. Nicholson, *et al.*, J. Appl. Phys. **81**, 3873 (1997).

Translated by S. Gorin

On the Possible Coexistence of Spiral and Collinear Structures in Antiferromagnetic KFe(MoO₄)₂

L. E. Svistov[1, 3], A. I. Smirnov[1], L. A. Prozorova[1], O. A. Petrenko[2],
A. Ya. Shapiro[3], and L. N. Dem'yanets[3]

[1] *Kapitza Institute of Physical Problems, Russian Academy of Sciences, Moscow, 119334 Russia*
[2] *Department of Physics, University of Warwick, Coventry, CV4 7AL, United Kingdom*
[3] *Shubnikov Institute of Crystallography, Russian Academy of Sciences, Moscow, 117924 Russia*
Received July 7, 2004

The static and resonance properties of a quasi-two-dimensional antiferromagnet phase on a distorted triangular lattice of $KFe(MoO_4)_2$ have been experimentally studied. Magnetization curves exhibit features corresponding to the spin-flop transition in a collinear biaxial antiferromagnet and simultaneously show a magnetization plateau characteristic of a triangular spin structure. The magnetic resonance spectra also display absorption lines corresponding to the spin structures of both types. The experimental data are described in terms of a model comprising alternating weakly bound magnetic layers, in which the main two exchange integrals have different values. Below the Néel temperature ($T_N = 2.5$ K), some of these layers possess a collinear antiferromagnetic structure, while the other layers have a triangular or spiral structure. © *2004 MAIK "Nauka/Interperiodica".*

PACS numbers: 75.50.Ee; 75.30.-m

Two-dimensional (2D) antiferromagnets on a regular triangular lattice exhibit unusual magnetic properties due to a partially frustrated antiferromagnetic exchange and the degeneracy (not vanishing in the applied magnetic field) of various spin configurations (see, e.g., [1]). The ground state corresponds to a three-sublattice magnetic structure with the spins mutually oriented at ±120° in a zero field. An important role in the magnetic structure formation is played by fluctuations, which account for the characteristic magnetization plateau (on a level of 1/3 of the saturation magnetization) in a rather broad interval of magnetic fields in the vicinity of $(1/3)H_{sat}$, where H_{sat} is the saturation field. In iron molybdates of the $AFe(MoO_4)_2$ type (A = K, Na, Rb, …), magnetic Fe^{3+} ($S = 5/2$) ions are arranged on plane triangular lattices with weak exchange interaction between neighboring planes, which accounts for the quasi-2D magnetism [2, 3]. In $RbFe(MoO_4)_2$ crystals with a third-order axis (symmetry group D_{3d}^3), each magnetic layer has a regular triangular lattice. These crystals exhibit the properties of quasi-2D antiferromagnets on a regular triangular lattice with a ratio of the lateral and interlayer exchange integrals of 20 [3].

A different situation is observed in $KFe(MoO_4)_2$ crystals, where magnetic ordering takes place on a distorted triangular lattice. At a temperature of $T_1 = 311$ K, this compound exhibits a structural transition from a phase with the aforementioned symmetry group D_{3d}^3 to a monoclinic phase of C_{2h}^3 symmetry [4]. The size of the primitive cell along the **Z** axis perpendicular to the

magnetic layers doubles, and iron ions, Fe_I^{3+} and Fe_{II}^{3+}, appear in nonequivalent positions of two types. The **X** axis remains the second-order axis, and the **YZ** plane is still the symmetry plane (Fig. 1). Owing to this decrease in the symmetry, we may expect that, at $T < T_1$, the exchange integral J_1 for the neighboring iron ions arranged along the **X** axis will differ from the exchange integral J_2 of the neighbors arranged along other directions in the triangular structure. Thus, the triangular
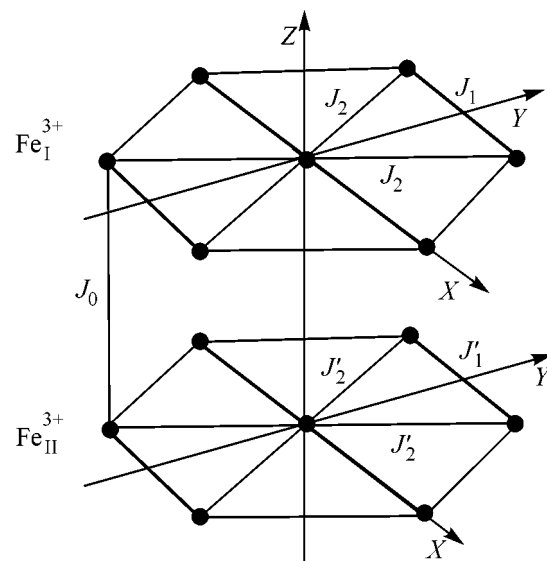

Fig. 1. Schematic diagram showing the arrangement of Fe^{3+} magnetic ions in the crystal structure of $KFe(MoO_4)_2$.

structure of $KFe(MoO_4)_2$ crystals is distorted and the crystals contain layers of magnetic ions occurring in the nonequivalent positions of two types. According to the theoretical analysis [5], a distortion ($J_1 \neq J_2$) corresponding to $J_1 > J_2/2 > 0$ leads to the appearance of an incommensurate spiral structure with the wavevector oriented in the direction (**X** axis) of distinct exchange interaction. In contrast, for $J_2/2 > J_1 > 0$, a collinear antiferromagnetic structure becomes energetically favorable.

This study was aimed at elucidating the effect of lattice distortions on the properties of 2D antiferromagnets on a triangular lattice. For this purpose, we have studied the static and resonance magnetic properties of $KFe(MoO_4)_2$ crystals.

The experiments were performed on $KFe(MoO_4)_2$ single crystals grown by spontaneous crystallization as described in [2]. The crystals had the shape of 0.1- to 0.3-mm-thick plates with a lateral size of up to 3 mm. The face surface of the crystals coincided with the planes of iron ions. At temperatures below T_1, the crystal separates into three domains corresponding to the three crystallographically equivalent directions of the **X** axis in the high-temperature phase. These domains can be visually observed in polarized light. The magnetic measurements were performed with a vibrating-sample magnetometer (Oxford Instruments) and a SQUID magnetometer (Quantum Design). The magnetic resonance spectra were obtained using a set of microwave spectrometers with transmission type resonators covering the 9–150 GHz frequency range.

Figure 2 shows the temperature dependence of the magnetic susceptibility $\chi = M/H$ of $KFe(MoO_4)_2$ crystals for two orientations of the magnetic field: $\mathbf{H} \perp \mathbf{Z}$ and $\mathbf{H} \parallel \mathbf{Z}$. At a temperature of $T_N = 2.5$ K, the curves exhibit a feature corresponding to the transition to an ordered state. In the interval of temperatures 15 K $\ll$ $T < 300$ K, $\chi(T)$ follows the Curie–Weiss law with the characteristic constant $\Theta_{CW} = 21 \pm 2$ K. Approximation of the magnetic susceptibility by the Curie–Weiss law in the low-temperature range is shown by the dashed curve in Fig. 1. Using the Weiss constant, it is possible to estimate the average value of the exchange integral for the neighboring ions in the **XY** plane as $J = 3\Theta_{CW}/2zS(S + 1) \approx 0.6$ K ($S = 5/2$ and the number of nearest neighbors is $z = 6$). The Θ_{CW} is virtually the same for $KFe(MoO_4)_2$ and $RbFe(MoO_4)_2$ [3].

The inset in Fig. 2 shows the temperature dependences of M/H for various values of the static field **H** oriented in the crystal plane ($\mathbf{H} \perp \mathbf{Z}$). The absolute values of M/H for the fields 0.1 and 1 kOe are probably determined with an error of 10–50% because of a residual magnetic field of the superconducting solenoid. Open triangles indicate the aforementioned feature in the form of a magnetic susceptibility peak. The peak is observed in the region of weak fields ($0 < H < 20$ kOe) and exhibits smearing in higher fields. Above 30 kOe,
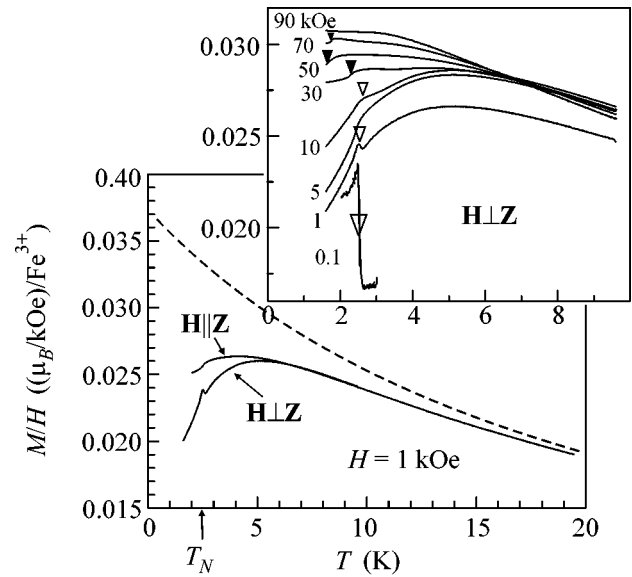

Fig. 2. The temperature dependence of the magnetic susceptibility $\chi = M/H$ of $KFe(MoO_4)_2$ crystals (for the sake of clarity, the curves for $\mathbf{H} = 0.1$ and 1 kOe in the inset are shifted along the ordinate axis).
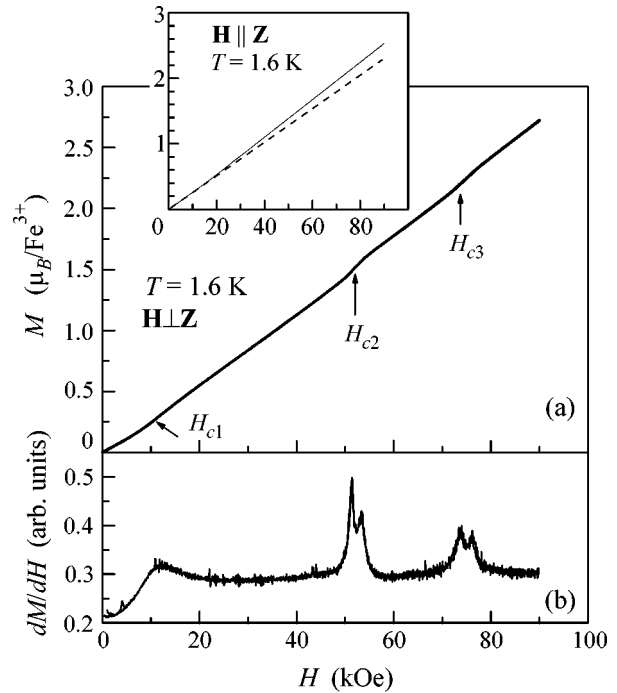

Fig. 3. (a) The magnetization curve $M(H)$ and (b) its derivative measured for a $KFe(MoO_4)_2$ crystal for $\mathbf{H} \perp \mathbf{Z}$. The inset shows the $M(H)$ curve observed for $\mathbf{H} \parallel \mathbf{Z}$ (the dashed line is tangent to the $M(H)$ curve in the region of small fields). All measurements were performed at $T = 1.6$ K.

the $M(T)$ curves exhibit variations in the form of steps, which are indicated by black triangles in the inset in Fig. 2. In addition, it should be noted that these curves exhibit a flattened maximum characteristic of low-dimensional antiferromagnets [6].
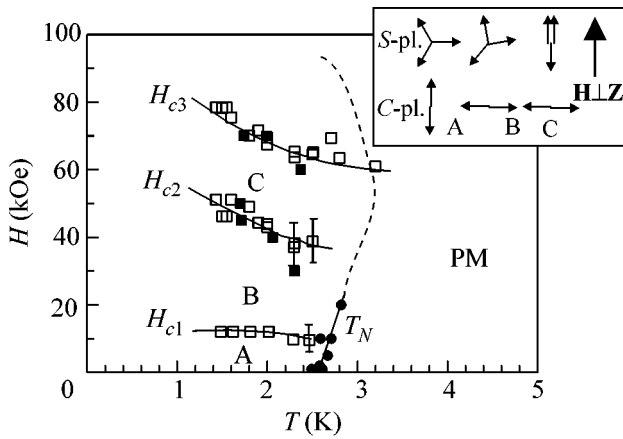
Fig. 4. The H versus T diagrams of the magnetic states observed for $\mathbf{H} \perp \mathbf{Z}$, showing the boundaries of the region of magnetic phases determined from (□) the $M(H)$ and (■) the $M(T)$ measurements. Black circles indicate the values of the Néel temperature. The inset shows the probable spin structures of the magnetic phases A, B, and C.

Figure 3a shows the $M(H)$ curves measured at $T = 1.6$ K for two orientations of the applied magnetic field. For $\mathbf{H} \perp \mathbf{Z}$, there are three features in these curves. Near $H = H_{c1} = 12.5$ kOe, there is a change in the slope of the $M(H)$ curve and the corresponding peak in the derivative dM/dH (Fig. 3b). The two other features are observed at $H_{c2} = 52$ kOe and $H_{c3} = 76$ kOe, where the derivative dM/dH exhibits sharp peaks. For $\mathbf{H} \parallel \mathbf{Z}$, the only special feature is an increase in the derivative in a field of 20–30 kOe. The slope of $M(H)$ in the region of lower fields was 0.9 of that in the region of higher fields ($H > 50$ kOe).

Figure 4 presents the H versus T diagram showing variation of the fields of magnetic phase transitions H_{c1}, H_{c2}, and H_{c3} determined for the features in the $M(H)$ and $M(T)$ curves and in the Néel temperature T_N determined by the position of the magnetic susceptibility peak.

The relation between susceptibilities, $\chi_\perp > \chi_\parallel$, observed in the fields above 20 kOe (where the difference reaches 5%) indicates that the "hard" magnetization direction is near the $\mathbf{Z}$ axis. In concluding so, we proceed from the fact that magnetic susceptibility exhibits a minimum along the hard axis in both collinear and triangular structures. The existence of a magnetic anisotropy with the hard axis oriented close to the $\mathbf{Z}$ axis is also confirmed by data on the paramagnetic resonance of Fe^{3+} ions at $T > T_N$ [7]. It should be noted that the absence of a high-order axis also implies the presence of another, so-called "medium" magnetization axis perpendicular to the hard axis.

The results of the experiments presented above show that the number of features of comparable magnitude on the $M(H)$ curve exceeds their number expected for both collinear and spiral structures on a distorted triangular lattice. Indeed, only one (spin-flop) feature is

expected for the collinear structure, and two such features (at the beginning and end of the magnetization plateau) are expected for the triangular and spiral structures [3, 8]. As was indicated above, the magnetic structure of $KFe(MoO_4)_2$ comprises two types of weakly bound alternating nonequivalent planes of magnetic ions. For this reason, we will consider a hypothetical model in which a collinear antiferromagnetic structure is formed in planes of the first type (C planes) and a spiral spin structure, in planes of the second type (S planes).

Within the framework of this model, the low-field feature at $H = H_{c1}$ can be considered as a reorientational transition in the C planes, which is related to rotation of the spin structure in the plane perpendicular to the hard axis. When the field is parallel to the easy axis, such a reorientation must have the character of spin flop, leading to a jump in the $M(H)$ curve. The feature observed in experiment exhibits a smoothened shape, which is explained by the presence of three domains with different orientations of their easy axes, on the one hand, and by a slight deviation of the easy axis from the $\mathbf{Y}$ axis in the $\mathbf{YZ}$ plane, on the other hand. This feature will be referred to below as a feature of the spin-flop type.

At the same time, the presence of phase transitions in the fields $\mathbf{H}_{c2}$ and $\mathbf{H}_{c3}$ on both sides of $(1/3)H_{\text{sat}}$ is characteristic of the 120° triangular structure ($J_1 = J_2$) [1, 3, 9] and the spiral structure on a distorted triangular lattice [8]. Note that the $(1/3)H_{\text{sat}}$ value apparently falls within the interval between $\mathbf{H}_{c2}$ and $\mathbf{H}_{c3}$. Indeed, judging from the H_{sat} value, this field has to be approximately on the same order of magnitude as in $RbFe(MoO_4)_2$ crystals, where saturation is reached at 186 kOe [9]. The inset in Fig. 4 shows the scheme of probable spin configurations for the field orientation $\mathbf{H} \perp \mathbf{Z}$. Our experiments did not reveal significant features during the transition from the paramagnetic to the ordered phase in the range of fields above 40 kOe. The probable position of such a transition or crossover between the above phases is depicted by the dashed line in Fig. 4.

The presence of hard-axis anisotropy suggests that a structure of the umbrella type is formed in the S planes at the $\mathbf{H} \parallel \mathbf{Z}$ orientation, while the C planes exhibit spin reorientation caused by a deviation of the hard axis from the $\mathbf{Z}$ axis in the $\mathbf{YZ}$ plane. The strong field dependence of the amplitude of the susceptibility peak in the region of weak fields probably corresponds to a small ferromagnetic moment, on the order of $10^{-4}\mu_B$ per Fe^{3+} ion.

Figure 5 shows the spectra of magnetic resonance measured at $T = 1.3$ K in the field $\mathbf{H}$ oriented parallel and perpendicular to the $\mathbf{Z}$ axis (i.e., significantly below T_N). Since the crystals studied at a temperature below 311 K exhibit the formation of domains of three types with different orientations of the X axis, the antiferromagnetic resonance (AFMR) line is usually split into three peaks with relative intensities strongly depending

on the realization of the domain structure in a particular sample. When the field is oriented parallel to the **Z** axis, all domains occur in approximately equivalent conditions and the observed absorption lines are not split. For this field orientation, there are four AFMR branches, one of which has a small dispersion (Fig. 5a). Figure 5b shows the spectra of magnetic resonance for five samples measured using the field oriented in the **XY** plane, with uncontrolled mutual orientation of the **Y** and **H** axes. In this case, the AFMR spectrum also displays four branches. The ν_1 branch (for which additional experiments with rotation of the sample showed the most pronounced dependence of the resonance frequency on the field orientation in the **XY** plane) is characterized by a broad distribution of resonance fields and frequencies in the ν versus H plane. In a zero field, the AFMR frequencies are $\nu_1^0 = 36 \pm 5$ GHz, $\nu_{3,4}^0 = 78 \pm 3$ GHz, and $\nu_2^0 = 123 \pm 3$ GHz.

In the triangular spin structure of RbFe(MoO$_4$)$_2$ crystals, the $\nu_{3,4}$ frequencies are close and exhibit similar field dependences with two branches of the magnetic resonance spectrum in the triangular spin structure [3]. In the case of KFe(MoO$_4$)$_2$ crystals, the behavior of $\nu_1(H)$ and $\nu_2(H)$ is characteristic of a collinear antiferromagnet with two anisotropy axes [10]. In Fig. 5, dotted curves show the AFMR spectrum calculated assuming that the $\nu_{1,2}(H)$ branches are determined by the homogeneous spin oscillations in the C planes [10], while $\nu_{3,4}(H)$ branches reflect oscillations in the S planes [3]. The interaction between the C and S planes was ignored.

Using the above zero-field AFMR frequencies, it is possible to estimate the values of magnetic anisotropy constants D in the microscopic theory (for the model Hamiltonian presented in [3]): $D_S \approx 0.25$ K and $D_C = 0.36$ K. The difference between ν_1^0 and ν_2^0 is explained by the biaxial character of anisotropy in the KFe(MoO$_4$)$_2$ crystals. Using these values, one can find that the magnetic anisotropy constant D_C'' for the medium magnetization axis in the C planes is approximately ten times as small as the D_C value. This anisotropy axis is parallel to the X axis. The AFMR spectrum of S planes was calculated disregarding the crystal anisotropy in the easy plane.

Thus, the obtained spectrum of magnetic resonance corresponds to a combination of the spectrum of a collinear biaxial antiferromagnet and the spectrum of a spiral or triangular antiferromagnet.

Summarizing the results presented above and generalizing the results of analysis, we conclude that the model of a magnetic structure comprising magnetic planes of two types—with collinear and spiral order—adequately describes the whole body of the static and resonance magnetic properties of KFe(MoO$_4$)$_2$ crystals. However, this statement is conjectural in nature, since the model does not take into account the interplanar interaction capable of leading to additional phase tran-
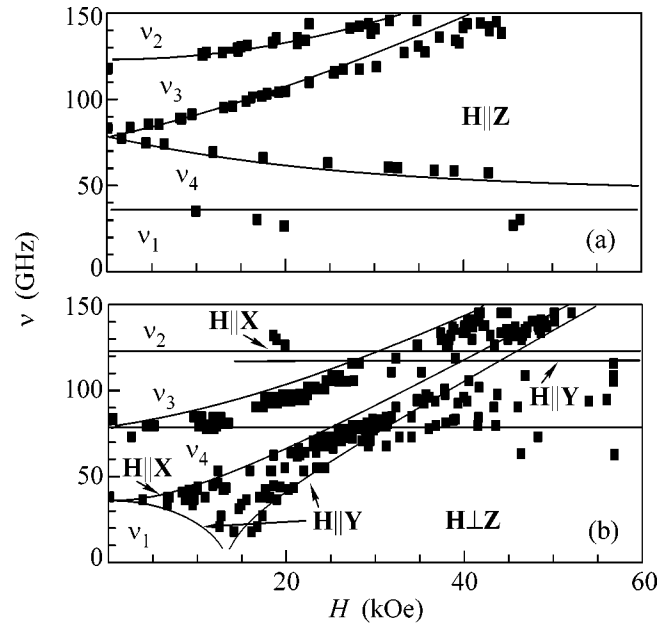

Fig. 5. Plots of the AFMR frequencies versus magnetic field for (a) **H** $\perp$ **Z** and (b) **H** $\parallel$ **Z** measured at $T = 1.6$ K.

sitions and lines in the magnetic resonance spectra (see [3]). The proposed exotic model can be verified in experiments on the determination of the magnetic structure using neutron scattering.

REFERENCES

1. S. E. Korshunov, J. Phys. C: Solid State Phys. **19**, 5927 (1986).
2. R. F. Klevtsova and P. V. Klevtsov, Kristallografiya **15**, 953 (1970) [Sov. Phys. Crystallogr. **15**, 829 (1970)].
3. L. E. Svistov, A. I. Smirnov, L. A. Prozorova, *et al.*, Phys. Rev. B **67**, 094434 (2003).
4. G. G. Kraĭnyuk, A. I. Otko, and A. E. Nosenko, Izv. Akad. Nauk SSSR, Ser. Fiz. **47**, 758 (1983).
5. W. Zhang, W. M. Saslow, and M. Gabay, Phys. Rev. B **44**, 5129 (1991).
6. L. J. de Jongh and A. R. Miedema, Adv. Phys. **50**, 947 (2001).
7. L. E. Svistov, A. I. Smirnov, L. A. Prozorova, *et al.*, Results of EPR Investigations (to be published soon).
8. T. Ono, H. Tanaka, H. Aruga Katori, *et al.*, Phys. Rev. B **67**, 104431 (2003).
9. T. Inami, Y. Ajito, and T. Goto, J. Phys. Soc. Jpn. **65**, 2374 (1996).
10. T. Nagamiya, K. Yosida, and R. Kubo, Adv. Phys. **4**, 1 (1955).

Translated by P. Pozdeev

Erratum: "The Proximity Effect in an Fe–Cr–V–Cr–Fe System" [JETP Lett. 80, 44 (2004)]

I. A. Garifullin, D. A. Tikhonov, N. N. Garif'yanov, M. Z. Fattakhov, L. R. Tagirov, K. Theis-Bröhl, K. Westerholt, and H. Zabel

PACS numbers: 74.45.+c; 7478.Fk; 75.70.Ak; 75.30.Fv

The name of one of the authors should read K. Theis-Bröhl.